Ultra-low power single crystal silicon SOI-CMOS micro-hotplate with novel temperature-modulation principle for chemical sensing

by

Takao Iwaki

School of Engineering

University of Warwick

A thesis submitted to the University of Warwick

for the degree of Doctor of Philosophy

December 2007

Contents

List of Figures

List of Tables

Acknowledgements

First of all, I would like to thank my academic supervisors Professor Julian Gardner and Dr James Covington for their constant guidance and support during the course of this project.

I wish to acknowledge all of the members of Sensors Research Laboratory, School of Engineering, University of Warwick, especially Mr Frank Courtney and Mr Ian Griffith for their assistance in practical work, and Ms Irina Leonte, Mr Jaleed Khawaja and Mr Fauzan Che Harun for valuable discussions.

I also would like to acknowledge Dr Florin Udrea at Centre for Advanced Photonics and Electronics, University of Cambridge, and the members of his research group, including Mr Prasanta Kumar Guha, Dr Syed Zeeshan Ali and Ms Cerdin Lee, for their support and discussions in developing the novel micro-hotplate devices.

I am grateful to Mr Oyuki Ogawa, the executive vice president of DENSO CORPORATION, and Dr Yoshiki Ueno, the head of DENSO Research Laboratories, for generously allowing me the opportunity of this study. I wish to acknowledge Mr Hiroaki Tanaka, Mr Kinya Atsumi, Dr Nobuaki Kawahara, Mr Yukihiro Takeuchi, Mr Kazuhiko Kano, Dr Hiroyuki Wado of DENSO Research Laboratories for technical discussions and constant encouragement. I also would like to acknowledge the members of DENSO SALES UK LTD., including Mr Kota Morioka, the former managing director, Mr Shiro Shimada, the managing director, and Mr Yasuhito Takasu for their constant support and encouragement. I am indebt to DENSO CORPORATION for financial support during the course of this study and for administrative support especially from the human resource department.

Lastly, I thank my wife, Akiko, our parents and my daughter, Anna, for their support, encouragement and patience.

Declaration

The work described in this thesis is entirely original and conducted by the author, except where otherwise indicated. The thesis has not been submitted for a degree at another university. Parts of this work have been published in the scientific literature listed below:

[1] T. Iwaki, J.A. Covington, F. Udrea, S.Z. Ali, P.K. Guha and J.W. Gardner, "Design and simulation of resistive SOI CMOS micro-heaters for high temperature gas sensors", Journal of Physics, Conference Series, 15, Sensors & their Applications XIII, pp. 27-32, 2005.

[2] T. Iwaki, J.A. Covington, J.W. Garder, F. Udrea, C.S. Blackman and I.P. Parkin, "SOI-CMOS based single crystal silicon micro-heaters for gas sensors", Proceedings of IEEE Sensors 2006, October 2006, pp. 460-463.

[3] T. Iwaki, J.A. Covington and J.W. Gardner, "Identification of vapours using a single carbon black/polymer composite sensor and a novel temperature modulation technique", Proceedings of IEEE Sensors 2007, October 2007, pp. 1229-1232.

[4] J.W. Gardner, F. Udrea, T. Iwaki, J.A. Covington, "Gas-sensing semiconductor", International patent application, WO 2007/026177.

During the course of his PhD study, the author contributed to a separate research project at the University of Cambridge, and parts of the work have been published as listed bellow:

[5] P.K. Guha, S.Z. Ali, F. Udrea, W.I. Milne, T. Iwaki, J.A. Covington and J.W. Gardner, "Novel design and characterisation of SOI CMOS micro-hotplates for gas sensors", Proceedings of Eurosensors XX, September 2006.

[6] S.Z. Ali, P.K. Guha, C.C.C. Lee, F. Udrea, W.I. Milne, T. Iwaki, J.A. Covington, J.W. Gardner, S. Maeng and J. Park, "High temperature SOI CMOS tungsten micro-heaters", Proceedings of IEEE Sensors 2006, October 2006, pp. 847-850.

[7] P.K. Guha, S.Z. Ali, C.C.C. Lee, F. Udrea, W.I. Milne, T. Iwaki, J.A. Covington and J.W. Gardner, "Novel design and characterisation of SOI CMOS micro-hotplates for high temperature gas sensors", Sensors and Actuators B, 127, 2007, pp. 260-266.

Summary

There is great need for the widespread use of indoor gas monitors as modern hermetically-sealed domestic buildings increasingly suffer from indoor air pollution. However, neither modern technologies of gas sensors nor analytical instruments are ideally suited to this purpose. The problems of gas sensors are poor selectivity and the fact that normally they can detect only one gas, and analytical instruments suffer from their large size and high price. Therefore, the aim of the project is "to develop a novel gas sensor with low cost, low power consumption, high reliability, which can detect multiple gases with excellent selectivity" for indoor gas monitoring.

In the first part of the project, an SOI-CMOS micro-hotplate with a single crystal silicon (SCS) resistive heater was proposed, fabricated and characterised. The design obviates issues of traditional heater materials *i.e.* platinum is not CMOS compatible and polysilicon is not thermally stable due to its polycrystalline structure. The SCS micro-hotplate was found to have an ultra low power consumption of 11.6 mW to operate at 500 °C, and an excellent reliability with less than 1 % drift after 500 hour operation at 500 °C.

In the second part, a novel temperature modulation technique for a carbon black/polymer composite sensor was theoretically derived based upon linear solvation and Fickian diffusion. The processing technique comprises only two steps; summing the off and on transient conductance signals from a temperature-stepped sensor, and subtracting the steady-state signal. The technique was demonstrated by applying to a carbon black/polyvinylpyrrolidone composite sensor employing the novel micro-hotplate. Identification of water, methanol and ethanol vapours was successfully demonstrated using the peak time of the resultant curve. Furthermore, quantification of those vapours was found to be possible using the height of the peaks, which was linearly proportional to the concentration.

In conclusion, a novel low-cost gas sensor has been realised that is capable of detecting more than one gas with a single sensing element and thermal modulation. This has the potential for commercial exploitation in the area of indoor air pollution monitoring.

Selected Abbreviations and Acronyms

TERM	DEFINITION
CMOS	Complementary Metal Oxide Semiconductor
DRIE	Deep Reactive Ion Etching
DWT	Discrete Wavelet Transform
FEM	Finite Element Method
FET	Field Effect Transistor
FFT	Fast Fourier Transform
FIA	Flow Injection Analysis
FTIR	Fourier Transform Infrared spectroscopy
FWHM	Full Width at Half Maximum
GC	Gas Chromatograph
IC	Integrated Circuit
LDA	Linear Discriminate Analysis
LP-CVD	Low Pressure Chemical Vapour Deposition
MFC	Mass Flow Controller
MFM	Mass Flow Meter
MLP	Multi-Layer Perceptron
MOS	Metal Oxide Semiconductor
NMOS	Negative Channel Metal Oxide Semiconductor
PC	Personal Computer
PCA	Principal Component Analysis
PCR	Principal Component Regression
PE-CVD	Plasma Enhanced Chemical Vapour Deposition
PLS	Partial Least Squares
PMOS	Positive Channel Metal Oxide Semiconductor
PVP	Polyvinylpyrrolidone
QCM	Quartz Crystal Microbalance
RT	Room Temperature
SAW	Surface Acoustic Wave
SBS	Sick Building Syndrome
SCS	Single Crystal Silicon
SOI	Silicon On Insulator
SRL	Sensors Research Laboratory
TCR	Temperature Coefficient of Resistance
TEM	Transmission Electron Microscopy
TMAH	Tetramethylammonium hydroxide
VOC	Volatile Organic Compound

CHAPTER 1

Introduction

1.1 The need for environmental gas monitors

Although outdoor air pollution has been a major issue for society for several hundred years, widespread monitoring and control has yet to be achieved. Most attention has been focused on pollutants from automobiles as the major source of the harmful or toxic gases (*e.g.* nitrogen oxides, carbon monoxide and volatile organic compounds (VOCs)) [1.1]. However, indoor air pollution probably has a much more significant effect on human health, as people spend as much as 90 % of their time indoors (according to U.S. Environmental Protection Agency [1.2]).

After the energy crisis in the 1970's, typical houses in the United States (US), which previously had ventilation paths allowing automatic refreshing of the air, were forced to be built with lower thermal losses to improve the energy efficiency [1.3]. Modern Japanese houses are also built to be hermetic sealed for more efficient control of the temperature and humidity with air conditioners, although the traditional ones enjoyed great natural ventilation with floors of *tatami* mat (an woven piece of straw) or *shoji* screens (slide doors made of paper) [1.4].

These airtight structures of modern houses have been identified at least partially responsible for the modern disease of "sick building syndrome (SBS)" [1.5]. There are a variety of symptoms of SBS, including eye, nose and throat irritations, headaches, nausea and dizziness [1.6]. Although the exact cause of the SBS is not known, it is suggested that one of the main causes is air pollution from various VOCs (volatile organic compounds, *e.g.* formaldehyde, benzene, perchloroethylene) emitted from

sources inside the buildings such as adhesives, upholstery, wood products and cleaning solutions [1.7]. Since indoor air pollution is much more localised than outdoors (components of the air can be different from building to building or even from room to room) and is caused by many types of gases, there is great need of small, low-cost gas monitors that can both identify and quantify such polluting gases or vapours.

There are already some commercial indoor air quality monitors. However, they are not widely used due to the following issues: they tend to be expensive, large, and can only detect a limited number of gases. For example, New Cosmos Electric Co., Ltd. (Japan) [1.8] produces a formaldehyde detector "Formtector XP-308B" using an electrochemical sensor (detailed later) with the price of *ca.* £ 700, dimensions W: 175 mm × H: 140 mm × D: 86 mm, and only one gas can be detected (formaldehyde). Another example is "Gasman CO_2" of Euro-Gas Management Services Ltd. (UK) [1.9]. This is a handheld gas monitor, and thus small. However, the price is *ca.* £ 500 and being limited to carbon dioxide detection makes the instrument impractical. Therefore, if the issues of size, cost and importantly multiple gas identification could be solved then a significant market would open up, leading to monitors being installed in most homes.

1.2 Gas sensors vs analytical instruments

The most gas monitors can be divided into two groups: gas sensors and analytical instruments. In this section, different gas sensors are briefly reviewed with an emphasis on metal oxide gas sensors and carbon black/polymer composite sensors due to their wide spread use. Then three types of analytical instruments, namely gas chromatographs, mass spectrometers and infrared spectrometers, are discussed. Finally their advantages and disadvantages are discussed from the point of view of indoor air quality monitoring.

1.2.1 Gas sensors

Metal oxide gas sensors

The most common type of gas sensor is probably the metal oxide resistive gas sensor. For example, nowadays most houses in Japan have gas leak detectors using this type of sensor. This has had a significant influence on reducing the number of gas explosion accidents since the 1970's [1.10]. Metal oxide sensors have also been commercialised

in a wide range of other applications, such as domestic or industrial carbon monoxide detection, air quality control (*e.g.* by detecting carbon dioxide) and portable alcohol detector (for measurements of the alcohol concentration in the human breath) [1.11].

The research on metal oxide sensors started on 1962, when Seiyama *et al.* first reported a gas sensing property of zinc oxide thin film [1.12]. In the same year, Taguchi patented a tin oxide gas sensor [1.13], and founded a company, Figaro Engineering Inc., which still is the world leading manufacturer of metal oxide gas sensors.

There are two major structures of metal oxide gas sensors: directly heated type and indirectly heated type [1.10]. Here the structure of the indirectly heated type sensor is explained. The main part is an alumina tube on which two gold electrodes and wires, made of gold palladium alloy, are connected. Tin oxide paste is painted on the alumina tube covering the electrodes, sintered at 725 °C. The wires are used to measure the resistance of the thick tin oxide film when operation. Inside of the alumina tube is a chromium alloy coil which act as a resistive heater.

The metal oxide sensors work at elevated temperatures (*e.g.* 350 °C) with the aid of the resistive heater [1.14]. Vacant sites exist through non-stoichiometry at the surface of the tin oxide and react with atmospheric oxygen thereby extracting an electron from the conduction band of the seminconducting tin oxide:

$$\frac{1}{2}mO_2 + \{\text{vacant site}\} + e^- \leftrightarrow \{O_m^-\} \tag{1.1}$$

where the index m varies according to the material and operating temperature. Therefore, a depletion layer is formed at the surface of the tin oxide grains. The depletion layer acts as a barrier to the mobility of the conduction electrons, and thus the resistance of the material increases. In the presence of reducing gas molecules, for example carbon monoxide, the adsorbed oxygen reacts with them and thus returning the electron to the material:

$$mCO + \{O_m^-\} \rightarrow CO_2 + e^- \tag{1.2}$$

As a result, the width of the depletion region decreases and so does the resistance. Therefore the concentration of the reducing gases is quantified by measuring the resistance. (Thus metal oxide sensors are often called chemoresistors).

An advantage of metal oxide gas sensors is their high sensitivity. For example, it has been reported that a thin film tin oxide chemoresistor prepared by reactive sputtering technique detected as low concentration as 5 ppb (parts per billion) of nitrogen dioxide gas with reproducibility [1.15]. However, the significant disadvantage of this type is their poor selectivity. Considering that the operation principle is simply the oxidisation/reduction reaction, it is natural that a single metal oxide gas sensor responds many types of gases and thus is difficult to identify the species. In fact, Yamazoe *et al.* tested tin oxide sensors with three different types of dopants (platinum, palladium and silver) in the presence of four types of gases (hydrogen, carbon monoxide, methane and propane) at temperatures between the room temperature to more than 400 °C, and all of the sensors responded to at least two gases within the temperature range tested [1.16].

Carbon black/polymer composite sensors

The carbon black/polymer composite sensor is another type of chemoresistor [1.17]. The composite material comprises of a non-conducting polymer in which carbon black nanospheres are dispersed. The carbon black nanospheres work as electrical pathways to make the composite material conductive.

In 1986, these types of composites were first reported to respond to vapours by Lundberg and Sundqvist who tested two materials (ET-Semicon® (AESA AB, Sweden) and carbon black/poly(tetrafluoroethylene) composite) to several types of vapours including butane, pentane and propane [1.18]. The vapour sensing characteristics of carbon black/polymer composites were investigated more intensively and patented by a research group at the California Institute of Technology lead by Lewis since mid 1990's [1.17, 1.19-1.22]. In 1996, Lonergan *et al.* reported experimental results on an array comprised of 17 different types of carbon black/polymer composite sensors with each of them having a different type of polymer (*e.g.* poly(4-vinylphenol), poly(styrene), poly(ethylene oxide)) [1.19]. They tested the array to 9 different vapours (*e.g.* toluene, methanol and 2-propanol), and found that all the sensors have different resistance response patterns. For example, the response of poly(4-vinylphenol) acetate to methanol

is *ca.* 49 times as much as that to benzene, whereas the response of poly(ethylene-*co*-vinyl acetate) to benzene is *ca.* 23 times as much as that to methanol. (The concentration they used were 23000 ppm (parts per million) for methanol and 17100 ppm for benzene). It was found that the diversity of the gas sensing characteristics of the array was suitable for discrimination of vapours. In fact, they separated out all of the 9 vapours using the first 5 principal components of the data from 17 sensors (the first 5 principal components contain more than 98% of the total variance). In 2000, Severin *et al.* reported on the results of 24 different types of carbon black/polymer composite sensors (*e.g.* poly(4-vinylphenol), poly(styrene), poly(ethylene oxide)) when tested to various single vapours (*e.g.* methanol, ethanol, benzene, toluene, chloroform) and binary mixtures with changing the concentrations. (Note: The concentration range was P/P_o = 0.005 – 0.03, where P and P_o is the partial pressure and the saturated vapour pressure) [1.20]. Their major findings are summarised as follows:

1. The signal of the sensor (*i.e.* relative differential resistance) is linearly proportional to the concentration when tested to any single gases.
2. The signal of the sensor to a binary mixture[1] is the sum of the signal for each vapour when exposed to a single vapour separately.

Considering that the principal components are the linear combination of the original sensor responses (*e.g.* [1.23]), the above findings can make the identification and quantification of single vapour much easier. In fact, they tested an array of 20 sensors to 8 types of alcohol vapours (methanol, ethanol, 1-propanol, 1-butanol, 1-pentanol, 1-hexanol, 1-heptanol and 1-octanol). The data in principal component space show that each vapour gave a unique and linear response pattern with the direction being specific to the type of vapour, and the height of the data proportional to the concentration.

There have also been efforts to understand the vapour sensing mechanism of carbon black/polymer composite sensors. First of all, Lundberg and Sundqvist qualitatively explained the resistance increase of the materials in the presence of vapours using the percolation theory [1.18]. According to them, the resistivity of the carbon black polymer is described as follows:

[1] This depends upon the precise choice of vapours tested and is not a general rule.

$$\rho = \frac{(z-2)\rho_c \rho_p}{A + B + \left[(A+B)^2 + 2(z-2)\rho_c \rho_p\right]^{1/2}} \tag{1.3 a}$$

where

$$A = \rho_c\left[-1 + (z/2)\left[1 - (v_c / f)\right]\right] \tag{1.3 b}$$

$$B = \rho_p\left[(z v_c / 2f) - 1\right] \tag{1.3c}$$

where ρ_c and ρ_p are the resistivities of the carbon black and polymer, v_c the volume fraction of the carbon black in the composite materials, z is the coordination number for the carbon black particles in the polymer pseudo-lattice, and f is the total packing fraction of the composite. The dissolved vapour molecules in the polymer cause the volume to increase, and thus the volume fraction of the carbon black in the composite materials v_c decreases. Therefore, using equation (1.3), the increase in the resistance is qualitatively explained, although it is difficult to find the realistic values for f and z for the composite.

In 2000, Severin and Lewis [1.21] reported experimental results and confirmed, at least partially, the above theory. Two types of carbon black/polymer composite materials (polymer: poly(caprolactone) and poly(ethylene oxide)) were tested to 8 types of vapours (*e.g.* hexane, isopropanol and benzene). Ellipsometry measurements of polymer films without carbon black were carried out on top of the normal resistance measurements in order to find the relationship between the swelling and the resistance increase. Their results are summarised as follows:

1. The relative differential resistance increase is linearly[2] proportional to the relative differential thickness increase, and the proportional constant is independent of the type of vapour.
2. The relative differential thickness increase is linearly proportional to the partial pressure (concentration) of the vapour.

[2] True for most vapours at low concentrations but depends on cross-linking and thermodynamics.

Therefore, the resistance change is directly related to the volume change (thickness change), and the volume change is directly related to the concentration of the vapour. Furthermore, the transient behaviour *i.e.* diffusion of vapour molecules into the polymer were explained quantitatively by Briglin *et al.* and Yates *et al.* using the assumption that the diffusion follows the Fick's law [1.22, 1.24].

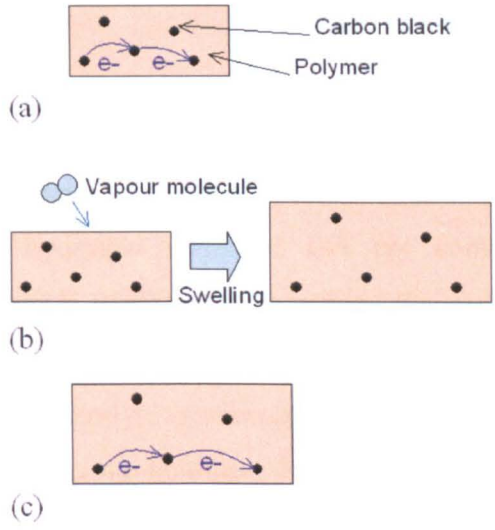

Figure 1.1. Gas sensing mechanism of carbon black/polymer composite chemoresistors. (a) Carbon black nanospheres dispersed in an insulating polymer form electrical pathways. (b) Gas molecules are absorbed in the polymer causing it to swell. (c) The increase in the distances between each nanospheres causes the resistances to increase.

A significant advantage of carbon black/polymer composite sensors is their low operating temperatures (*e.g.* room temperature) compared with metal oxide gas sensors. In addition, a significant diversity of the type of the sensor (*i.e.* polymer) and thus the sensitivity makes these materials suitable for electronic nose applications. However, the disadvantage is again poor selectivity. Since the operating principle of these gas sensors are simply the diffusion of the vapour molecules and the resultant swelling of the polymer, it is natural that they responds to a variety of vapours.

Others

As mentioned above, metal oxide sensors and carbon black/polymer composite sensors have the same common disadvantage; they respond to more than one gas, though they have only one output, and thus their selectivity is poor. Most other types of gas sensors suffer from the same issue including the following: (inherently) conducting polymer chemoresistors [1.25], MOSFET gas sensors [1.26], QCM (Quartz Crystal Microbalance) [1.27] or SAW (Surface Acoustic Wave) gas sensors [1.28] and pellistors [1.29].

An electrochemical sensor is one of the few examples of reasonably selective gas sensors [1.23]. These types of sensors are often used to detect toxic gases such as carbon monoxide and hydrogen sulphide, and are commercially available. An electrochemical sensor mainly comprises of a sensing electrode and a counter electrode dipped in the electrolyte. The sensing electrode is made of a catalytic metal (*e.g.* platinum), and the liquid electrolyte is often sulphuric acid or potassium hydroxide. At the three phase boundary (*i.e.* the boundary between the gas, electrolyte and catalyst) the gas molecule is either reduced or oxidised, depending on the target gas. (For example, carbon monoxide is oxidised, and nitrogen dioxide is reduced), and an electrical ionic current flows with its value proportional to the concentration of gases. The sensor is reasonably selective as the materials for sensing electrode (*i.e.* catalyst) and the electrolyte are chosen specially for the target gases.

1.2.2 Analytical instruments

Gas chromatographs

A gas chromatograph (GC) is one of the most commonly used instruments for environmental monitoring [1.30]. The main part of the gas chromatograph is the long "chromatography column". The inside of the column is either coated or packed by a stationary phase material (*e.g.* poly(ethylene glycol)). The sample gas is injected into the instrument, and is forced to travel inside the column with the aid of a carrier gas. Since the stationary phase material absorbs the gas molecules with differing affinities depending on their types, different types of molecules arrives the exit at different time (retention time). Therefore, by detecting the gases at the exit, identification and quantification of each gas in a mixture is possible. Their separation ability can be

enhanced by using a long chromatography column and by optimising the type of the stationary phase material.

Mass spectrometers

A mass spectrometer is another common type of analytical instrument which can be used for gas monitoring [1.23]. The gas samples are first introduced into a vacuum chamber, and then ionised by, for example, an electron ionisation technique (sample molecules are ionised by the electrons, which are thermally emitted from a filament and then accelerated by an electric field). The ions are accelerated by an electric field and introduced into the mass analyser. In the mass analyser the ions are separated according to their mass to charge ratio with the aid of a magnetic field. Therefore, it is possible to identify and quantify multiple gases simultaneously. The advantage is the excellent sensitivity; in fact this technique is often used to measure the partial pressure of gas species inside the high vacuum chamber for laboratory experiments. The disadvantage is obviously the complexity of the instruments due to the need of vacuum and high voltages.

Optical spectrometers

An optical spectrometer is an instrument that can detect the absorption of light at various wavelengths (usually between infrared and ultraviolet) [1.31]. Gas molecules have their specific modes of mechanical vibration and rotation. Hence, when light travels through a medium of gases, the light with the wavelength corresponding to the specific modes of gases is absorbed, making it possible to identify the types using the wavelength value. In addition, according to the Beer's law, the absorbance (the logarithm of the reciprocal of the transmittance) is proportional to the concentration of the gas and the path length (the distance the light travel through the gases). Therefore, quantification of gases is also possible. The advantage of an optical spectrometer, when compared with a gas chromatograph or a mass spectrometer, is its relative simplicity; it does not need to force the gases to flow at a constant rate nor require vacuum pump. The disadvantage is relatively low sensitivity.

1.2.3 Comparison between sensors and analytical instruments

The above brief review shows that most gas sensors, apart from electrochemical sensors, have the disadvantage of poor selectivity. In addition, gas sensors normally return only one output voltage, and thus will not be able to identify and quantify gas mixtures even if the poor sensitivity issue is resolved. Therefore, modern gas sensor technologies, although small and cheap are not ideally suited for indoor environmental monitoring.

On the other hand, all of the above analytical instruments can detect multiple gases simultaneously with excellent selectivity. It may be useful to point out what the above analytical instruments have in common, which gives their strong separation ability. All of the above analytical instruments measure the value of a physical quantity to identify the type of gases, and the intensities of the signal corresponding to the value of the physical quantity. For example, a gas chromatograph measures the retention time (*i.e.* the strength of the interaction of the gases and stationary phase material) for identification and the amplitude of the signal at the specific retention time. A mass spectrometer and an optical spectrometer detect the mass to charge ratio and the wavelength for identification, both of which are specific to a type of gas, and amplitudes of the signal for quantification. However, their main issues are their size and the price. Although portable analytical instruments are commercially available, at present, their sizes are not small enough. For example, a portable gas chromatograph (3000 Micro GC) manufactured by Agilent Technologies, Inc. (US) [1.32], and a portable FTIR (Fourier Transform Infrared spectroscopy) (Gasmet DX-series) instruments by Gasmet Technologies Oy (Finland) [1.33] have the sizes of a computer tower case. Therefore, it can be concluded that there is no commercially available gas monitor which is suitable for ubiquitous indoor environmental monitoring applications.

Considerable efforts toward commercial ubiquitous gas monitors are, of course, still being made. It may be possible to split those efforts into two types: (1) miniaturising the analytical instruments, and (2) enhancing the selectivity and increasing the number of gases being detected using gas sensors.

First of all, many reports have already been published concerning miniaturisation of gas analytical instruments. Sandia National laboratory (US) reported on a handheld gas chromatograph unit "μChemlab" [1.34, 1.35]. The unit comprises three miniaturised components fabricated by micro-technology, namely a micro-hotplate based pre-concentrator, a column micromachined by deep reactive ion etching

(DRIE) technique and an array of surface acoustic wave sensors fabricated on a piezoelectric substrate. Identification and quantification of various vapours were successfully demonstrated and thus this approach is promising. The issue is that the limited degree of miniaturisation, as it is needed to assemble a number of parts including a pump and valves.

Taylor *et al.* reported on a miniature mass spectrometer in 2000 [1.36]. They fabricated quadrupole rods, which is the main part of a mass spectrometer, and demonstrated a separation between O^+, OH^+, H_2O^+ and Ar^{2+}. However, to replace fully a conventional mass spectrometer, it is necessary to miniaturise the vacuum chamber (including a pump and electron gun), which is very challenging.

There are some small infrared interferometers, which are already commercially available. For example, Robert Bosch GmbH (Germany) has produced "Climate Control Sensor CCS" ($60 \times 50 \times 20$ mm^3), which is used to measure the concentration of carbon dioxide inside the car cabin [1.37]. Although currently it cannot detect more than one gas (it detects only CO_2), it may lead to a miniaturised infrared spectrometer in the near future.

The other approach is to improve gas sensors to make multiple gas detection possible. In order to quantify n types of gases, it is needed to solve the following n equations simultaneously:

$$\begin{cases} f_1(c_1, c_2, \cdots, c_n) = b_1 \\ f_2(c_1, c_2, \cdots, c_n) = b_2 \\ \vdots \\ f_n(c_1, c_2, \cdots, c_n) = b_n \end{cases} \tag{1.4}$$

where c_i is the concentration of each gas species and b_j is the feature acquired by the gas sensor(s). Obviously the number of features required is n, though normally a gas sensor can return only one feature. There has been significant research on increasing the number of uncorrelated features obtained by gas sensors, and they can be split into two areas: using a sensor array and temperature modulation techniques.

Enhancing sensitivity using an array has been investigated with various types of sensors such as metal oxide gas sensors [1.38], MOSFET sensors [1.39], conducting polymer sensors [1.40], carbon black/polymer composite sensors [1.20], surface

acoustic wave sensors [1.41], electrochemical sensors [1.42]. Although most of the research is focusing on qualitative analysis from the data taken by using arrays (*e.g.* discrimination between different odours), there have been several reports on quantitative analysis. Sundgren *et al.* have reported on quantification of each gas from a multi-component gas mixture using a MOSFET gas sensor array in 1990 [1.39]. The array composed of six sensors: three palladium gate MOSFET sensors and identical platinum gate ones. The three sensors in each type are identical but are operated at different temperatures: 100 °C, 150 °C and 200 °C. The array was tested to mixtures consisting of hydrogen, ammonia, ethylene, and ethanol with different concentrations, and the results were processed using partial least squares (PLS) technique. It has been demonstrated that the array has an ability to quantify the concentration of hydrogen, though more efforts are needed to quantify the other three gas species. In 2000, Severin *et al.* [1.20] successfully demonstrated, in a principal component space, the following:

1. Identification and quantification of 8 types of single alcohol vapours with an array comprising of 20 carbon black/polymer composite sensors.
2. Identification and quantification of 8 types of single alkane vapours with an array comprising of 20 carbon black/polymer composite sensors.
3. Identification and quantification of each vapour in a binary mixture of benzene and nitrobenzene vapours with an array comprising of 12 carbon black/polymer composite sensors.

Thus, it may be concluded that using an array is a promising approach toward simultaneous multi gas monitoring. One of the main issues of this approach, when used for ubiquitous environmental gas monitors, is the cost; the developing cost for 10 –20 different types of chemical sensors with guaranteed reliability is enormous.

Therefore, in this thesis focus will be towards developing a novel temperature modulation technique. The device, which will be developed in the project, should not only be able to detect (*i.e.* identify and quantify) many gases selectively and simultaneously, but also have price and size, both of which are small enough for indoor air quality monitoring applications.

1.3 Temperature modulation technique using micro-hotplates

Temperature modulation is a promising technique to enhance a selectivity of gas sensors [1.43]. It is possible to increase the number of features obtained from a single gas sensor by using a temperature modulation technique. This is because a gas sensor normally responds to multiple gases and because the shape of the response vs temperature curve is a function of the type of the gas [1.16]. Taguchi type metal oxide gas sensors were generally used in the early research on temperature modulation. For example, in 1989, Sears *et al.* [1.44, 1.45], who were one of the first research groups to use temperature modulation techniques, used TGS#821 manufactured by Figaro Engineering Inc. [1.11]. A sinusoidal voltage with an offset was applied to the heater, and the response of the sensor was measured over time in the presence of various single gases (ethanol, propane, methane, carbon monoxide, acetone and hydrogen) [1.44]. It was found that the shape of the curves depends upon the type of gas, which could lead to the enhanced selectivity. (Note: The curves shown in the paper also depend on the concentration, and thus performing identification and quantification will not be straightforward).

Nowadays most of research on temperature modulation techniques is carried out using a resistive gas sensor with a micro-hotplate, which is a thermally isolated thin membrane (typical thickness: 1-2 μm) structure with a resistive heater embedded in it, fabricated by silicon microtechnology (described in detail later). This is because micro-hotplate based gas sensors are more advantageous than classical ones as they have lower thermal response times and consume less power. Hence, this section focuses on the research performed with micro-hotplates.

The procedure for temperature modulation of a gas sensor is generally as follows:

1. The sensor is operated with modulated heater voltage (thus with modulated temperature) and the sensor response is measured over time.
2. The features are extracted from the sensor response. Signal processing technique such as FFT (First Fourier transform) or DWT (Discrete Wavelet Transform) is often used for this purpose.
3. Identification or quantification is performed. Suitable data processing techniques are used depending on the purpose. PCA (Principal component analysis) for

qualitative analysis and PCR (Principal component regression), PLS (Partial least squares) for quantitative analysis.

A feature extracted from the signals of temperature modulated chemoresistors can either be a static feature (*e.g.* a saturated response at a certain temperature) or a transient (or non-static) feature (*e.g.* a transient response caused by a temperature change). A static feature is extracted more efficiently by applying a sinusoidal wave voltage to the heater, and a square wave voltage is often used in order to extract transient features. Research on temperature modulated micro-hotplates started with using sinusoidal wave voltage in the late 1990's [1.46, 1.47], though more recently some authors have started reporting on the use of a square wave voltage [1.48, 1.49].

When using a sinusoidal wave for temperature modulation, normally the frequency is chosen to be slow (*e.g.* 50 mHz) so that the sensor operates close to the steady state. In 1997, Heilig *et al.*, applied a sinusoidal voltage with the frequency of 50 mHz to a platinum resistive heater micro-hotplate on which a palladium doped tin oxide thick film was deposited This was tested to carbon monoxide, nitrogen dioxide and their mixtures at various concentrations [1.46]. First Fourier transform (FFT) was applied to the raw data, and the first six coefficients (corresponding to 0 Hz, fundamental frequency and its first four harmonics) were extracted as features. The features were used for quantitative prediction of the concentration of carbon monoxide and nitrogen dioxide using an artificial neural network (with 5 input nodes/5 hidden neurons/2 output neurons). The prediction was successful with few outliers. Then, in 2001, Llobet *et al.* applied a discrete wavelet transform (DWT) technique to the data from a temperature modulated (50 mHz) micro-hotplate based metal oxide (palladium doped tin oxide) gas sensor [1.47]. The tested gases were carbon monoxide, nitrogen dioxide and their mixtures, which were successfully identified and quantified using multi-layer perceptron (MLP) neural network method. They also applied FFT to the same data and found that DWT outperformed FFT as a feature extraction technique.

Square wave temperature modulation is more suitable to extract transient features. In 2005, Parret *et al.* tested an undoped tin oxide chemoresistor based on micro-hotplate technology [1.48]. Square wave temperature modulation was used with the sensor tested with carbon monoxide, nitrogen dioxide, propane and their mixtures with various concentrations. It was found that the shape of the transient curve

associated with a step temperature increase or decrease was strongly affected by the presence of gases. Then, in 2006, Menini, *et al.* from the same research group, applied a square wave voltage to a platinum doped tin oxide chemoresistor in the presence of carbon monoxide, propane, nitrogen dioxide and their mixtures with various concentrations [1.49]. Features (*e.g.* the time and amplitude of the peak) were extracted from the temperature transient curves when the temperature steps up from 110 °C to 550 °C. The concentration of carbon monoxide was quantified successfully using the linear discriminant analysis (LDA) technique.

Although most of the reports discussed above are successful in identification and quantification of gases they tested, there is a major issue that requires resolving before commercialisation. Pre-calibration of the sensors is needed with not only with single gases but also their mixtures. This is because the response of metal oxide gas sensors is not linear in gas concentration and thus the simple superposition of the responses for different gases is not possible [1.10]. Therefore, if quantification of 5 different types of gases is required, which may happen for indoor air quality monitor, pre-calibration has to be carried out for all the possible concentration combination of those 5 gases, which makes the commercialisation difficult.

One promising way to solve the above issue is to apply a temperature modulation technique to a carbon black/polymer composite sensor. As described earlier, it has already been shown that the response of carbon black/polymer composite sensors is linearly proportional to the concentration and superposition is possible [1.20]. However, there has only been preliminary research on temperature modulation of carbon black/polymer composite sensors. In 2007, Kim *et al.* proposed to introduce an additional thermodynamic feature when processing the results of the array of carbon black/polymer composite chemoresistors [1.50]. Four different types of carbon black/polymer composite sensors (poly(ethylene oxide), poly(ethylene-co-vinyl acetate), poly(caprolactone) and poly(α-methylstyrene)) were tested to three different vapours (methanol, acetone and benzene) of various concentrations at five different temperatures (21 °C, 25 °C, 29 °C, 34 °C and 38 °C). The logarithm of the response of the chemoresistor (*i.e.* $\ln(\Delta R/R)$, where R and ΔR are the resistance of the chemoresistor in air and the change in the resistance in the presence of the vapour) was plotted against the inverse of the absolute temperature (*i.e.* $1/T$, where T is the absolute temperature). The value of the slope was found to depend on a type of vapour as shown in figure 1.2

and was proposed to be used as a new thermodynamic feature. It was demonstrated that the classification capability between the vapour classes was enhanced by adding the new feature. However, to the best of our knowledge, quantification of gases/vapours using temperature modulated carbon black polymer/composite films has not been reported.

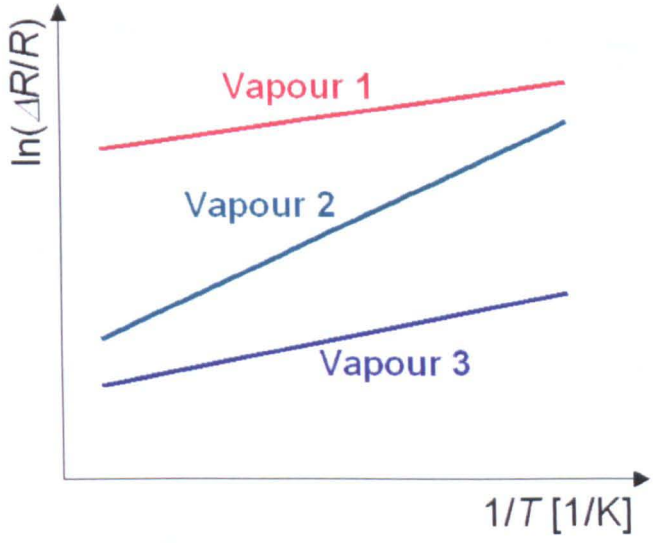

Figure 1.2. Conceptual illustration of the additional thermodynamic feature proposed in [1.50].

1.4 Micro-hotplate technology

1.4.1 Overview of micro-hotplate technology

As mentioned earlier, micro-hotplate based chemoresistos have two significant advantages compared with classical gas sensors (*e.g.* Taguchi type metal oxide gas sensors): faster thermal response and lower power consumption. Therefore, it is desirable a micro-hotplate technology is employed in the target device *i.e.* a temperature modulated gas sensor, which is capable to identify and quantify multiple gases, for indoor air quality application.

Micro-hotplates for gas sensors were proposed in the late 1980's and have been investigated by researchers ever since. In 1988, Demarne *et al.* first demonstrated a tin oxide micro gas sensor employing resistive heater made of gold [1.51]. Later Stoev *et al.* (1990) reported a tin oxide gas sensor using a polysilicon resistive heater [1.52]. Predominantly micro-hotplates are divided into two groups: those with a solid membrane and those with a suspended bridge [1.14, 1.53]. Examples of these designs

are illustrated in figures 1.3 and 1.4. Here, the structure and the operation principle of the solid membrane type are mainly explained and the difference from suspended bridge type is commented wherever required.

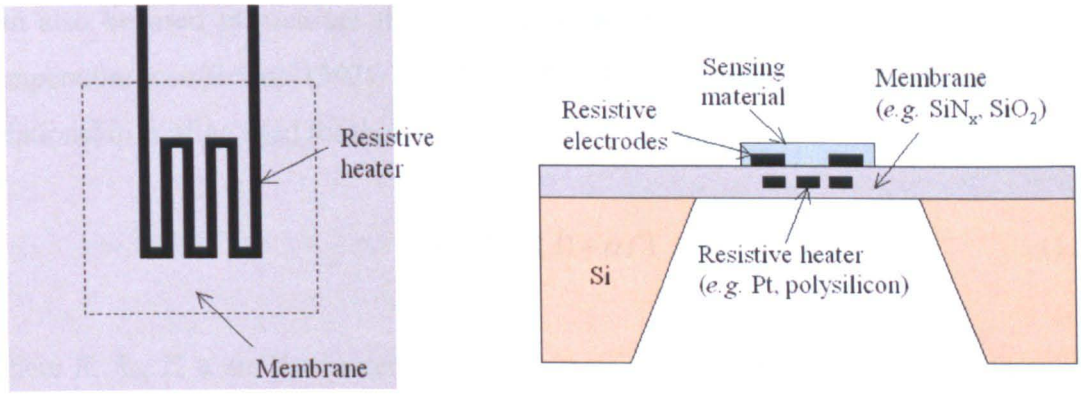

Figure 1.3. Schematic of solid membrane type gas sensor: (a) top view, (b) cross sectional view.

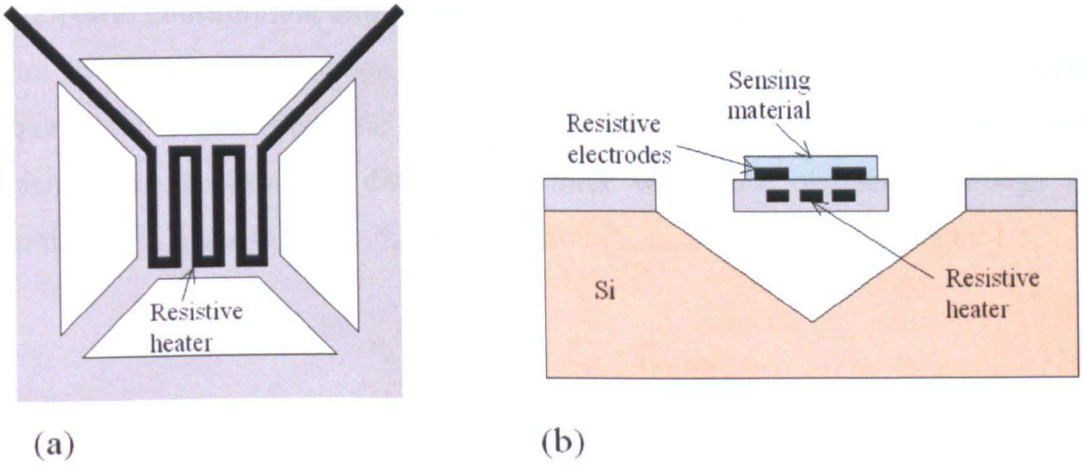

Figure 1.4. Schematic of suspended bridge type gas sensor: (a) top view, (b) cross sectional view.

The thin membrane structure comprises of multiple layers of thin films: silicon dioxide and silicon nitride with the total thickness of typically 1 –2 μm. The substrate silicon underneath is etched away by anisotropic wet etching using KOH or TMAH. A resistive heater (typically made of platinum or polysilicon) with meandering shape is sandwiched between those films. This thin membrane structure helps to thermally isolate the heater from the silicon substrate to reduce heat dissipation. The bridge type

shown in figure 1.4 has a similar structure, but the anisotropic silicon wet etching is performed from the front side rather than the backside.

The resistive heater is operated simply by Joule heat: *i.e.* either a constant current or voltage is applied (when temperature is not modulated). This resistive heater can also be used to measure the temperature as its resistance tends to have a large temperature coefficient (3927 ppm/°C for bulk platinum [3] [1.54]). The following relationship is often used for this purpose:

$$R(T) = R_0(1 + \alpha T) \tag{1.5}$$

where R, R_0, T, α are the heater resistance, heater resistance at 0 °C, temperature, and the temperature coefficient of the resistance (TCR), respectively. Alternatively, a separated temperature sensor (*e.g.* resistor or diode), which is also embedded in the membrane, can be used [1.53].

1.4.2 Power consumption and response time of micro-hotplates

Ultra low power consumption, which makes battery operation possible, could be required for a gas sensor for indoor air quality monitor application. The power generated by the heater is dissipated in three ways: heat dissipation through the membrane $P_{membrane}$, to the air P_{air} and radiation $P_{radiation}$ as illustrated in figure 1.5.

$$P_H = P_{membrane} + P_{air} + P_{radiation} \tag{1.6}$$

Previous work has shown that each power loss has the following relationship with geometry:

$$P_{membrane} \propto 1/ln(r_m/r_h) \tag{1.7 a}$$

$$P_{air} \propto A \tag{1.7 b}$$

$$P_{radiation} \propto A \tag{1.7 c}$$

[3] Value is different for thin films.

where r_m, r_h denotes the membrane and heater radius, and A the heated area [1.53]. For equation (1.7 a), a circular shaped membrane and heater is assumed. In 1997, Pike *et al.* reported that the heat loss to the air is the greatest for large heaters with a heated area of 0.5 mm^2 [1.55]. Their reported values of heat loss through the membrane, to the air and radiation at the operating temperature of 350 °C are *ca. 40, 80, 10* mW, respectively. However, researchers aiming at lower power consumption choose much lower heating areas (0.03 mm^2 – 0.23 mm^2) [1.56-1.58]. Since the heat loss to the air is proportional to the heated area and the heat loss through the membrane does not depend on it, the heat loss through the membrane is expected to be the most significant one for these low power consumption micro-hotplates with smaller heated area. In fact, Lee *et al.* fabricated a pellistor based on micro-hotplate technology with different membrane to heater ratios (2.7 – 5.0) [1.56]. It was found that the normalised response of the pellistor to methane, which should be inversely proportional to the heat dissipation, monotonously increases as the membrane to heater ratio increases, indicating that the heat dissipation through the membrane is a significant heat dissipation mechanism of their micro-hotplates.

Therefore, it may be concluded that the optimum micro-hotplate design, in terms of power consumption, should have (1) small heated area and (2) high membrane to heater ratio. The maximum membrane to heater ratio reported so far is, to our knowledge, 5.0 [1.56]. Considering equation (1.7 a), it is possible to decrease the power consumption by, for example, 30 % by increasing the membrane to heater ratio to 10.0.

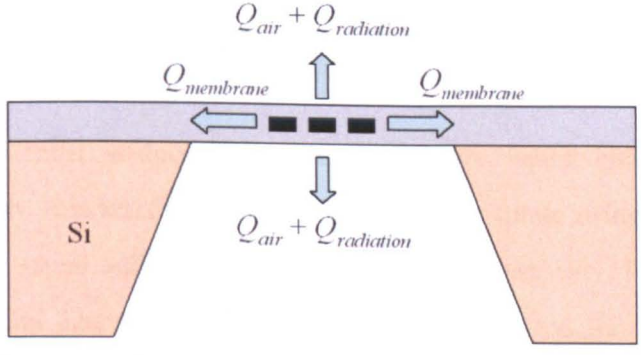

Figure 1.5. Three heat dissipation mechanisms from a micro-hotplate.

A short thermal time constant is one of the requirements for micro-hotplates especially when used for temperature modulation with a square wave voltage. Thermal time constant τ is usually defined by the following relationship, which is the temperature response to a step function:

$$T(t) - T_{amb} \propto 1 - exp(-t/\tau) \quad (1.8\text{ a})$$

$$\tau = R_{therm} C_{therm} \quad (1.8\text{ b})$$

where T is the temperature, R_{therm} the thermal resistance and C_{therm} the heat capacity. Thus, to shorten the thermal response, both thermal resistance and heat capacity must be decreased. Heat capacity is automatically decreased when ultra-low power micro-hotplates are designed, though thermal resistance may increase in order to use the power efficiently. However, considering that the typical time constant of micro-hotplates is 10 ms (For example, in 1997, Sberveglieri *et al.* reported that the thermal time constants of their micro-hotplates are 20 ms at RT and 10 ms at 500 °C [1.59]), which is much smaller than that of traditional chemoresistors (*e.g.* the thermal time constants of typical Taguchi type gas sensors is 10 s [1.10]), there is little need to take into account the thermal time constants when designing micro-hotplates for this project.

1.4.3 Long term stability of micro-hotplates

Long term stability is the most important feature when it comes to commercialising micro-hotplate based gas sensors, though there has been very little research carried out on this issue. In general, long term stability mainly depends on the material used for the resistive heater.

One of the most widely investigated resistive heater materials for micro-hotplates is platinum. It is sensible to develop a micro-hotplate using this material as it is an inactive noble metal and thus has excellent thermal stability. For example, Qu *et al.* (2000) [1.60] and Lee *et al.* (2003) [1.61] demonstrated the operation of their platinum based micro-hotplates at 800 °C and 750 °C. Silicon carbide (SiC) is another high temperature material, and in 2001, Sozbancher *et al.* fabricated and demonstrated the operation of SiC based micro-hotplates at more than 800 °C [1.62]. However, neither platinum nor silicon carbide is a CMOS compatible material and thus such

designs cannot be fully integrated with drive/detection circuitry or take advantage of the low production costs associated with CMOS.

CMOS compatible polysilicon heaters have also been widely investigated. However, their long term stability has been reported to be poor due to the highly reactive grain boundaries [1.63, 1.64]. In 2000, Rydberg *et al.* showed that their polysilicon heater drifts at 0.8 - 3 % after operated at a low temperature of 150 °C for 500 hours [1.63]. Gràcia *et al.* (2001) showed that their polysilicon heater drifts at 2 %, 5 %, 11 % after being operated at 350 °C, 420 °C, 550 °C for 1000 hours [1.64]. Furthermore, several studies have been made on highly boron doped single crystal silicon based micro-hotplates formed by anisotropic selective wet silicon etching (*e.g.* [1.65]). These are CMOS compatible and the heater material itself is believed to be thermally stable without the grain boundary issue, which causes the resistance drift in polysilicon. However, the wet etching process makes it impossible to passivate the bottom of the heaters within the CMOS process. Therefore, the heaters are easily contaminated and the commercial exploitation is difficult. Micro-hotplates using FETs, based on SOI-CMOS technology, was proposed in 2001 [1.66]. The structure employs FET as a heater, and thus essentially single crystal silicon is the heater material. Furthermore, the heater is passivated properly from underneath by the buried oxide layer of the SOI wafer. However its operating temperature is limited to less than 400 °C, because of the bipolar turn-on of the MOSFET and the use of aluminium interconnects.

Therefore, it is concluded that there has been no reported micro-hotplates that are both CMOS compatible and reliable. Hence, there is a significant need to develop such a micro-hotplate in order to achieve our target device.

1.5 Aim of the project

In summary, there is great need for the widespread use of indoor gas monitors as modern hermetically-sealed domestic buildings increasingly suffer from indoor air pollution. However, neither modern technologies of gas sensors nor analytical instruments are ideally suited to this purpose. The problems of gas sensors are poor selectivity and the fact that normally they can detect only one gas, and analytical instruments suffer from their large size and high price.

Therefore, the project is dedicated to the development of technology for indoor gas monitors. More specifically, the aim of the project is "to develop a novel gas sensor

with low cost, low power consumption, high reliability, which can detect multiple gases with excellent selectivity". To achieve this aim, the project has been split into two parts: development of a novel ultra low power and reliable CMOS compatible micro-hotplate, and development of a novel temperature modulated carbon black/polymer composite sensor capable of identifying and quantifying several different gases simultaneously using the developed micro-hotplate.

1.6 Outline of the thesis

In chapter 1, the issue of modern indoor air quality is discussed, and both gas sensor and analytical instrument technologies are reviewed. Finally, the aim of the project is described.

In chapter 2, a novel SOI-CMOS micro-hotplate design is proposed and designed aiming at low cost, low power consumption and good reliability. Electro-thermal FEM (Finite Element Method) simulation of the novel design is also performed to confirm the design concept.

Chapter 3 covers fabrication process and characterisation of the proposed micro-hotplates. The characterisation is mainly focusing on confirming the designed ultra low power consumption, and finding the long term stability of the novel structure.

In chapter 4, a novel temperature modulation technique, which can both identify and quantify multiple gases using a singe gas sensor, is proposed. The technique is derived by pure mathematical discussion assuming the linear solvation of the vapour molecules into a polymer film and Fickian (linear) diffusion.

In chapter 5, the novel temperature modulation technique, proposed in chapter 4, is tested experimentally. Identification and quantification of different gases are carried out.

In chapter 6, an improved technique is proposed and demonstrated, settling the issues of the technique described in chapters 4 and 5.

Chapter 7 concludes this research reviewing the principal results and discussing how these have fulfilled the aim of the project. Lastly, possible further work is proposed.

References

[1.1] UK air quality archive, http://www.airquality.co.uk/archive/index.php, accessed on 15th November 2007.

[1.2] U.S. Environmental Protection Agency, Office of Air and Radiation. "Report to congress on indoor air quality, Volume II: Assessment and control of indoor air pollution", 1989, pp. I, 4-14.

[1.3] Federal occupational health, http://foh.dhhs.gov/default.asp, accessed on 15th November 2007.

[1.4] Kansai window, http://www.kansai.gr.jp/, accessed on 15th November 2007.

[1.5] The American Lung Association (ALA), The Environmental Protection Agency (EPA), The Consumer Product Safety Commission (CPSC), and The American Medical Association (AMA)," Indoor air pollution: An introduction for health professionals", U.S. Government Printing Office Publication No. 1994-523-217/81322, 1994.

[1.6] Health and Safety Executive/Local Authority Enforcement Liaison Committee (HELA), http://www.hse.gov.uk/lau/hela/index.htm, accessed on 15th November 2007.

[1.7] United States Environmental Protection Agency (EPA), "Indoor air facts No. 4 (revised), sick building syndrome", 1991.

[1.8] New Cosmos Electric Co., Ltd., http://www.new-cosmos.co.jp/en/, accessed on 8th December 2007.

[1.9] Euro-Gas Management Services Ltd., http://www.euro-gasman.com/, accessed on 8th December 2007.

[1.10] K. Ihokura and J. Watson, "The stannic oxide gas sensor, principles and applications", CRC Press, Boca Raton, 1994.

[1.11] Figaro Engineering Inc., http://www.figaro.co.jp/, accessed on 15th November 2007.

[1.12] T. Seiyama, A. Kato, K. Fukiishi and M. Nagatini, "A new detector for gaseous components using semiconductive thin films", Analytical chemistry, Vol. 34, 1962, pp. 1502-1503.

[1.13] N. Taguchi, Japanese patent. S45-38200, applied in 1962.

[1.14] J.W. Gardner, V.K. Varadan and O.O. Awadelkarim, "Microsensors, MEMS, and Smart Devices", Chichester: Wiley, 2001.

[1.15] J. Santos, P. Serrini, B. O'Beirn and L. Manes, "A thin film SnO_2 gas sensor selective to ultra-low NO_2 concentrations in air", Sensors and Actuators B, 43, 1997, pp. 154-160.

[1.16] N. Yamazoe, Y. Kurokawa and T. Seiyama, "Effects of additives on semiconductor gas sensors", Sensors and Actuators, 4, 1983, pp. 283-289.

[1.17] N.S. Lewis, "Comparisons between mammalian and artificial olfaction based on arrays of carbon black – polymer composite vapor detectors", Accounts of Chemical Research, 37, 2004, pp. 663-672.

[1.18] B. Lundberg and B. Sundqvist, "Resistivity of a composite conducting polymer as a function of temperature, pressure, and environment: Applications as a pressure and gas concentration transducer", Journal of Applied Physics, Vol.60, No.3, 1986, pp. 1074-1079.

[1.19] M.J. Lonergan, E.J. Severin, B.J. Doleman, S.A. Beaber, R.H. Grubbs and N.S. Lewis, "Array-based vapor sensing using chemically sensitive, carbon black-polymer resistors", Chemistry of materials, 8, 1996, pp. 2298-2312.

[1.20] E.J. Severin, B.J. Doleman and N.S. Lewis, "An investigation of the concentration dependence and response to analyte mixtures of carbon black/insulating organic polymer composite vapor detectors", Analytical Chemistry, Vol. 72, No. 4, pp. 658-668, 2000.

[1.21] E.J. Severin and N.S. Lewis, "Relationships among resonant frequency changes on a coated quartz crystal microbalance, thickness changes, and resistance responses of polymer – carbon black composite chemiresistors", Analytical Chemistry, Vol. 72, No. 9, pp. 2008-2015, 2000.

[1.22] S.M. Briglin and N.S. Lewis, "Characterization of the temporal response profile of carbon black – polymer composite detectors to volatile organic vapors", Journal of Physical Chemistry B, 107, 2003, pp. 11031-11042.

[1.23] J.W. Gardner and P.N. Bartlett, "Electronic noses: principles and applications", Oxford University Press, Oxford, 1999.

[1.24] J.W.T, Yates, M.J. Chappell and J.W. Gardner, "Novel phenomena-based dynamic model of carbon black/composite vapour sensors", Proceedings of the Royal Society A, 463, 2007, pp. 551-568.

[1.25] P.N. Bartlett and J.W. Gardner, "Odour sensors for an electronic nose", In "Sensors and sensory systems for electronic noses", (ed. J.W. Gardner and P.N. Bartlett) NATO ASI Series, Vol. 212, 1992, pp. 31-51.

[1.26] J.A. Covington, PhD Thesis, University of Warwick, 2001.

[1.27] D.A. Buttry and M.D. Ward, "Measurement of interfacial processes at electrode surface with the electrochemical quartz crystal microbalance", Chemical reviews, 92, 1992, pp. 1355-1379.

[1.28] A. J. Ricco, R. M. Crooks, and G. C. Osbourn, "Surface acoustic wave chemical sensor arrays: New sensitive interfaces combined with novel cluster analysis to detect volatile organic compounds and mixtures," Accounts of Chemical Research, 1998, 31, pp. 289-296.

[1.29] E. Jones, "The pellistor catalytic gas sensor", In "Techniques and mechanisms of gas sensing", (ed. P.T. Moseley, J.O.W. Morris and D.E. Williams), Adam Hilger: Bristol, 1991, pp. 108-138.

[1.30] D.H. Desty (ed.), "Gas chromatography", Butterworths, London, 1958.

[1.31] R.E. Sherman, L. Rhodes (ed.), "Analytical instrumentation: Practical guides for measurement and control", Instrument Society of America, 1996.

[1.32] Agilent Technologies Inc., http://www.agilent.com/, accessed on 24th November 2007.

[1.33] Gasmet Technologies Oy, http://www.gasmet.fi/, accessed on 24th November 2007.

[1.34] C. M. Matzke, R. J. Kottenstette, S. A. Casalnuovo, G. C. Frye-Mason, M. L. Hudson, D. Y. Sasaki, R. P. Manginell and C. Channy Wong, "Microfabricated silicon gas chromatographic microchannels: fabrication and performance", Proceedings of SPIE, Vol. 3511, 1988, pp. 262-282.

[1.35] Sandia National Laboratories, http://www.sandia.gov/, accessed on 24th November 2007.

[1.36] S. Taylor; B. Srigengan; J. R. Gibson; R. Tindall; R. Syms; T. Tate; M.M. Ahmad, "Miniature mass spectrometer for chemical and biological sensing", Proceedings of SPIE, Vol. 4036, pp. 187-193, 2000.

[1.37] Bosch GmbH, http://www.semiconductors.bosch.de/, accessed on 24th November 2007.

[1.38] C.D. Natale, F.A.M. Davide, A. D'Amico, G. Sberveglieri, P. Nelli, G. Faglia, C. Perego, "Complex chemical pattern recognition with sensor array: the discrimination of vintage years of wine", Sensors and Actuators B 24-25, 1995, pp. 801-804.

[1.39] H. Sundgren, I. Lundström, F. Winquist, I. Lukkari, R. Carlsson and S. Wold, "Evaluation of a multiple gas mixture with a simple MOSFET gas sensor array and pattern recognition", Sensors and Actuators B, 2, 1990, pp. 115-123.

[1.40] J.W. Gardner and P.N. Bartlett, "A brief history of electronic noses", Sensors and Actuators B, 18-19, 1994, pp. 211-220.

[1.41] D. Amati, D. Am, N. Blom, M. Ehrat, J. Saunois and H.M. Widmer, "Sensitivity and selectivity of surface acoustic wave sensors for organic solvent vapour detection", Sensors and Actuators B, 7, 1992, pp. 587-591.

[1.42] B. Ross, K. Cammann, W. Mokwa and M. Rospert, "Ultra-microelectrode arrays as transducers for new amperometric oxygen sensors", Sensors and Actuators B, 7, 1992, pp. 758-762.

[1.43] A.P. Lee and B.J. Reedy, "Temperature modulation in semiconductor gas sensing", Sensors and Actuators B, 60, 1999, pp. 35-42.

[1.44] W.M. Sears, K. Colbow and F. Consadori, "General characteristics of thermally cycled tin oxide gas sensors", Semiconductor Science and Technology, Vol. 4, 1989, pp. 351-359.

[1.45] W.M. Sears, K. Colbow and F. Consadori, "Algorithms to improve the selectivity of thermally-cycled tin oxide gas sensors", Sensors and Actuators, 19, 1989, pp. 333.349.

[1.46] A. Heilig, N. Bârsan, U. Weimar, M. Schweizer-Berberich, J.W. Gardner and W. Göpel, "Gas identification by modulating temperatures of SnO_2-based thick film sensors", Sensors and Actuators B, 43, 1997, pp. 45-51.

[1.47] E. Llobet, R. Ionescu, S. Al-Khalifa, J. Brezmes, X. Vilanova, X. Correig, N. Barsan and J.W. Gardner, "Multicomponent gas mixture analysis using a single tin oxide sensor and dynamic pattern recognition", IEEE Sensors Journal, Vol.1, No.3, 2001, pp. 207-213.

[1.48] F. Parret, Ph. Menini, A. Martinez, K. Soulantica, A. Maisonnat and B. Chaudret, "Optimised dynamic temperature operating mode specifically dedicated to micromachined SnO_2 gas sensors", Proceedings of the Eurosensors XIX conference, 2005.

[1.49] Ph. Menini, F. Parret, C. Tropics and A. Martinez, "Accurate measurement of CO concentration in gas mixture with a single SnO_2 semi-conducting gas sensor", Proceedings of the Eurosensors XX conference, 2006.

[1.50] Y.S. Kim and Y.S. Yang, "Additional thermodynamic feature extraction from chemoresistive carbon black-polymer composite sensors by temperature modulation", Sensors and Actuators B, 121, pp. 507-514.

[1.51] V. Demarne and A. Grisel, "An integrated low-power thin-film gas sensor on silicon", Sensors and Actuators, 13, 1988, pp. 301-313.

[1.52] I. Stoev and D. Kohl, "An integrated gas sensor on silicon substrate with sensitive SnO_x layer", Sensors and Actuators B, 2, 1990, pp. 233-236.

[1.53] I. Simon N. Barsan, M. Bauer and Udo Weimar, "Micromachined metal oxide gas sensors: opportunities to improve sensor performance", Sensors and Actuators B, 73, 2001, pp. 1-26.

[1.54] D.C. Giancoli, "Physics 4th Edition", Prentice Hall, 1995.

[1.55] A. Pike and J.W. Gardner, "Thermal modelling and characterisation of micropower chemoresistive silicon sensors", Sensors and Actuators B, 45, 1997, pp. 19-26.

[1.56] S.M. Lee, D.C. Dyer and J.W. Gardner, "Design and optimisation of a high-temperature silicon micro-hotplate for nanoporous palladium pellistors", Microelectronics Journal, 34, 2003, pp. 115-126.

[1.57] D. Lee, W. Chung, M. Choi and J. Baek, "Low-power micro gas sensor", Sensors and Actuators B, 33, 1996, pp. 147-150.

[1.58] S. Astié, A.M. Gué, E. Scheid, L. Lescouzères and A. Cassagnes, "Optimization of an integrated SnO2 gas sensor using a FEM simulator", Sensors and Actuators A, 69, pp. 205-211.

[1.59] G. Sberveglieri, W. Hellmich, G. Müller, "Silicon hotplates for metal oxide gas sensor elements", Microsystem Technologies, 3, 1997, pp. 183-190.

[1.60] W. Qu, W. Wlodarski and M. Austin, "Microfabrication and reliability study of sapphire based Ti/Pt-electrodes for thin-film gas sensor applications", microelectronics Journal, 31, 2000, pp. 561-567.

[1.61] D. Lee, J. Huh and D. Lee, "Classifying combustible gases using micro-gas sensor array", Sensors and Actuators B, 93, 2003, pp. 1-6.

[1.62] F. Solzbacher, C. Imawan, H. Steffes, E. Obermeier and M. Eickhoff, "A highly stable SiC based microhotplate NO_2 gas sensor", Sensors and actuators B, 78, 2001, pp. 216-220.

[1.63] M. Rydberg and U. Smith, "Long-term stability and electrical properties of compensation doped Poly-Si IC-resistors", IEEE Transactions on Electron Devices, Vol. 47, No.2, 2000, pp. 417-426.

[1.64] I. Gràcia, J. Santander, C. Cané, M. C. Horrillo, I. Sayago and J. Gutierrez, "Results on the reliability of silicon micromachined structures for semiconductor gas sensors", Sensors and Actuators B, 77, 2001, pp. 409-415.

[1.65] Z. Tang, S.K.H. Fung, D.T.W. Wong, P.C.H. Chan, J.K.O. Sin and P.W. Cheung, "An integrated gas sensor based on tin oxide thin-film and improved micro-hotplate", Sensors and Actuators B, 46, 1998, pp. 174-179.

[1.66] F. Udrea, J.W. Gardner, D. Setiadi, J.A. Covington, T. Dogaru, C.C. Lu and W.I. Milne, "Design and simulations of SOI CMOS micro-hotplate gas sensor", Sensors and Actuators B, 78, 2001, pp. 180-190.

CHAPTER 2

Design and simulation of novel SOI-CMOS single crystal silicon micro-hotplates

2.1 Introduction

Two major issues that make the commercialisation of micro-hotplates for gas sensors problematic have been discussed previously, namely: (1) no micro-hotplate which is both CMOS compatible and sufficiently thermally stable has been developed, and (2) the micro-hotplate design has not been optimised to minimise power consumption.

In this chapter, we propose a novel micro-hotplate design to obviate these problems. Here the source and drain region of a standard SOI-CMOS process are used as integrated resistive heaters to form micro-hotplates, achieving better thermal stability than more traditional polysilicon heaters. Furthermore, these micro-hotplates have been designed to have significantly lower power consumption than previously reported designs. These design concepts have been confirmed by computational FEM (Finite Element Method) simulations.

2.2 Design and layout of the novel micro-hotplates

2.2.1 Choice of material and starting wafer

The choice of resistive heater material and type of silicon wafer are crucial factors when designing novel micro-hotplates that are both CMOS compatible and thermally stable. Tables 2.1 and 2.2 summarise the principal semiconductor and metal materials in a CMOS process and some of their important material properties for micro-hotplate

design [2.1, 2.2]. Here we proposed to use the $n+$ or $p+$ regions of an SOI-CMOS process as resistive heater materials. They are single crystal silicon and thus are expected to have better thermal stability than polycrystalline silicon because they do not have highly reactive grain boundaries [2.3] as discussed in chapter 1. Metals were not chosen because of the following reasons:

1. All of the metals are polycrystalline and thus will suffer from the same problem as polysilicon, *e.g.* chemical reaction at grain boundaries.
2. Aluminium and copper resistors are easily damaged by electromigration - especially at high temperatures.
3. The resistances of aluminium and copper are much smaller than platinum (traditional heater material), and thus it is expected that designing a resistive metallic heater with a small area is problematic.

In addition the choice of $n+$ or $p+$ is beneficial by having the lowest dopant concentrations (and thus the lowest resistivity) of all the silicon layers in CMOS ($n+$ or $p+$ region have typically 10^{20}-10^{21} cm^{-3} whereas n or p region has 10^{16}-10^{17} cm^{-3}) and thus will allow resistive heaters to operate at lower voltages. To reduce thermal losses and to simplify the fabrication process, it was decided to use SOI (Silicon On Insulator) wafers, allowing a silicon dioxide layer below the heater unlike with previous micro-hotplates [2.4].

Table 2.1. Material properties of semiconductors used in CMOS.

Property	c-Si, $n+$ ($10^{20}cm^{-3}$)	c-Si, $p+$ ($10^{20}cm^{-3}$)	c-Si, n ($10^{17}cm^{-3}$)	c-Si, p ($10^{17}cm^{-3}$)	Poly-Si
Resistivity [Ω m]	7.70×10^{-6}	1.17×10^{-5}	8.38×10^{-4}	2.02×10^{-3}	10^{-4}-10^{-3}
Thermal conductivity [W/(m·K)]	168				34
Heat capacity [J/K/kg]	678				678
Melting point [°C]	1410				-

Table 2.2. Material properties of metals used in CMOS compared to platinum (traditional heater material).

Property	Al	Cu	W	Pt
Resistivity [$10^{-8}\Omega$ m]	2.65	1.65	5.46	10.6
Thermal conductivity [W/(m·K)]	236	403	177	72
Heat capacity [J/K/kg]	904	385	134	133
Melting point [°C]	660	1083	3410	1772

2.2.2 Design of standard devices aiming at ultra-low power consumption

Here the structure of the micro-hotplate was decided to be the solid diaphragm type rather than the suspended micro-bridge type (both described in chapter 1) *i.e.* the resistive heater is embedded in a thin continuous membrane made of silicon dioxide and silicon nitride. This makes it possible to use a DRIE (Deep reactive ion etch) to back etch making the chip size smaller as will be detailed later.

The resistive heater structure must be strategically designed to fit the material properties of $n+$ or $p+$ silicon. The resistivity of $n+$ or $p+$ silicon is much higher than that of metals (*e.g.* the resistivity of $n+$ with 10^{20} cm^{-3} doping is 7.70×10^{-6} Ωm whereas that of pure aluminium is 2.65×10^{-8} Ωm as shown in tables 2.1 and 2.2), though their thermal conductivity (168 W/(m·K) as shown in table 2.1) is comparable to many metals (*e.g.* thermal conductivity of aluminium is 236 W/(m·K) as shown in table 2.2). One possible issue which can be caused by these material properties is explained as follows. The total power P of a resistive heater and tracking is given by:

$$P = R_H I^2 + R_T I^2 \tag{2.1}$$

where R_H and R_T are resistances of the heater and track, and I is the electrical current. The first term is the Joule heat generated to raise the temperature of membrane, whilst most of the heat generated by the tracks is dissipated to the substrate. Moreover, a high track resistance of single crystal silicon will be an issue because it will reduce the voltage dropped across the heater itself. Therefore wider tracks, which have a lower resistance, are preferred. However, from a thermal point of view, wider tracks will cause more heat to be dissipated along the tracks and be dissipated into the substrate. To solve these conflicting design issues, metal track structure is proposed for standard devices. Having lower resistivity, even a narrow metal track can supply a current to the

heater suppressing the generation of the Joule heat as well as the heat dissipation to the substrate. A cross-section of an SOI resistive sensor employing this structure is shown in figure 2.1. There are three candidates of the material for metal track: aluminium, copper and tungsten. Aluminium is the most common metallization layer in CMOS process and thus is generally available. However its use for micro-hotplate is limited as it tends to suffer from electro-migration at high temperatures. Copper has a lower resistivity than aluminium and thus the lower power consumption of any associated circuitry is expected. However, it also suffers from electro-migration problem. Unlike aluminium or copper, tungsten is suitable for high-temperature applications, though its resistivity is larger than aluminium making the power consumption of any associated circuitry higher.

Considering the discussion in the previous chapter, the following rules for the design were set in order to minimise the power consumption:

1. Heated area should be designed to be small enough so that the convection heat loss, which is proportional to the heated area and the most significant in traditional micro-hotplates, is much less significant than the conduction heat loss (e.g. heated area: less than 0.02 mm^2 as mentioned in the previous chapter).
2. Provided that the first guideline is satisfied, a large membrane to heater ratio should be large enough (*e.g.* 10) to decrease the conduction heat loss.

Considering the above rules, two types of micro-hotplates with $n+$ single crystal silicon were designed: a large micro-hotplate with membrane radius of 282 μm and heater radius of 75 μm (heated area: 0.018 mm^2, membrane to heater ratio: 3.8), which satisfies rule 1, and a small micro-hotplate with membrane radius of 28 μm and heater radius of 12 μm (heated area: 0.00045 mm^2, membrane to heater ratio: 12.5) which satisfies both rules 1 and 2 as is shown in figures 2.2 (a) and (b). Those devices will be referred to as "large standard" micro-hotplate and "small standard" micro-hotplate. The shapes of both membranes and heaters have been chosen to be circular in order to reduce the possibility of membrane failure due to stress. It should be noted that silicon tracks with exactly the same shape as the metal ones are located under the metal track in the "standard small" micro-hotplate to support the narrow metal track (width: 4 μm).

The resistive heater is made of two parallel resistors, and each resistor is made of three concentric half rings which are serially connected. The widths of the rings have been varied with the outer ring being wider. This has been implemented as the outer region loses more heat through conduction to the membrane than the inner region, thus the structure will improve the temperature uniformity. In addition, there are a silicon heat spreading plate inside the silicon heaters and a metal heat spreading plate (metal 2) which has the same area as the heater to again enhance temperature uniformity.

The resistive heaters can also be used as a temperature sensor. If the resistance of a heater is measured then the temperature dependence of the heater resitivity is defined as [2.5]:

$$\rho(T) = \rho_a \left[1 + \alpha_1 (T - T_a) + \alpha_2 (T - T_a)^2\right] \tag{2.2}$$

where $\rho(T)$ is the electrical resistivity, T is the temperature, T_a is the ambient temperature (27 °C), ρ_a is the resistivity at temperature T_a, α_1, α_2 are the temperature coefficients of resistance.

In addition, a dual metal track structure with a wide track for current supply and a narrow track for voltage sensing has been added in order to perform 4 probe resistance measurement as shown in figure 2.2. Therefore, a precise resistance measurement of the heaters is achieved by negating the resistance of the metal tracks (and drift).

The micro-hotplates were designed for the XFAB foundry (Germany) using its XI10 process. This is a 1.0 micron SOI process with three metal layers, and allows the use of tungsten as well as aluminium. This three metal layer process makes it possible to fabricate resistive track, metal heat spreading plate and resistive electrodes (discussed later) without any post-CMOS processing. The sheet resistance of $n+$ is 40 Ω, and the resistances of the resistive heater structure is approximately 800 Ω for both the large and small standard micro-hotplates at room temperature with the temperature coefficients of resistance is $\alpha_1 = 1.35 \times 10^{-3}$ /K and $\alpha_2 = 0.29 \times 10^{-6}$ /K^2 [2.5].

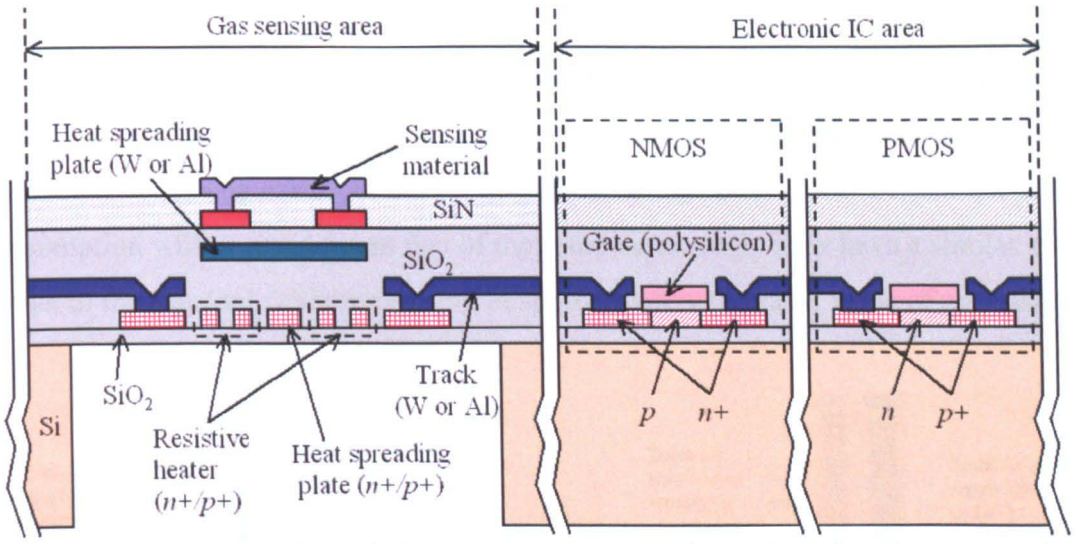

Figure 2.1. Structure of a resistive gas sensor employing SCS micro-hotplates with metal tracks. The gas sensor is integrated with CMOS circuitry.

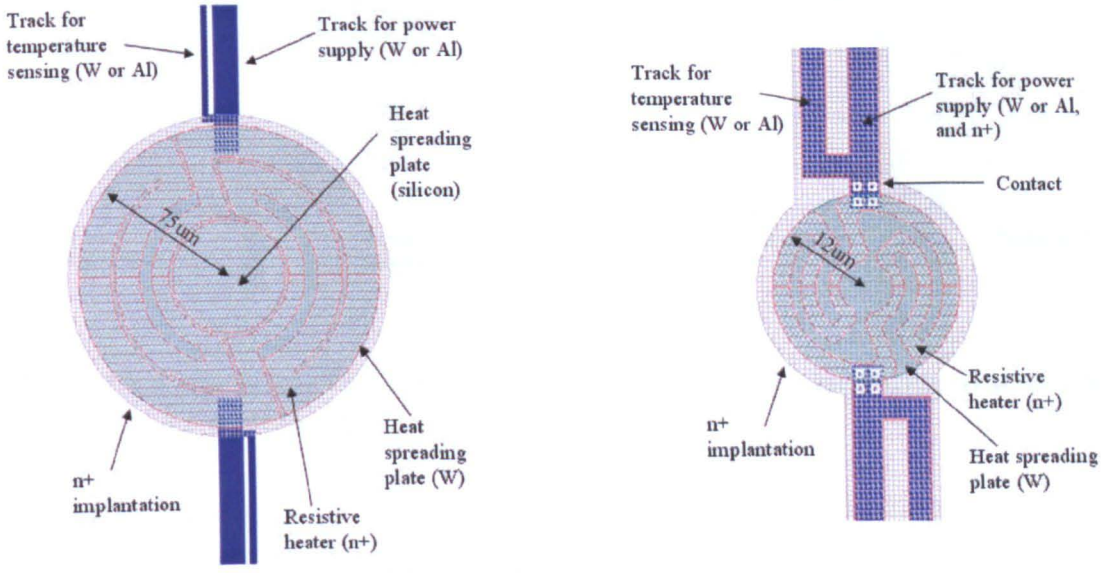

(a) (b)

Figure 2.2. Standard devices for (a) large and (b) small micro-hotplates.

2.2.3 Device variations

Apart from the standard devices, a number of other types of micro-hotplates were created. They were deviations from the standard devices of large (radius: 282 μm) and small micro-hotplates (radius: 150 μm) in terms of (a) heater radius, (b) heater resistance, (c) heater material and (d) metal heat spreading plate. Furthermore various types of resistive electrodes were designed and integrated with the micro-hotplates.

(a) Heater radius

Micro-hotplates with greater heater radii than the standard devices were designed. A larger heater area offers the opportunity to create longer electrodes, which will make deposition of sensing materials easier. The disadvantage of this will be that the power consumption will be greater than that of the standard devices. They have a similar shape to that of the standard devices resulting in approximately the same value of resistance.

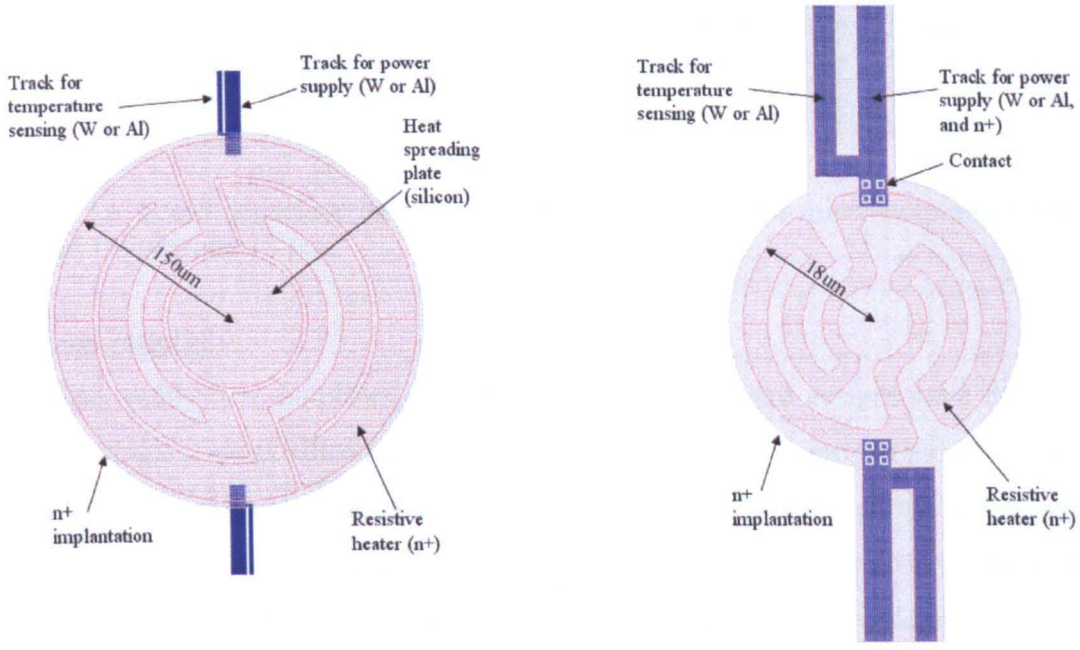

Figure 2.3. Large heater for (a) large and (b) small micro-hotplates with radii of 150 μm and 18 μm, respectively.

(b) Heater resistance

A large micro-hotplate and a small micro-hotplate both with lower resistance heaters than the standard devices were designed. Their resistances were designed to be *ca.* 200 Ω for large and small micro-hotplates. Thus it was expected that the devices would have an advantage of low operating voltage, making them suitable for battery operation. As with the standard devices, the widths of the resistive heater rings of these devices are varied with the outer ring being to improve temperature uniformity.

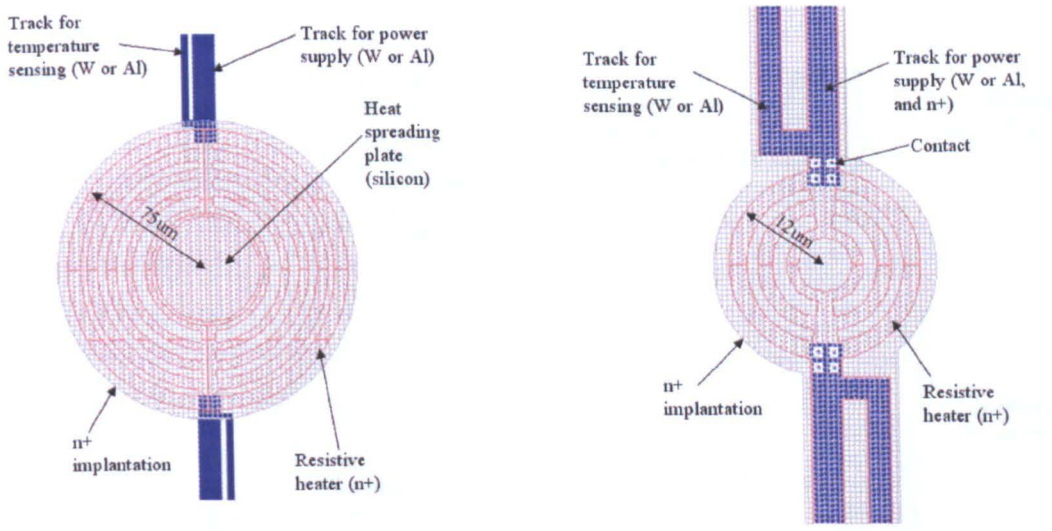

(a) (b)

Figure 2.4. Small resistance heater for (a) large and (b) small micro-hotplates with radii of 150 μm and 18 μm.

(c) Heater material

Large and small micro-hotplates with the shape of the standard designs were designed with $p+$ single crystal silicon and polysilicon. The electrical properties of $n+$, $p+$, polysilicon are summarized in table 2.3 [2.5]. These devices will operate in the same way as the standard devices (made of $n+$ silicon) apart from the operating voltages due to the change in resistivities. However, as mentioned earlier, we would expect better thermal stability of $n+$ or $p+$ than polysilicon, and thus reliability tests will be performed to confirm this (detailed in chapter 3).

Table 2.3. Electrical properties of $n+$, $p+$ and polysilicon.

	n+	p+	polysilicon
Sheet resistance [Ω]	40	65	30
Temperature coefficient of resistance α_1 [1/K]	1.35×10^{-3}	1.51×10^{-3}	0.85×10^{-3}
Temperature coefficient of resistance α_2 [1/K^2]	0.29×10^{-6}	0	0.35×10^{-6}

(d) Metal heat spreading plate

Micro-hotplates without metal heat spreading plates were also designed as shown in figure 2.5. The temperature uniformity of these devices will be compared with the standard devices to confirm the effect of the metal heat spreading plates.

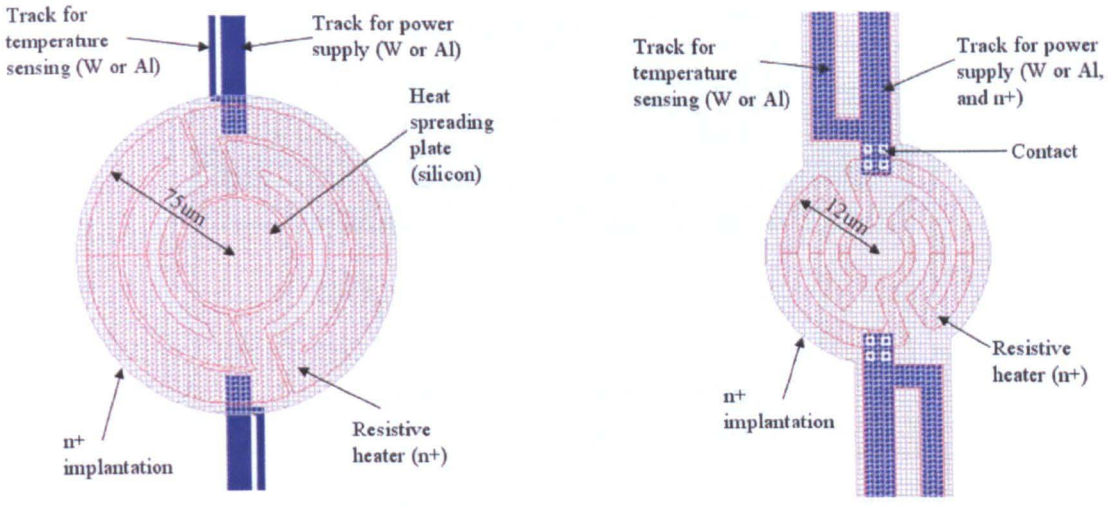

(a) (b)

Figure 2.5. (a) Large and (b) small micro-hotplates without heat spreading plate.

(e) Resistive track

Micro-hotplates with sector shape silicon tracks rather than metal tracks were designed. A cross-section of an SOI calorimeter employing these tracks is shown in figure 2.6. These are sector shape track designs (angle of 40°) for large and small micro-hotplates as shown in figure 2.7. This design is more suitable for use in a micro-calorimeter configuration. These devices contain no metals in the membrane area and thus can be operated at, for example, 500 °C, though still are standard aluminium based on an SOI CMOS process. This sector shape track generates more heat in the inner region of the track and so can be used more efficiently to raise the temperature of heater area. The silicon track is connected to metal outside the membrane, where the temperature approximately equals to that of the ambient. Again, 4 probe temperature sensing method is employed to measure temperature accurately, and thus there exist tracks both for current supply and for temperature sensing.

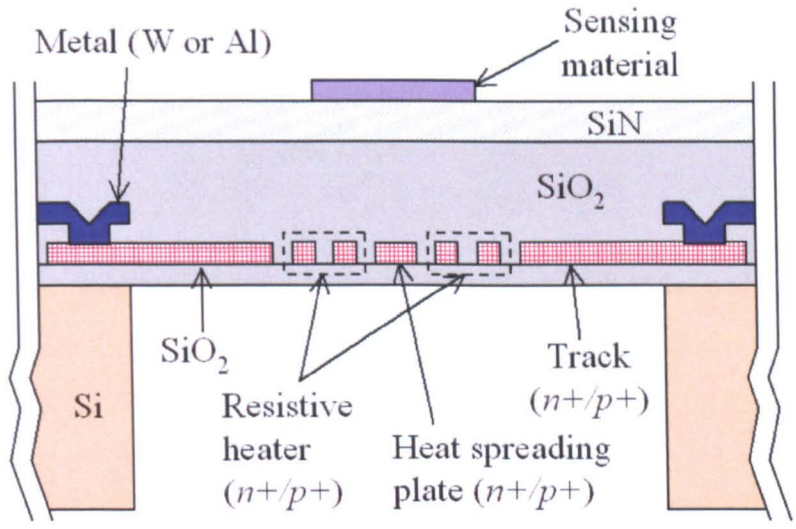

Figure 2.6. Structure of a calorimetric gas sensor employing SCS micro-hotplates with silicon track.

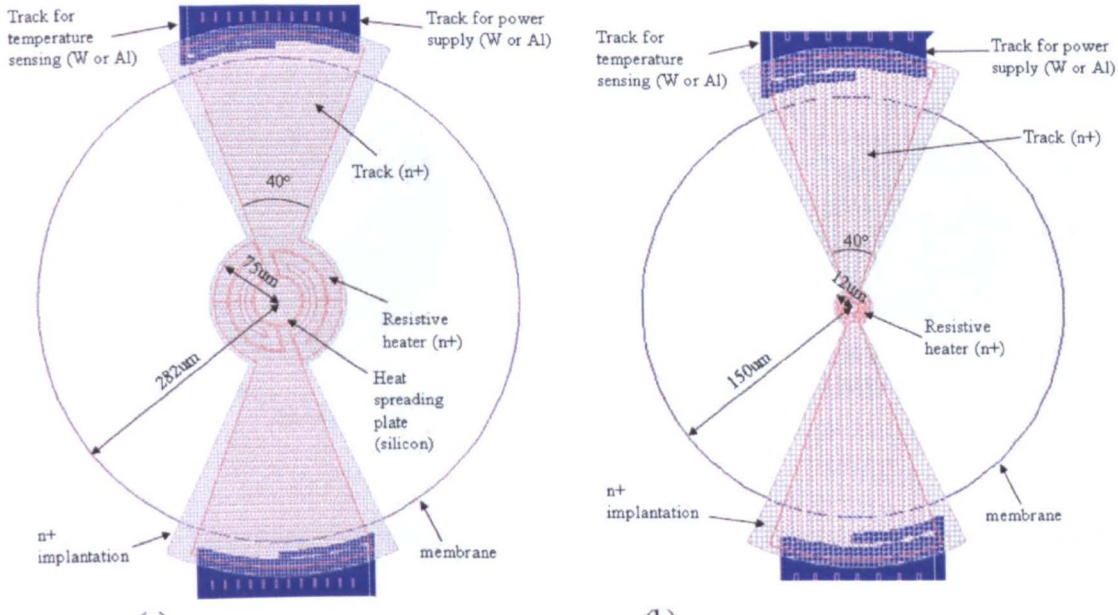

Figure 2.7. (a) Large micro-hotplate with silicon track (angle 40°), and (b) small micro-hotplate with silicon track (angle 40°).

(f) Resistive Electrodes

6 types of resistive electrodes for large micro-hotplates and 3 types for small micro-hotplates were designed. Typical designs of resistive electrodes are shown in figure 2.8. Most of these have an interdigitated shape thus there is a high aspect ratio. This can be used to reduce the resistance of sensing film with high sheet resistance. There are some others with simple parallel resistors. The resistance of a gas sensing film deposited onto

the electrodes is calculated by:

$$R = \frac{R_{sheet}}{r} \tag{2.3}$$

where R_{sheet} is the sheet resistance, r is the aspect ratio, which is defined as

$$r = n\frac{L}{d} \tag{2.4}$$

where n is the number of interdigitated fingers, d is the electrode gap and L is the length of the electrodes. All the variations in electrode geometries are shown in table 2.4.

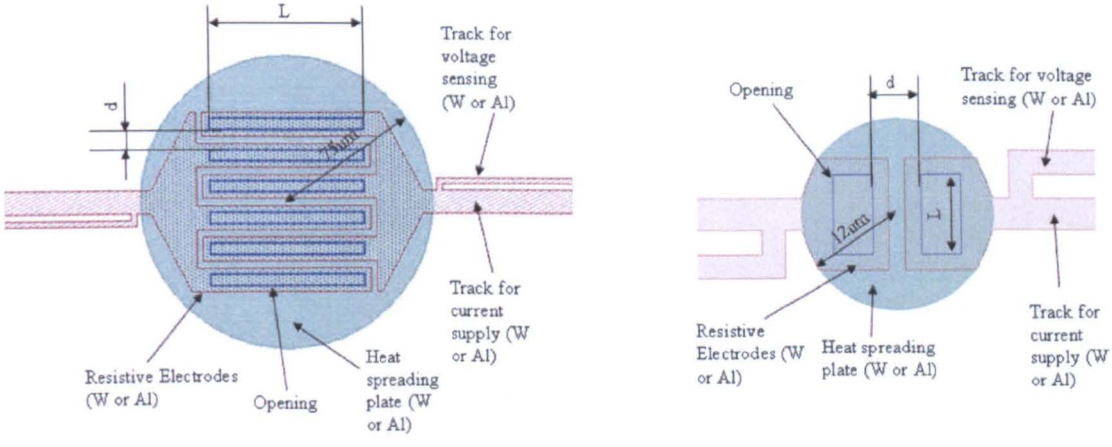

(a) (b)

Figure 2.8. Typical resistive electrodes for (a) large micro-hotplate and (b) small micro-hotplate.

Table 2.4. List of all the resistive electrodes.

Membrane radius [μm]	Heater radius [μm]	L [μm]	d [μm]	n	Aspect ratio
75	80	10	10	5	40
150	180	10	10	13	234
75	80	12	12	5	33.3
75	80	25	25	3	9.6
75	80	20	20	4	16
12	10	6	6	1	1.7
18	16	6	6	2	5.3
12	6	10	10	1	0.6

2.2.4 General layout

All the micro-hotplates described in this chapter were laid out in 5 silicon chips. They are labelled SRL287, SRL288, SRL289, SRL290 and SRL291 with each chip being 3.75 mm by 3.75 mm as shown in figures 2.9 (a) - (e). Figure 2.9 (f) is an outline of a single chip. Each chip has 5 large micro-hotplates with the labels of A_1, A_2, B, C and D, and 4 small micro-hotplates labelled e, f, g and h (Note: A_1 and A_2 are identical, thus are sometimes referred to as just "A"). For example, device A of chip SRL287 is referred to as SRL287A. All the micro-hotplates designed are listed in table 2.5.

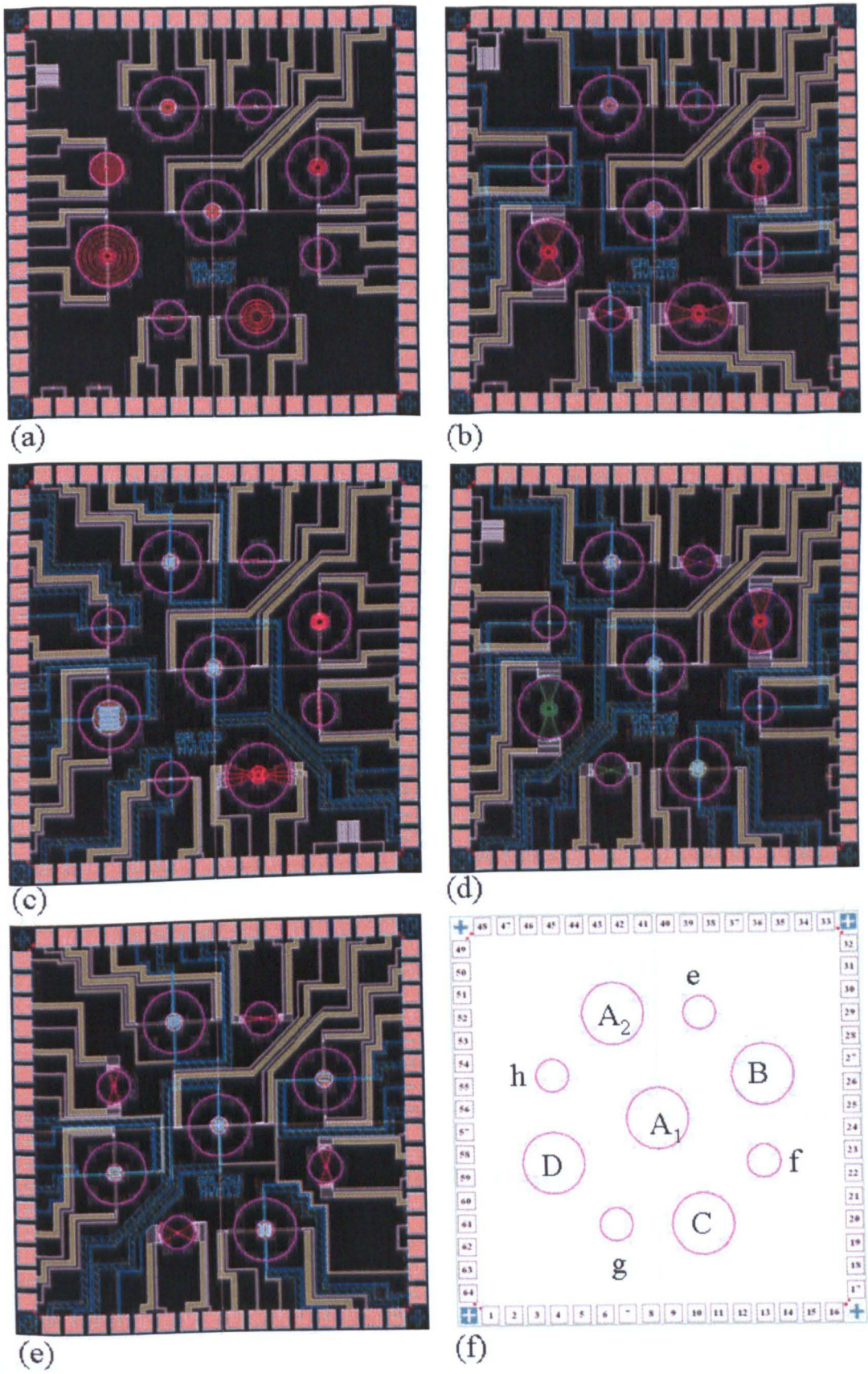

Figure 2.9. Individual chip lay-out. (a) SRL287, (b) SRL288, (c) SRL289, (d)SRL290, (e) SRL291, (f) labelling of each micro-hotplate.

Table 2.5. List of all the micro-hotplates designed. "n" for heater shape indicates normal type heater and "l" low resistance type heater.

Name	Membrane radius [μm]	Heater radius [μm]	Heater material	Heater shape	Track	Heat spreading plate	Aspect ratio
SRL287A	282	75	*n*+	n	metal	yes	-
SRL287B	282	75	*n*+	n	metal	no	-
SRL287C	282	150	*n*+	n	metal	no	-
SRL287e	150	12	*n*+	n	metal	yes	-
SRL287f	150	12	*n*+	n	metal	no	-
SRL287g	150	18	*n*+	n	metal	no	-
SRL288C	282	75	*n*+	n	*n*+/40°	no	-
SRL288f	150	12	*n*+	n	metal	no	0.6
SRL288g	150	12	*n*+	n	*n*+/40°	no	1.7
SRL288h	150	18	*n*+	n	metal	no	5.3
SRL289A	282	75	*n*+	n	metal	yes	40
SRL289B	282	75	*n*+	l	metal	no	-
SRL289C	282	75	*n*+	l	*n*+/40°	no	-
SRL289D	282	150	*n*+	n	metal	yes	234
SRL289f	150	12	*n*+	l	metal	no	-
SRL289g	150	12	*n*+	n	metal	yes	1.7
SRL289h	150	18	*n*+	n	metal	yes	5.3
SRL290A	282	75	*p*+	n	metal	yes	40
SRL290B	282	75	*p*+	n	*p*+/40°	no	-
SRL290C	282	75	poly	n	metal	yes	40
SRL290D	282	75	poly	n	poly/40°	no	-
SRL290e	150	12	*p*+	n	*p*+/40°	no	-
SRL290f	150	12	*p*+	n	metal	yes	1.7
SRL290g	150	12	poly	n	poly/40°	no	-
SRL290h	150	12	poly	n	metal	yes	1.7
SRL291A	282	75	*n*+	n	metal	no	33.3
SRL291B	282	75	*n*+	n	metal	no	9.6
SRL291C	282	75	*n*+	n	metal	no	16
SRL291D	282	75	*n*+	n	metal	no	16
SRL291f	150	12	*n*+	n	*n*+/40°	no	-
SRL291h	150	18	*n*+	n	*n*+/40°	no	-

2.3 Simulations of proposed micro-hotplates

2.3.1 Aims of simulations

FEM simulations were performed on a PC to check the operation of these designs prior to fabrication. The aims were to predict power consumption, temperature uniformity and operating voltage before fabrication to confirm that the proposed design concepts are correct.

2.3.2 2D electro-thermal modelling of micro-hotplates

Since the geometry of the micro-hotplates is a very thin membrane (thickness: *ca.* 5 μm, radius: 282 μm or 150 μm), it is possible to model them as a 2-D structure to save simulation time. In order to carry out 2D electro-thermal simulations, it was necessary to create a finite element model of these micro-hotplates. The Joule heating and heat dissipation are described in the following equations:

$$\sigma(T)(\nabla V)^2 = P_{conduction} + P_{convection} + P_{radiation} \tag{2.5a}$$

$$\nabla \cdot [\sigma(T)\nabla V] = 0 \tag{2.5b}$$

$$\sigma(T) = 1 \Big/ \left\{ \rho_a \left[1 + \alpha_1 (T - T_a) + \alpha_2 (T - T_a)^2 \right] \right\} \tag{2.5c}$$

where $\sigma(T)$ is the electrical conductivity, T is the temperature, T_a is the ambient temperature (27 °C), V is the electrical potential, ρ_a is the resistivity, α_1, α_2 are the temperature coefficients of resistance, $P_{conduction}$, $P_{convection}$, $P_{radiation}$ are the power losses per unit volume caused by different heat loss mechanism. The mechanism of power loss by conduction along the membrane is denoted as:

$$P_{conduction} = -\nabla \cdot (\kappa \nabla T) \tag{2.6}$$

where κ is thermal conductivity and calculated as follows:

$$\kappa = \left(t_{SiN}\kappa_{SiN} + t_{SiO2}\kappa_{SiO2} + t_{Si}\kappa_{Si} + t_w\kappa_w\right) / \left(t_{SiN} + t_{SiO2} + t_{Si} + t_w\right) \times c \tag{2.7}$$

where t is the thickness of each film and c is the correction factor that corrects for different thickness of membrane denoted as

$$c = \left(t_{SiN} + t_{SiO2} + t_{Si} + t_w\right) / \left(t_{SiN} + t_{SiO2}\right) \tag{2.8}$$

For convection, *i.e.* power loss to the ambient air is modelled by [2.6]:

$$P_{convection} = \left\{ \left[0.104(T-T_a)+4.129\times10^{-4}(T-T_a)^2\right] / 5.0\times10^{-7} \right\} / (t_{SiN}+t_{SiO2}) \quad [mW/m^3] \tag{2.9}$$

The denominator, which is the thickness of membrane in equation (2.9), is needed to correct the equation for our designs. Radiation power loss is described as follows:

$$P_{radiation} = 2\varepsilon\sigma(T^4 - T_a^4)/(t_{SiN}+t_{SiO2}) \tag{2.10}$$

where the emissivity constant ε is assumed to be unity and the value of the Stefan-Boltzmann constant σ is 5.67×10^{-8} W/m^2/K^4. The edge of the membrane is assumed to be at ambient temperature (*i.e.* 300 K).

2.3.3 Material properties and film thickness

Table 2.6 lists the material properties used in the computer simulations. The heater is made of *n*+ silicon and the electrical properties are taken from [2.5]. All other material properties are common values taken from [2.1]. The thicknesses of all the layers are listed in table 2.7.

Table 2.6. Material properties used in simulations.

		Si	W	SiO_2	SiN
Density	[kg/m^3]	2330	19350	2200	3100
Thermal conductivity	[W/m/K]	168	177	1.4	20
Specific heat capacity	[J/K/kg]	678	134	730	700
Resistivity	[Ωm]	1.00E-05	1.20E-07	-	-
Temperature coefficients of resistance	α_1 [1/K]	1.35E-03	2.05E-03	-	-
	α_2 [1/K^2]	2.90E-07	3.00E-07	-	-

Table 2.7. Thickness of the film used in simulations.

Si	250 nm
W	300 nm
SiO_2	3800 nm
SiN	550 nm

2.3.4 Results of simulations and discussions

The following devices were simulated: SRL287A, SRL287B, SRL288C, SRL289B, SRL287e and SRL287f . They may be referred to as "large, standard", "large, without spreading plate", "large, silicon track", "large, small resistance", "small, standard", "small, without spreading plate".

The commercial software COMSOL® (COMSOL, US, Version 3.3) was used to solve the 2D electro-thermal problem. An automatically generated mesh of triangles was used as shown in figures 2.10 and 2.11.

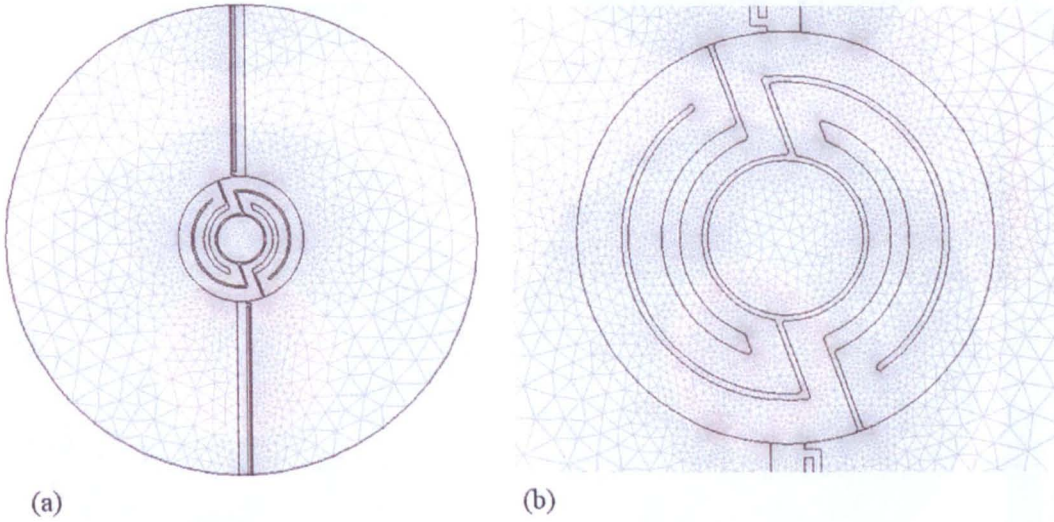

(a) (b)

Figure 2.10. Meshed model for large standard micro-hotplate (SRL287A). (a) Entire model, and (b) magnified model of the heater region.

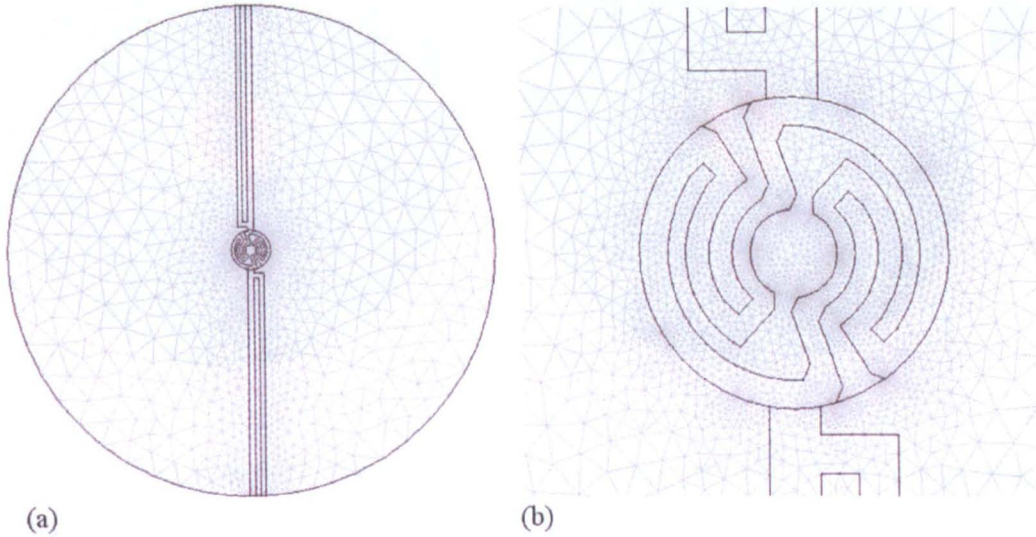

(a) (b)

Figure 2.11. Meshed model for small standard micro-hotplate (SRL287e). (a) Entire model, and (b) magnified model of the heater region.

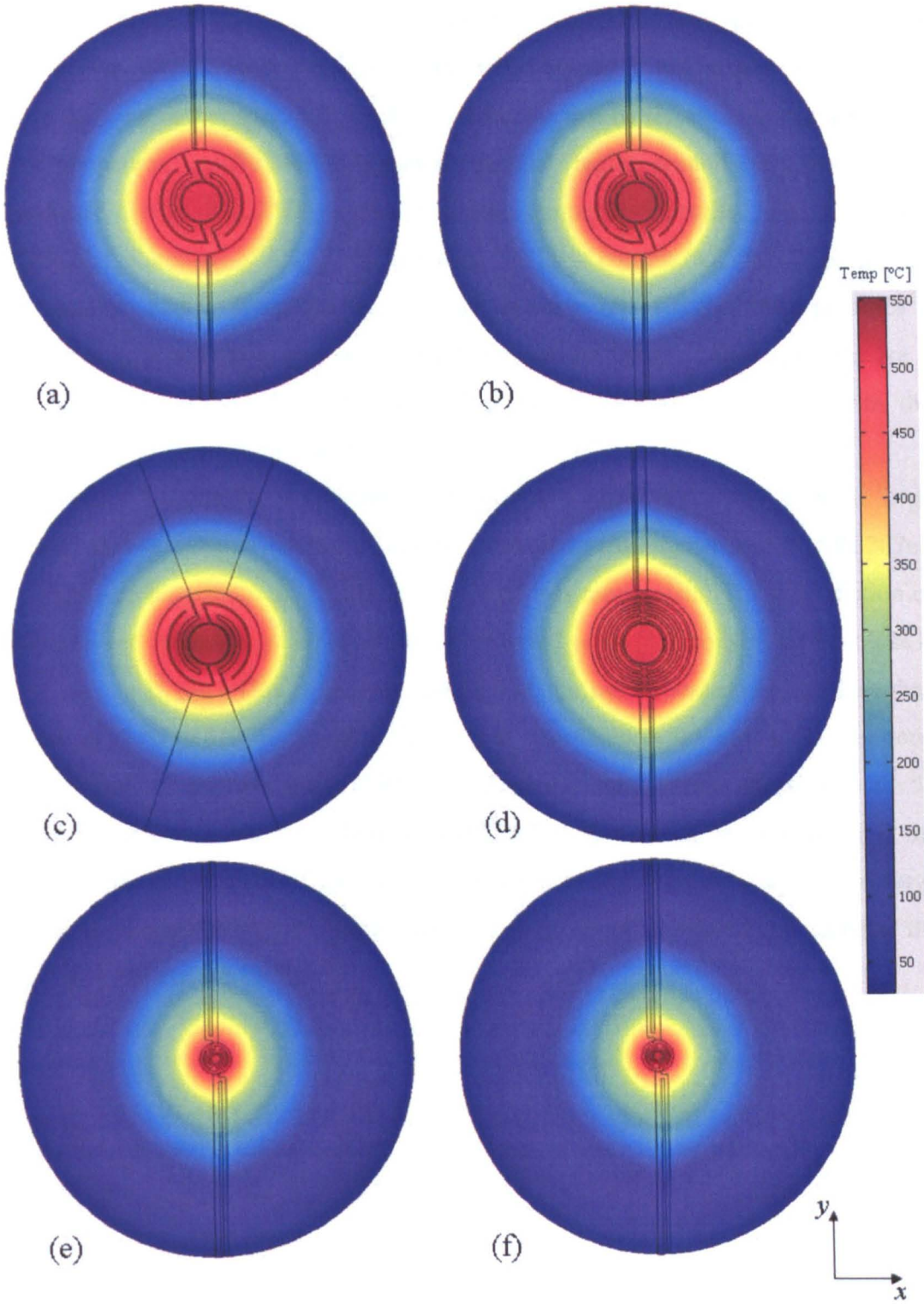

Figure 2.12. Temperature profiles of micro-hotplates at 500 °C. (a) Large, standard (SRL287A), (b) large, without heat spreading plate (SRL287B), (c) large, silicon track (SRL288C), (d) large, small resistance (SRL289B), (e) small, standard (SRL287e), (f) small, without heat spreading plate (SRL287f).

Temperature profiles over the membranes at 500 °C for all the micro-hotplates, are shown in figure 2.12. Here, temperatures were calculated by averaging over the area of the heater. Temperature profiles of all micro-hotplates are nearly uniform and without any central hot spot. The small resistance design (SRL289C) shows a slightly elliptic temperature profile with a higher temperature region around the tracks, whilst the standard design (SRL287A) shows a circular temperature profile. The reason for this is the large amount of Joule heat caused by the large current required to operate the small resistive heater. Even the silicon track micro-hotplate (SRL288B) provides a nearly circular temperature profile despite having wider tracks. These profiles are a result of balancing out the heat generated at the inner region of tracks with the dissipated power through the tracks.

Figure 2.13 shows contribution of each heat dissipation path for both the large standard micro-hotplate (SRL287A) and the small standard micro-hotplate (SRL287e). It is concluded that conduction is the main power loss mechanism. The contribution of convection and radiation are far less than the reported value (e.g. convection heat loss is 2/3 of total in [2.6]). This is because the area of the micro-heater is much less than reported in [2.6] (0.018 mm^2 and 0.00045 mm^2 compared to 0.5 mm^2). Furthermore, the small standard micro-hotplate (SRL287e) consumes only 26 mW compared with 53 mW of the large standard micro-hotplate (SRL287A). Given that the conduction is the main heat dissipation mechanism; this ultra-low power consumption is due to the large heater to membrane ratio of the small standard micro-hotplate. Hence this satisfies the rules 1 and 2 discussed earlier.

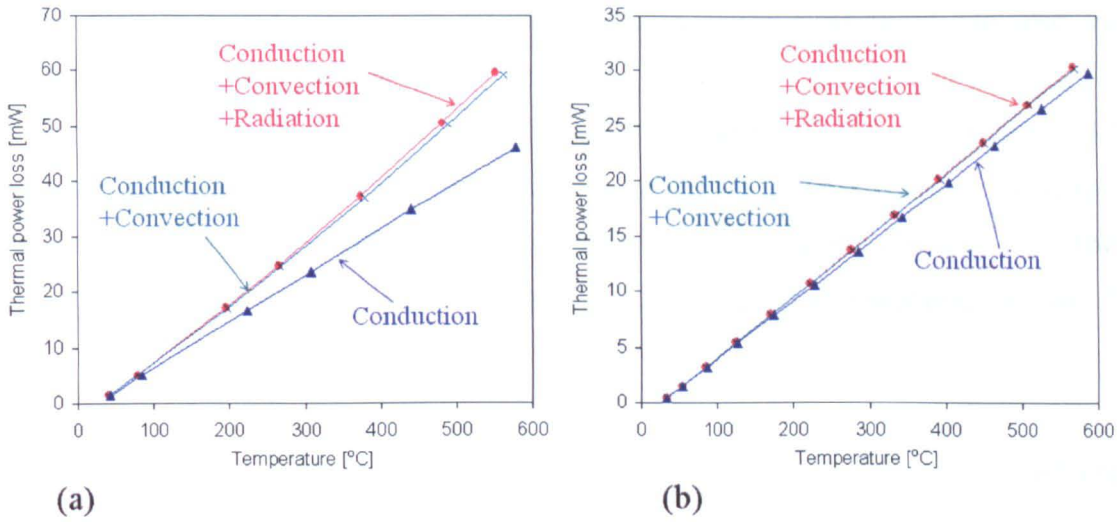

Figure 2.13. Simulated contribution of each heat dissipation mechanism for (a) "large standard" micro-hotplate (SRL287A), and (b) "small standard" micro-hotplate (SRL287e).

Figure 2.14 shows that power consumption of all of the simulated micro-hotplates. All of the micro-hotplates consume less than 70 mW when operated at 500 °C. This value is ideal for handheld, battery powered gas sensing applications. The silicon track micro-hotplate (SRL288C) consumes about 20 mW more power than the tungsten tracks (SRL287A). This is due to the larger conductive losses and Joule heat generated in silicon tracks and thus is less efficient. It should be worth pointing out that the heat spreading plates have only little effect on power consumption for both large and small micro-hotplates.

Figures 2.15 and 2.16 show the temperature profiles along the x and y axes of large and small micro-hotplates both with and without heat-spreading plate (refer to figure 2.12 for the definition of x and y axes). Heat-spreading plate design was shown to reduce the overall temperature variance by more than half i.e. from ± 48 °C to only ± 23 °C for large micro-hotplates and from ± 45 °C to only ± 21 °C for small micro-hotplates.

Figure 2.17 shows the relation between the operating voltage and temperature for all of the simulated micro-hotplates. "Large, small resistance (SRL289B)" micro-hotplates can be operated at the lowest voltage as expected. It is operated at 500 °C for less than 5 V and thus can easily be controlled by CMOS circuitry unlike all the other

large micro-hotplates. The small standard micro-hotplate (SRL287e) can also be operated at 500 °C for less than 5 V.

The slopes of the operating voltage vs temperature curves in figure 2.17 gradually decrease from the room temperature to *ca.* 200 °C and are almost constant (*i.e.* the curve is linear) above 200 °C. The reason of this behaviour is explained here. The operating voltage V is related with the heater resistance R and the power consumption P by:

$$V = \sqrt{PR} \tag{2.11}$$

Assuming the temperature is proportional to the power consumption and the resistance is independent of the temperature, the operating voltage is proportional to the square root of the temperature. This explains the gradual decrease in the slopes at the lower temperature region (below 200 °C). At the higher temperature region (above 200 °C), the resistance cannot be assumed to be constant anymore but increases as the temperature increases (see equation (2.2)), which makes the curve almost linear.

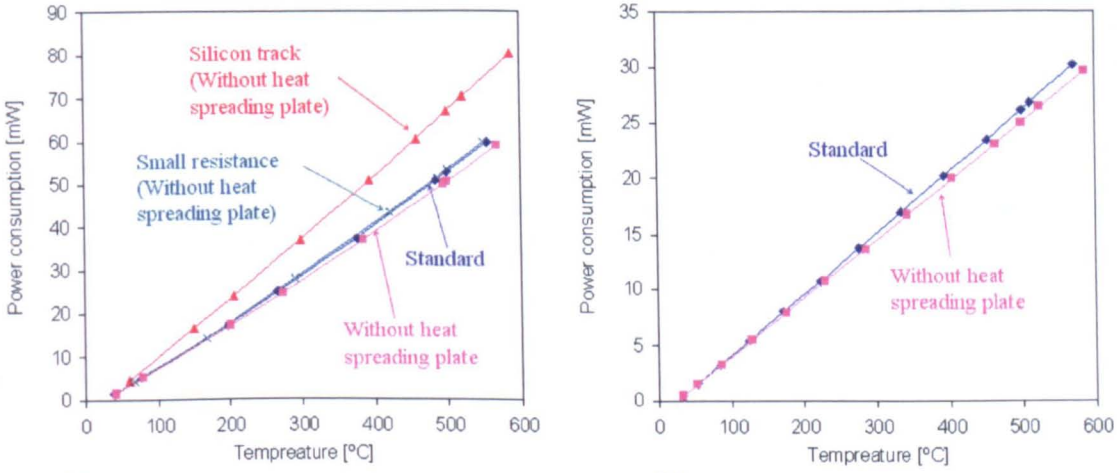

Figure 2.14. Simulated power consumption of (a) large micro-hotplates and small micro-hotplates.

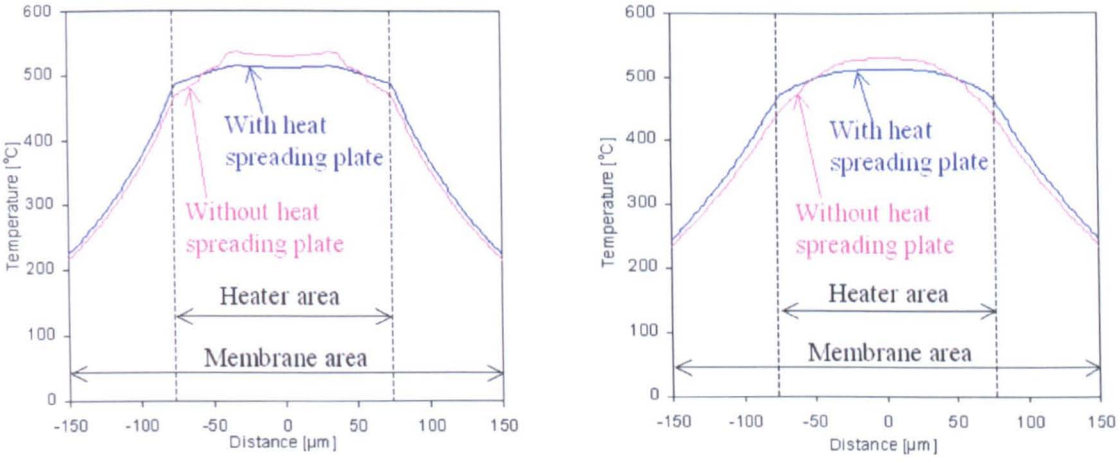

Figure 2.15. Simulated temperature profiles with and without metal heat spreading plate for large micro-hotplates along (a) *x* axis and (b) *y* axis.

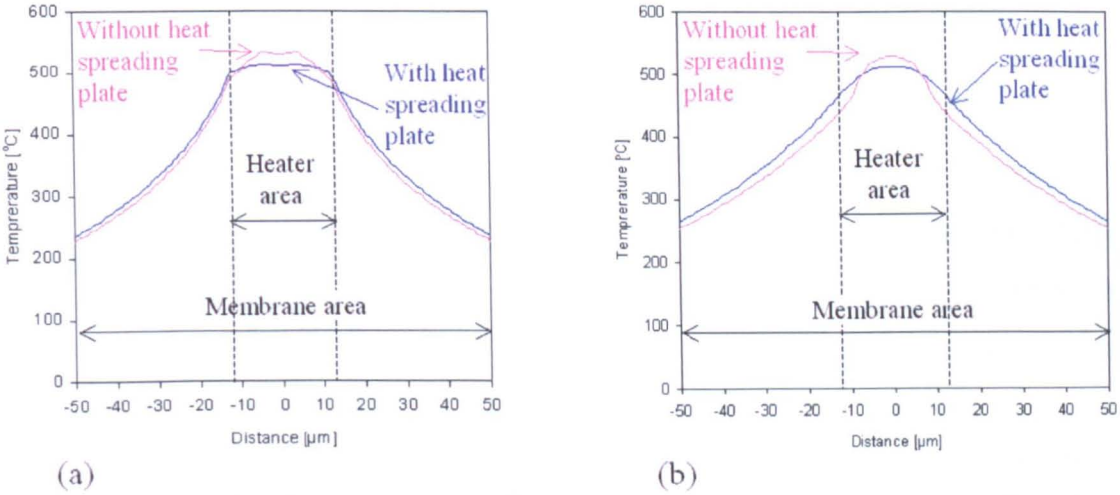

Figure 2.16. Simulated temperature profiles with and without metal heat spreading plate for small micro-hotplates along (a) *x* axis and (b) *y* axis.

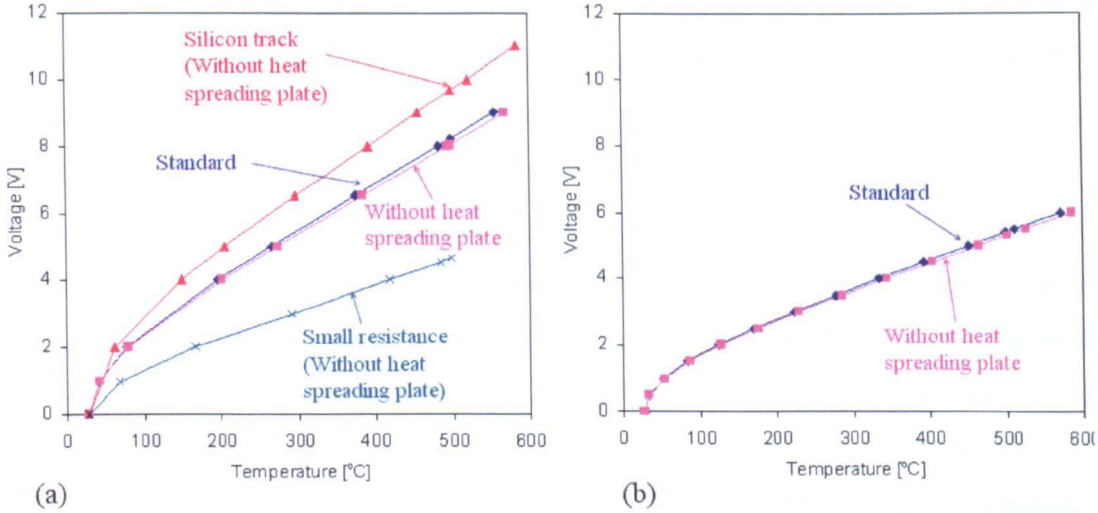

Figure 2.17. Simulated operating voltage vs temperature of (a) large micro-hotplates ("standard", "without heat spreading plate", "small resistance" and "silicon track") and (b) small micro-hotplates ("standard" and "without heat spreading plate").

2.4 Conclusions

Here novel micro-hotplates for gas sensors employing single crystal silicon as resistive heaters have been proposed. The designs are fully compatible with an SOI-CMOS process and hence can be integrated with drive and detection circuitry. They are expected to be thermally stable without chemically reactive grain boundaries, and as SOI substrate has been used the area under the heater is passivated with SiO_2.

In addition, the designs were optimised to achieve ultra-low power consumption in the following way:

1. Low resistance metal (W or Al) tracks were employed to reduce the Joule heat wasted in the tracks.
2. Resistive heaters were designed to be much smaller than previously reported devices in order to suppress the most significant convective heat loss (heated area: 0.00045 mm^2).
3. Membrane to heater ratio was designed to be much larger than previously reported devices in order to reduce the conductive heat loss (membrane to heater ratio: 12.5).

FEM simulations were performed to confirm the design concept prior to fabrication. It was found that the proposed micro-hotplates can be operated at 500 °C with ultra-low power consumption of 26 mW and low battery voltage of less than 5 V. Furthermore, it was found that a novel heat spreading plate design makes the temperature deviation to be reduced by more than 50 %.

It should be noted that there is a limitation in the 2D electro-thermal simulation. In the 2D simulation, the heat loss to the air was not simulated by a fluid dynamics simulator but was simply assumed to be the same as [2.6], though it can depend on the geometry of the micro-hotplates (Not all the heat transferred from the heater to the air simply dissipates, but part of it can be conducted to other parts of the chip (*e.g.* substrate) or the package on which the chip is mounted). Therefore, it is needed to investigate the discrepancy between simulated and experimental results.

The characterisation of the fabricated devices is described in the next chapter.

References

[2.1] J.W. Gardner, V.K. Varadan and O.O. Awadelkarim, "Microsensors, MEMS, and Smart Devices", Chichester: Wiley, 2001.

[2.2] INSPEC (Information service), "Properties of Silicon", EMIS data reviews series, no. 4. London: INSPEC, Institution of Electrical Engineers, 1988, pp. 411-475.

[2.3] M. Rydberg and U. Smith, "Long-term-stability and electrical properties of compensation doped poly-Si IC-resistors", IEEE Transactions on Electron Devices, Vol. 47, No.2, 2000, pp. 417-426.

[2.4] Z. Tang, S.K.H. Fung, D.T.W. Wong, P.C.H. Chan, J.K.O. Sin and P.W. Cheung, "An integrated gas sensor based on tin oxide thin-film and improved micro-hotplate", Sensors and Actuators B 46, 1998, pp.174-179.

[2.5] X-FAB Semiconductor Foundries, "Process Specification XI10 – 1.0 μm process", June 2001.

[2.6] A. Pike and J.W. Gardner, "Thermal modelling and characterisation of micropower chemoresistive silicon sensors", Sensors and Actuators B 45, 1997, pp.19-26.

CHAPTER 3

Fabrication and characterisation of SOI-CMOS micro-hotplates

3.1 Introduction

In chapter 2, a new generation of micro-hotplates for gas sensors was proposed based upon SOI-CMOS technology. These micro-hotplates were strategically designed to have ultra-low power consumption, high reliability and, importantly, low cost in volume production.

In this chapter, we describe the SOI-CMOS fabrication process used to fabricate the devices, as this is a standard microelectronics process it allows all of the associated circuitry to be integrated with the micro-hotplates. This chapter also describes the characterisation of the fabricated devices. Firstly, electro-thermal properties are characterised in detail, and the results compared with the simulations in chapter 2. Secondly, long term stability tests were carried out and the results were compared to traditional polysilicon heaters. Since it is impossible to predict device reliability by simulation, these tests are crucial. It is believed that this is the first time that long term stability of single crystal silicon heater have been characterised.

3.2 Fabrication of the novel SOI-CMOS micro-hotplates

The fabrication was performed by three companies: XFAB (Germany) for SOI-CMOS processing, Silex Microsystems (Sweden) for DRIE (Deep Reactive Ion Etching) back etching, and Pac Tech GmbH (Germany) for Au/Ni electroless plating (described later).

Figure 3.1 gives the fabrication process focussing on the key process steps. The figure shows not only micro-hotplates but also associated circuitry. It should be noted that this circuitry was not made here, but is included to show possible integration. Circuitry was integrated in a separate project with the University of Cambridge. The process is detailed as follows:

(a) The fabrication process starts at XFAB using its XI10 1.0 μm SOI-CMOS process. The process has a choice of two materials for metallization: tungsten and aluminium, both of which were used in this project (Metal layers are labelled as Al only in figure 3.1 for simplicity). The initial substrate is a 6 inch SOI wafer with n-type active layer. The film thicknesses of all the films are listed in table 3.1 [3.1].

(b) Trench etching of active silicon layer is performed. This is originally a process to isolate each MOSFET, and is also used to define the shape of resistive heater structure. It may be possible to define heater structures without trench etching since the diffusion distance of the dopant from the $n+$ or $p+$ regions is limited as described in [3.2]. However, it was believed that this process would help to fabricate heater structure more precisely and to reduce power consumption by removing an unnecessary part of the highly conducting silicon layer.

(c) Ion implantation of BF_2 (boron difluoride) is used for the p-well to create NMOS structures.

(d) Ion implantation for the resistive heater is performed. This is originally a process to dope source and drain ($n+$ or $p+$), which have the highest dopant concentrations in SOI-CMOS, and is used to dope resistive heater structures simultaneously.

(e) The rest of the SOI-CMOS process is performed. Note that no additional process steps are required for the commercial SOI-CMOS process to form the resistive heater structure. Therefore no additional costs to an SOI-CMOS factory are required when commercialising the proposed devices.

(f) The wafers were sent to Silex Microsystems where DRIE was performed from the backside of the SOI wafer to etch the silicon substrate. In this process the buried oxide layer of the SOI wafers acts to stop the etching. This process can etch silicon nearly vertically (aspect ratios of 30 or larger) and thus the smaller chip size can be achieved compared with traditional anisotropic wet etching using for example KOH or TMAH.

(g) The wafers were sent to PacTech, and Au/Ni electroless plating, which is originally a process to form bumps onto aluminium electrodes for flip chip bonding, was performed. This process was carried out for the aluminium metallization wafers to make sure that there is an ohmic contact between electrodes and sensing materials. The thicknesses of the Au and Ni films are 0.2 μm and 2.0 μm, respectively.

(h) Finally, deposition of sensing materials was performed. This process is detailed in chapter 5.

Fabrication was performed successfully (with few membranes broken mainly in dicing and Au/Ni electroless plating processes) and figure 3.2 shows all the 5 fabricated chips designed in the previous chapter. Each chip has 5 large membranes (radius: 282 μm) and 4 small membranes (radius: 150 μm). Figure 3.3 shows photographs of the large and small resistive micro-hotplates (SRL289A and SRL289e).

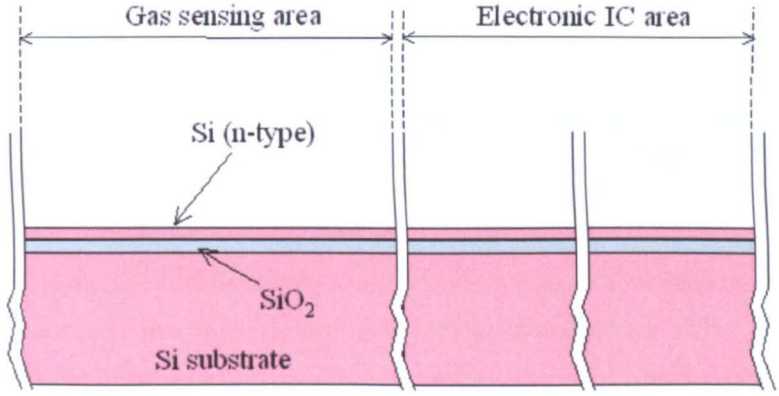

(a) Initial substrate: 6 inch SOI wafer with n-type active layer

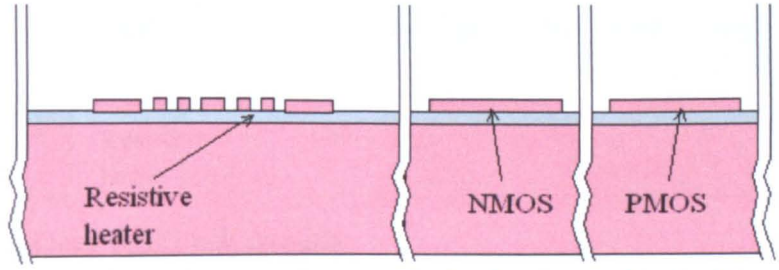

(b) Trench etching to pattern resistive heater and to isolate MOSFET

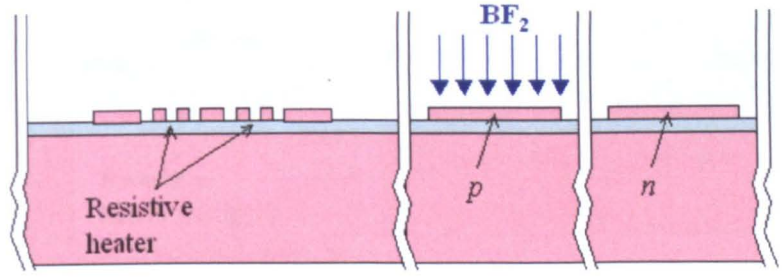

(c) Ion implantation for p-well

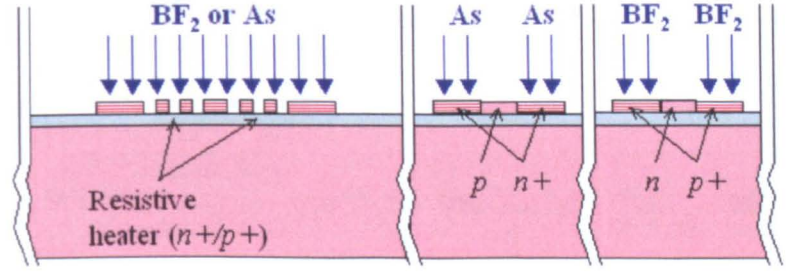

(d) Ion implantation for resistive heater, source and drain

Figure 3.1. Fabrication process for SOI-CMOS micro-hotplate.

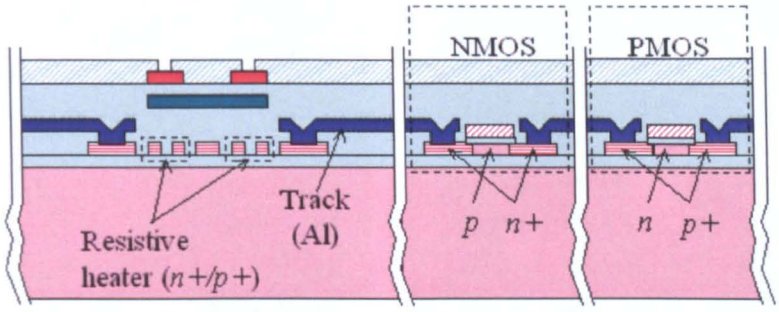

(e) Rest of the SOI-CMOS process (metallization: Al)

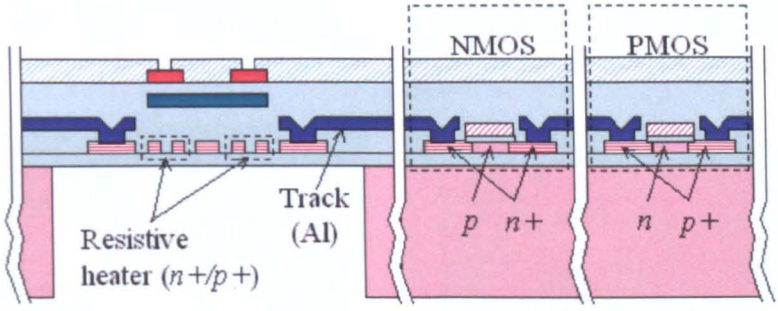

(f) Deep RIE back etching

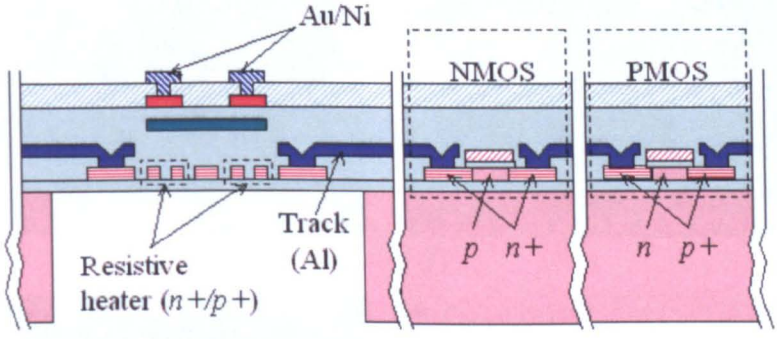

(g) Au/Ni electroless plating

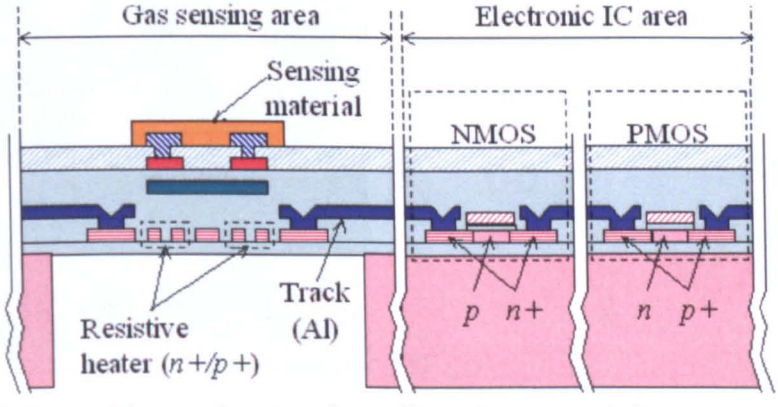

(h) Deposition and patterning of sensing material

Figure 3.1. (*Continued*)

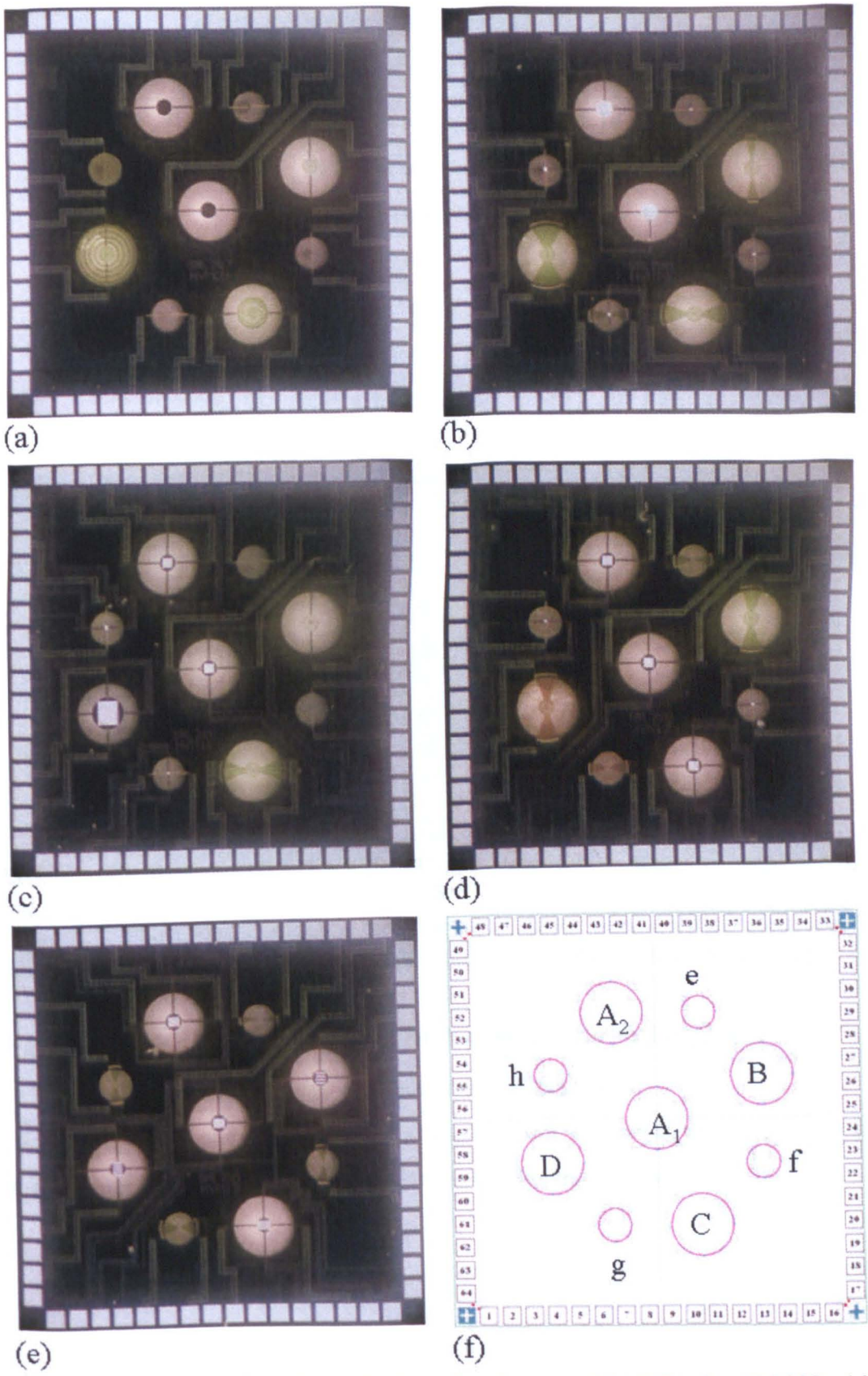

Figure 3.2. Photographs of the fabricated chips. (a) SRL287, (b) SRL288, (c) SRL289, (d) SRL290, (e) SRL291, (f) labelling for each micro-hotplate.

Table 3.1. Thickness of process layers.

	Tungsten device	Aluminium device
Active silicon	250 ± 10 nm	250 ± 10 nm
Polysilicon	300 ± 30 nm	300 ± 30 nm
Met1	300 ± 50 nm	720 ± 120 nm
Met2	300 ± 50 nm	650 ± 120 nm
Met3	500 ± 100 nm	940 ± 140 nm
Silicon nitride	550 ± 100 nm	550 ± 100 nm
Silicon oxide	3800 ± 250 nm	3550 ± 200 nm

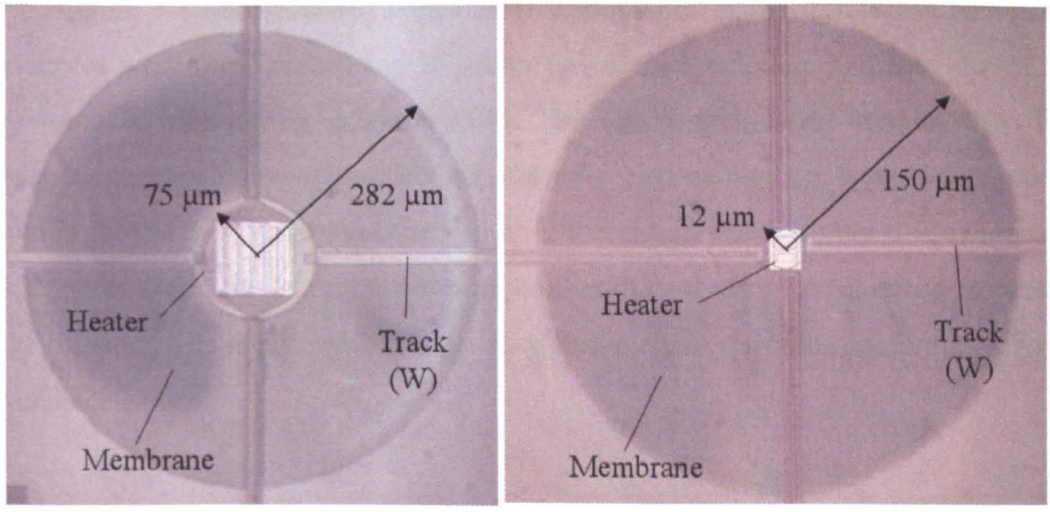

(a) (b)

Figure 3.3. Photographs of (a) a large micro-hotplate with resistive electrodes (SRL289A), and (b) a small micro-hotplate with resistive electrodes (SRL289e).

3.3 Characterisation of the novel SOI-CMOS micro-hotplates

3.3.1 Calibration of temperature coefficient of resistances

As mentioned earlier, the resistive heaters are also used to monitor the temperature of the micro-hotplates. This is achieved by using the following equations:

$$\rho(T) = \rho_a \left[1 + \alpha_1 (T - T_a) + \alpha_2 (T - T_a)^2\right] \tag{3.1}$$

where $\rho(T)$ is the electrical conductivity, T is the temperature, T_a is the ambient temperature (27 °C), ρ_a is the resistivity at the ambient temperature, α_1, α_2 are the temperature coefficients of resistance (TCRs). Those TCRs depend on the type of

dopant, its concentration and the size of grains (in the case of polysilicon). Before the heaters can be used as temperature sensors these parameters require measurement.

The devices SRL287A, SRL290A and SRL290C were chosen to obtain values for the TCRs for $n+$, $p+$ and polysilicon. The devices were bonded to ceramic packages using gold wires and put into a temperature controlled electric furnace (Carbolite AAF1100). Cu wires insulated by glass capillary tubes (SAMCO) were used for electrical connection between the ceramic package inside the furnace and the multimeter (FLUKE 8840A) outside. The temperature dependence of resistances was measured using a 4 probe resistance measurement technique neglecting all the unnecessary resistances (e.g. resistances of Ni wires, gold wires and tungsten tracks).

Figure 3.4 illustrates the temperature dependence of the resistances measured. The curves were fitted well using 2nd order polynomial function, and thus the TCRs were found as defined by equation (3.1). The results are shown in table 3.2. The resistances at room temperature before and after this calibration were compared as shown in table 3.3. It was found that the typical resistance drift during this calibration was less than 0.5 %, indicating that the calibration did not affect the material properties of the resistors. The measured TCRs are used in the characterisation performed later in this chapter.

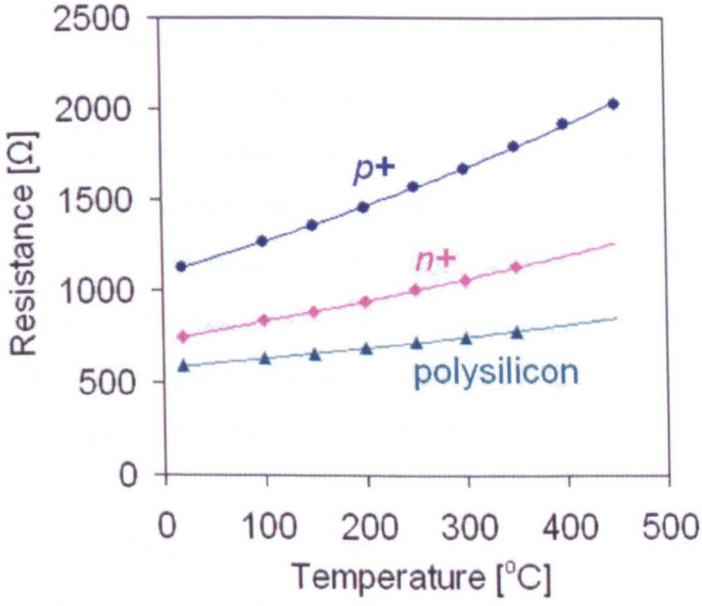

Figure 3.4. Temperature dependence of the resistances of the fabricated SOI micro-hotplates.

Table 3.2. Experimental values of TCRs of *n*+, *p*+ and polysilicon and correlation coefficient for quality of fit to model.

	n+	*p*+	polysilicon
α_1 [1/K]	1.37×10^{-3}	1.47×10^{-3}	0.88×10^{-3}
α_2 [1/K^2]	4.9×10^{-7}	8.9×10^{-7}	4.4×10^{-7}
r^2	0.9993	0.9997	0.9998

Table 3.3. Resistances of resistive heaters before and after calibration.

	n+	*p*+	polysilicon
R_b (Ω)	746.0	1130	588
R_a (Ω)	747.5	1130	586
$(R_b-R_a)/R_b$ (%)	0.20 %	0.00 %	-0.34 %

3.3.2 Electro-thermal characterisation of the standard devices

I-V measurements of the devices were performed using a probe station (Karl Suss, PM5) and semiconductor parameter analyzer (Agilent 4156C). The standard devices (SRL287A and SRL287e) from 5 chips in different places in a wafer with tungsten metallization were measured. The location of those chips is top (8-3), centre (5-4), bottom (1-2), left (5-1) and right (5-7) as shown in figure 3.5.

Figure 3.6 shows the *I-V* characteristics of those micro-hotplates and table 3.4 shows the resistance values at room temperatures. *I-V* curves of micro-hotplates from 5 different places are almost identical for both large and small micro-hotplates. In fact, the standard deviations of the resistances of large and small standard devices at room temperature were only 0.31 % and 1.49 %, respectively. It is believed that this excellent uniformity was achieved by the precise structure forming from using a trench etching process.

Figure 3.7 shows the power consumption and operating voltage, as a function of temperature, for the large and small standard micro-hotplates. The standard large and small micro-hotplates require only 26.6 mW (5.95 V) and 9.4 mW (3.35 V) to operate at 500 °C. To our knowledge, the value for the standard small micro-hotplate is the

smallest reported in the literature. They are smaller than the values simulated in the previous chapter (53 mW for large micro-hotplate and 26 mW for the small micro-hotplate), and this discrepancy is discussed later in this chapter.

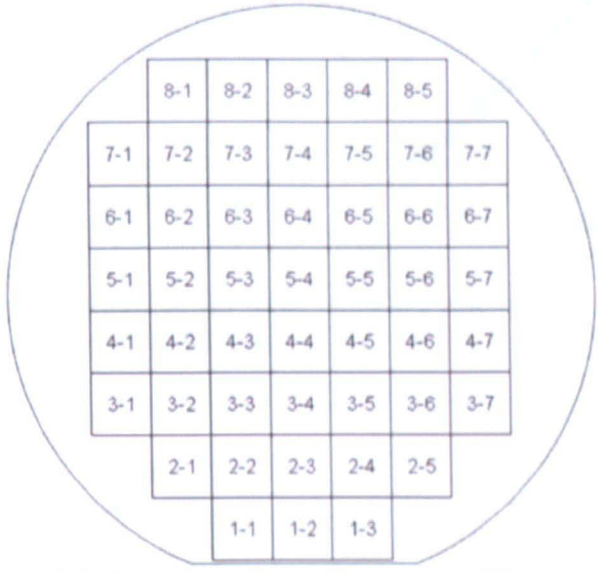

Figure 3.5. Location of the chips on the silicon wafer.

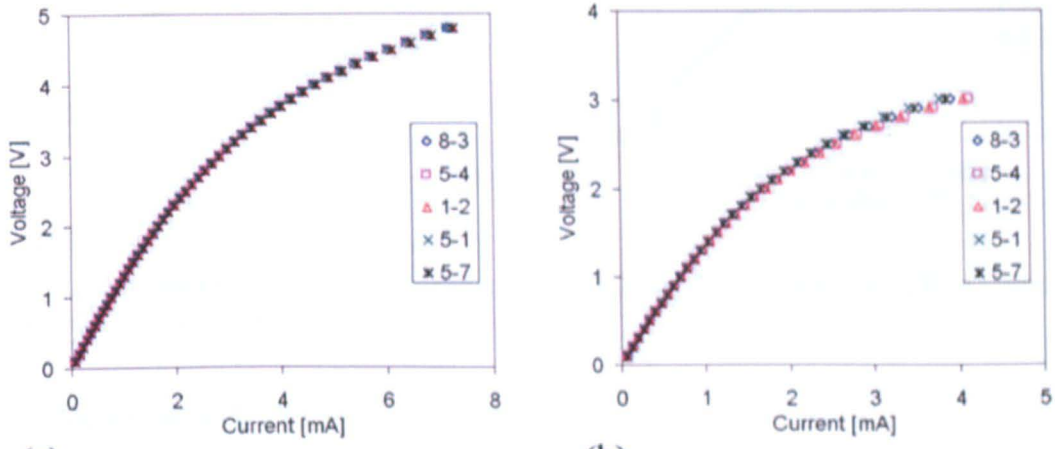

Figure 3.6. Measured *I-V* curves of (a) large standard micro-hotplate (SRL287A), and (b) small standard micro-hotplate (SRL287e).

Table 3.4. Resistances of standard micro-hotplates measured at room temperature.

	8-3	5-4	1-2	5-1	5-7	average	σ [%]
Large, standard (SRL287A)	749.2	752.6	753.0	748.0	748.8	750.3	0.31%
Small, standard (SRL287e)	673.8	678.4	678.2	660.0	658.0	669.7	1.49%

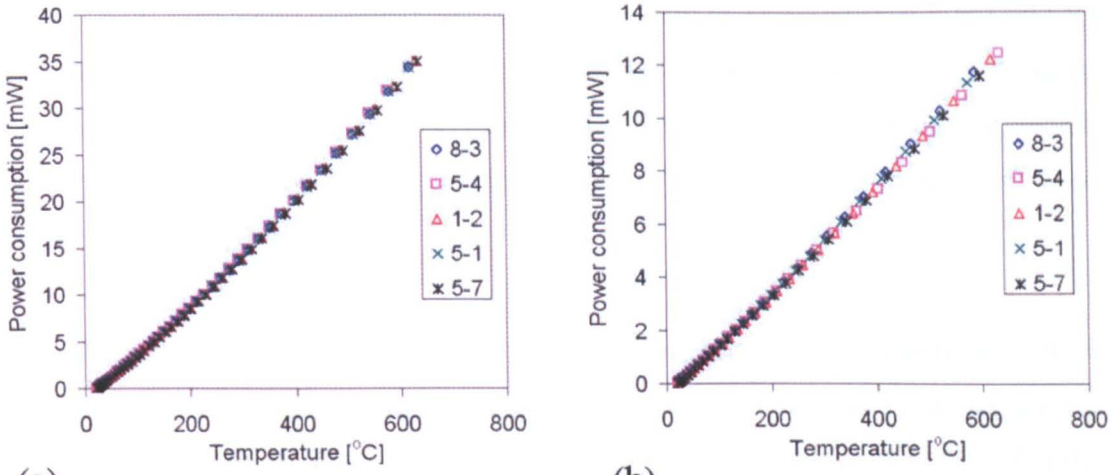

Figure 3.7. Power consumption of (a) large standard micro-hotplate (SRL287A), and (b) small standard micro-hotplate (SRL287e).

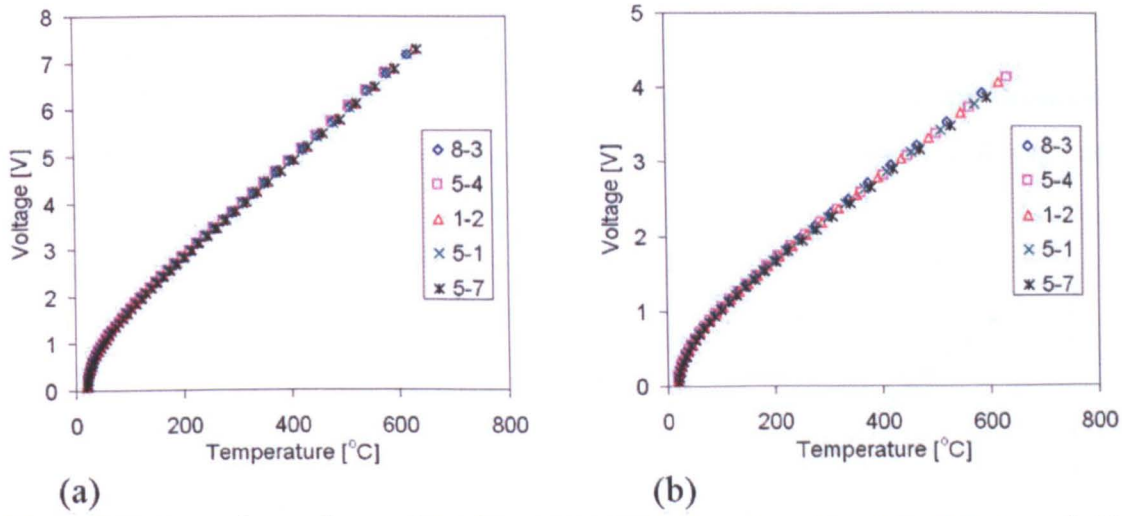

Figure 3.8. Operating voltage of (a) large standard micro-hotplate (SRL287A), and (b) small standard micro-hotplate (SRL287e).

3.3.3 Electro-thermal characterisation of other devices

A number of different types of devices were characterised and discussed in terms of (a) metallization, (b) resistive electrodes, (c) heater radius, (d) heater resistance, (e) resistive track, (f) heater material and (g) metal heat spreading plate. The results of these measurements are described below.

(a) Metallization

Figure 3.9 shows the power consumption and the operating voltages of the large and small standard micro-hotplates with aluminium metallization as compared to those with tungsten metallization (as described earlier). The large and small standard micro-

hotplates with aluminium metallization require 16.6 mW (4.18 V) and 6.6 mW (2.47 V) to operate at 300 °C, respectively. All of the above values are greater than those of tungsten metallization devices by approximately 17 % and 27 % respectively, which required 14.2 mW (3.89 V) and 5.2 mW (2.24 V). The possible reasons of these differences are as follows:

1. The thickness of the aluminium layer is roughly twice as much as that of tungsten layer and the thermal conductivity of aluminium is 1.3 times greater than tungsten – hence 2.6 times the thermal loss (aluminium: 236 W/mK, tungsten: 177 W/mK) [3.3]
2. The thickness of silicon dioxide layer for aluminium metallization devices is 10 % greater than that of tungsten.

All of the following characterisations were performed using tungsten metallization devices with the above fact in mind (*i.e.* values for aluminium devices can always be estimated easily).

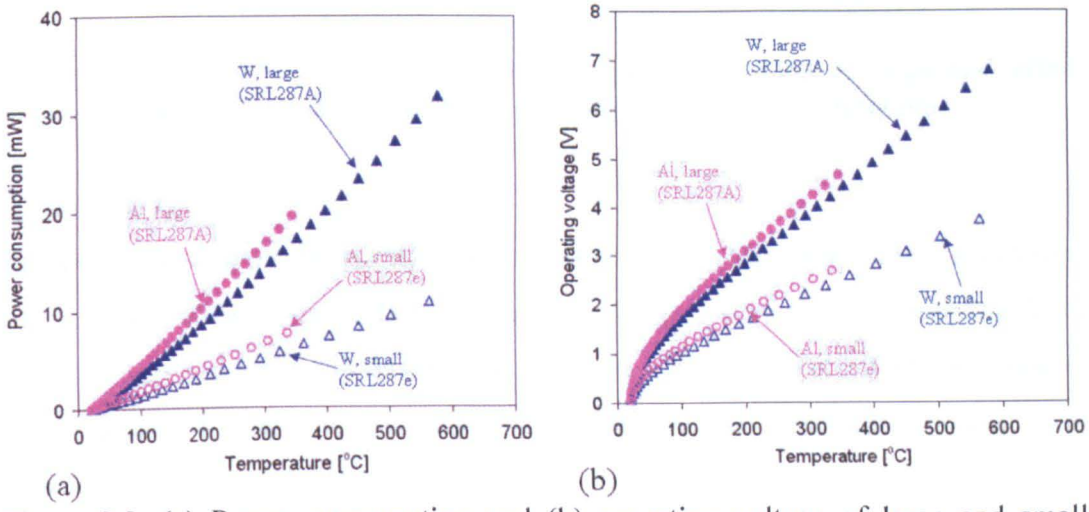

Figure 3.9. (a) Power consumption and (b) operating voltage of large and small micro-hotplates with aluminium metallization as compared to those with tungsten metallization.

(b) Resistive electrodes

The effect of resistive electrodes upon power consumption and operating voltage was examined. It is expected that the resistive electrodes and their tracks would increase thermal conduction along the membranes and thus increase both power consumption and operating voltage.

Figure 3.10 show power consumptions of large and small micro-hotplates with resistive electrodes (SRL289A and SRL289e) compared with the standard devices (without resistive electrodes, SRL287A and SRL287e). The large and small micro-hotplates with resistive electrodes consume 29.3 mW (6.24 V) and 11.6 mW (3.71 V) to operate at 500 °C, respectively. They are 10 % and 23 % greater than those without electrodes. These types of resistive devices are used in the latter part (chapters 4-6) of this thesis.

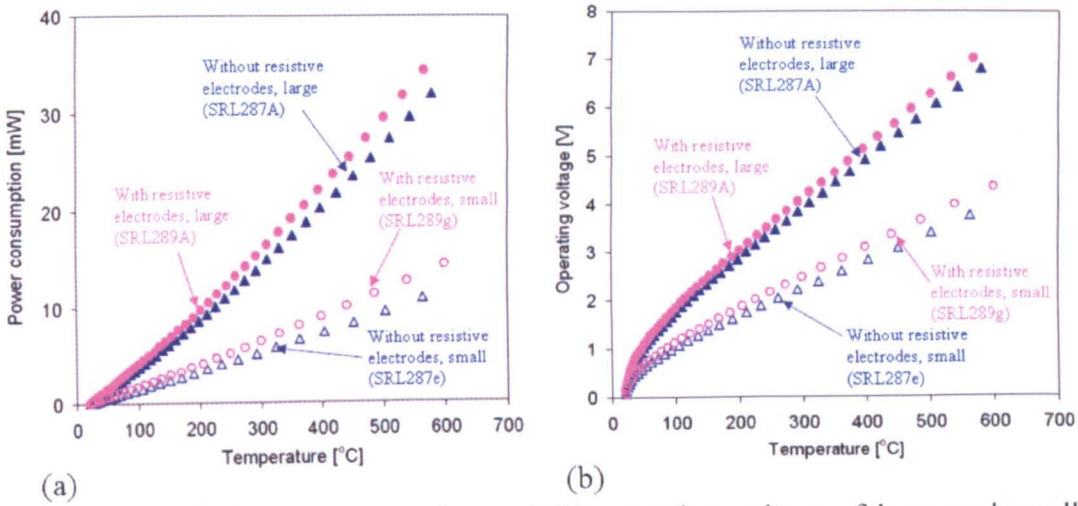

Figure 3.10. (a) Power consumption and (b) operating voltage of large and small micro-hotplates with resistive electrodes as compared to those without ones.

(c) Heater radius

The devices with larger heater radii than the standard devices were also characterised. They are SRL289D (heater radius: 150 μm) for large micro-hotplates (standard heater radius: 75 μm) and SRL289h (heater radius: 18 μm) for small micro-hotplates (standard heater radius: 12 μm). Their power consumption and operating voltage were characterised as shown in figure 3.11.

They have higher power consumption and higher operating voltage than devices with standard radii, though they have advantages: deposition of sensing materials will be easier and higher aspect ratio resistive electrodes can be used (*i.e.* sensing materials with a higher resistivity are allowed).

These results also confirm the design concepts aiming for ultra-low power consumption. They were (1) to reduce the convective heat loss by minimising the size of the heater, and then (2) to reduce the conductive heat loss by minimising the

membrane to heater ratio. If the devices worked according to these concepts, power consumptions should follow this relationship [3.4]:

$$P \propto 1/ln(r_m/r_h) \tag{3.2}$$

where r_m and r_h denote the radii of membrane and heater, indicating that the main heat dissipation mechanism is conduction through the membrane. Figure 3.12 plots the power consumption to operate at 500 °C vs $1/ln(r_m/r_h)$. The results are almost linear *i.e.* satisfy equation (3.2), and thus justify our design concepts.

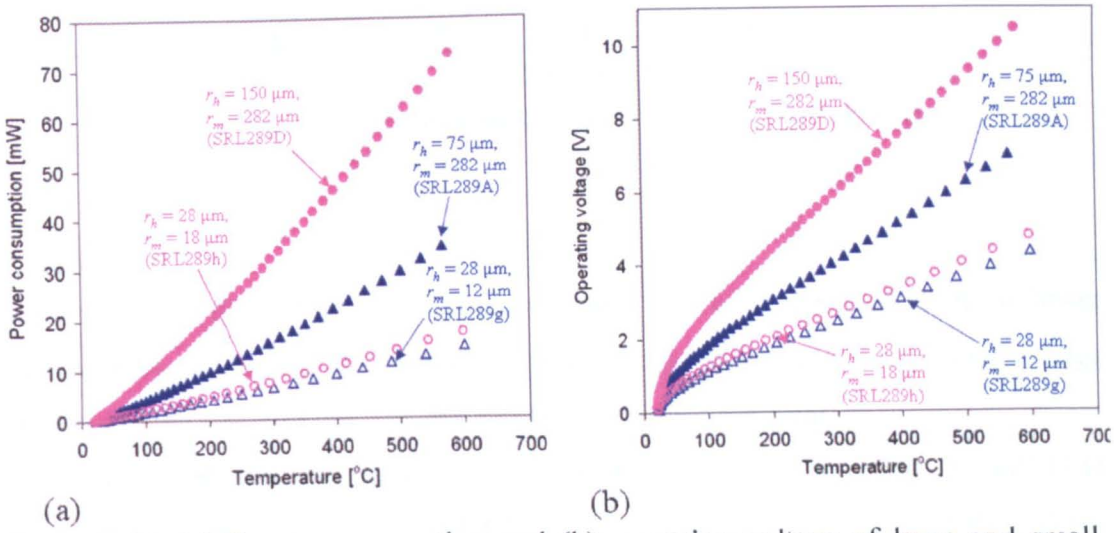

(a) (b)

Figure 3.11. (a) Power consumption and (b) operating voltage of large and small micro-hotplates of various heater and membrane radii.

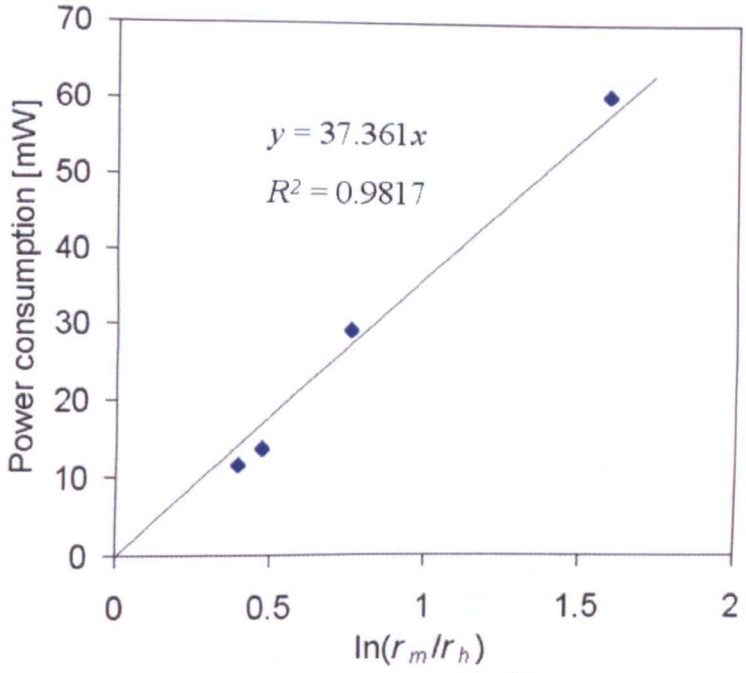

Figure 3.12. Power consumption at 500 °C vs logarithm of membrane to heater ratio.

(d) Heater resistance

SRL289B and SRL287f are the micro-hotplates that were designed to have lower resistances by connecting 10 resistors in parallel; thus have a lower operating voltage compared to the standard devices, but still be thermally equivalent.

In fact, measured resistances of SRL289B and SRL287f were 208 Ω and 133 Ω compared with standard 750 Ω and 670 Ω. The operating voltage V of the micro-hotplates can be related to the heater resistance R by the following equation:

$$V = \sqrt{PR} \tag{3.3}$$

where P is the power consumption. Assuming that P is a constant (*i.e.* the lower resistance device is thermally equivalent to the standard devices), it is predicted from equation (3.3) that the operating voltages of the lower resistance devices will be 52.7 % and 44.6 % of the standard devices.

Figure 3.13 shows the power consumptions and operating voltages of those lower resistance devices compared with the standard devices. It was shown that the resistance has little effect on power consumptions as expected. In addition, it was found that the operating voltage of lower resistance devices was much smaller than those of

the standard devices. They are 53.4 % and 44.8 %, and thus our prediction was shown to be correct. Those lower resistance devices will be more suitable for battery operation (*i.e.* < 5 V operating voltage).

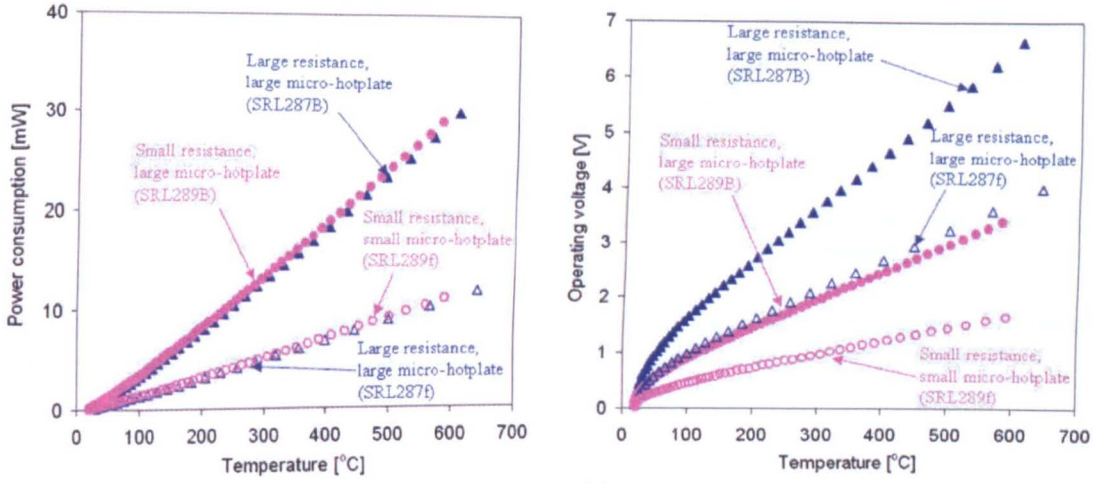

(a) (b)

Figure 3.13. (a) Power consumption and (b) operating voltage of large and small micro-hotplates with smaller resistances as compared to those with standard ones.

(e) Resistive track

The micro-hotplates with single crystal silicon tracks were also fabricated as described earlier. The advantage of these devices is that they can be used as a base for high temperature (*e.g.* 500 °C) calorimeters even with the aluminium metallization, which is more compatible with most SOI-CMOS factories.

Figure 3.14 shows the power consumption and operating voltage of those devices. The large and small micro-hotplates with silicon track devices require 30.1 mW (6.91 V) and 12.5 mW (4.64 V). Those values are greater than tungsten track devices, though still acceptable for hand held gas monitors.

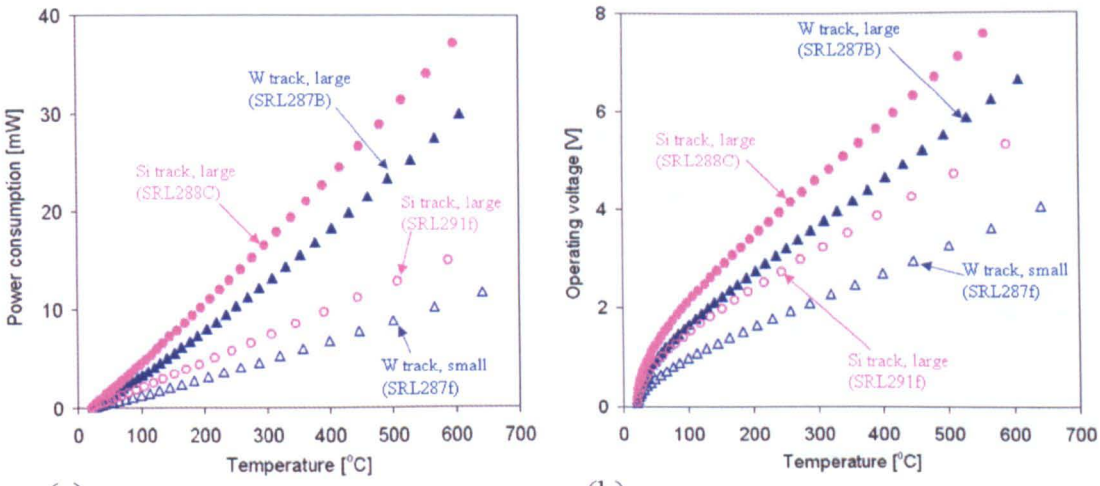

(a) (b)

Figure 3.14. (a) Power consumption and (b) operating voltage of large and small micro-hotplates with silicon tracks as compared to those with tungsten tracks.

(f) Heater material

The resistive heaters of the micro-hotplates characterised so far were made of *n*+ doped single crystal silicon. Here micro-hotplates with resistive heaters made of the other dopant *i.e.* *p*+ (SRL290A and SRL290f) and n-type polysilicon (SRL290C and SRL290h) were characterised for comparison. The geometric shapes of these devices were designed to be exactly the same as that made of *n*+ (SRL289A and SRL289g).

Figure 3.14 shows the power consumption and operating voltage of *p*+ and polysilicon micro-hotplates, compared with those of *n*+. The power consumptions of *p*+ and polysilicon micro-hotplates have only little deviations from those of *n*+ as expected. These results indirectly justify the TCRs, which is used to measure the temperatures, characterised earlier in this chapter. The operating voltages at 300 °C of the *p*+ and polysilicon devices are larger (127 %) and smaller (85 %) than those of the *n*+ devices. They are close to the predicted values of 127 % and 87 % from the sheet resistances of those layers (*p*+: 65 Ω, *n*+: 40 Ω, polysilicon: 30 Ω) using equation (3.3).

The standard deviations of resistances of *p*+ and polysilicon in a wafer were also measured as shown in table 3.5. They have excellent uniformity, as *n*+, with standard deviations of less than 2 %.

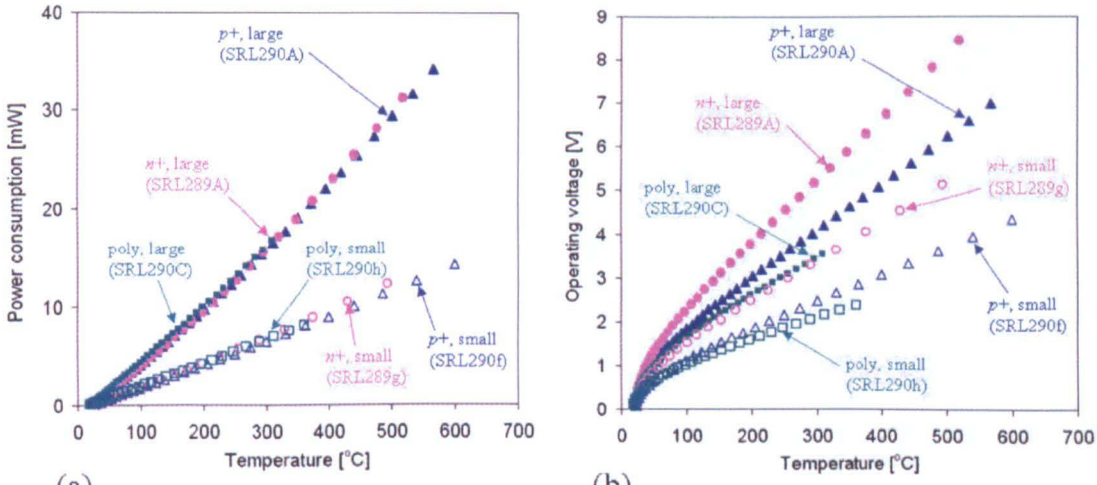

Figure 3.15. (a) Power consumption and (b) operating voltage of large and small micro-hotplates with resistive heaters made of $p+$ or n-type polysilicon as compared to those with $n+$.

Table 3.5. Resistances of micro-heaters made of $p+$ and polysilicon at room temperature.

	1-2	3-6	5-4	5-6	6-6	average	σ [%]
Large, $p+$ (SRL290A)	1191.6	1164.6	1177.0	1162.6	1158.2	1170.8	1.16%
Small, $p+$ (SRL290f)	1158.8	1130.4	1164.0	1130.4	1125.2	1141.8	1.59%
Large, poly (SRL290C)	592.8	581.8	592.8	582.8	578.8	585.8	1.12%
Small, poly (SRL290h)	545.2	540.4	546.4	532.2	531.0	539.0	1.33%

(g) Metal heat spreading plate

The heat spreading plate was introduced to improve the temperature uniformity. Here the effect of the heat spreading plate upon power consumption and operating voltage is examined.

Figure 3.16 shows the power consumption and the operating voltage of large and small micro-hotplates without the heat spreading plate (SRL287B and SRL287f) compared with the standard devices (without resistive electrodes, SRL287A and SRL287e). The large and small micro-hotplates with heat spreading plate consume 26.6 mW and 9.4 mW, whereas those without consume 23.5 mW and 8.7 mW, respectively. The increase in power consumption by employing the metal heat spreading plate is only 13 % and 8 %, and thus is not very significant.

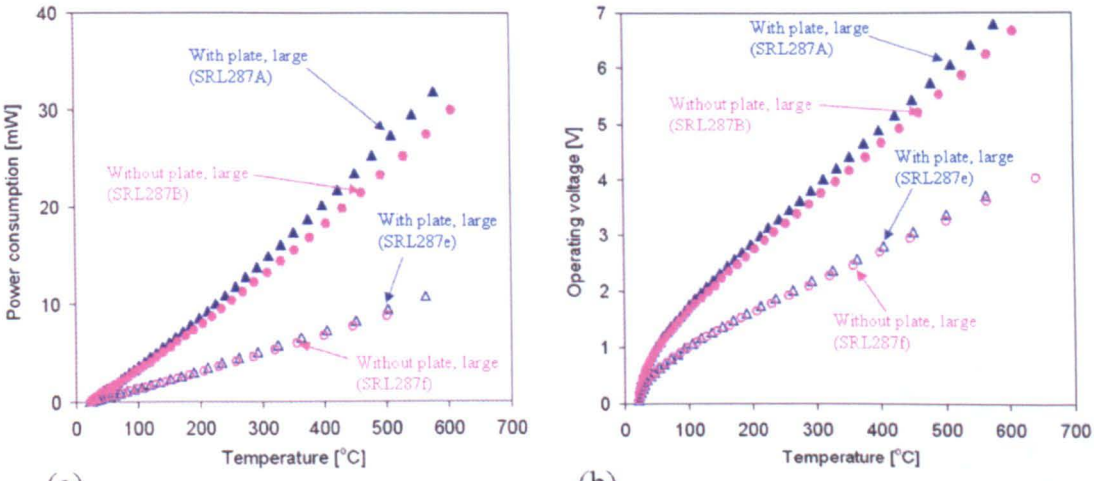

(a) (b)

Figure 3.16. (a) Power consumption and (b) operating voltage of large and small micro-hotplates without metal heat spreading plate as compared to those with ones.

Finally, all the micro-hotplates characterised in this chapter are summarised in table 3.6 with the power consumption and the operating voltage at 500 °C.

Table 3.6. All the micro-hotplates characterised in this chapter with power consumptions and voltages to operate at 500 °C.

Name	Metal	Membrane radius [μm]	Heater radius [μm]	Heater material	Heater shape	Track	Heat spreading plate	Aspect ratio	Power at 500 °C (300 °C) [mW]	Voltage at 500 °C (300 °C) [V]
SRL287A	W	282	75	*n*+	n	metal	yes	-	26.6 (14.2)	5.95 (3.89)
SRL287A	Al	282	75	*n*+	n	metal	yes	-	(16.6)	(4.18)
SRL287B	W	282	75	*n*+	n	metal	no	-	23.5	5.58
SRL288C	W	282	75	*n*+	n	*n*+	no	-	30.1	6.91
SRL289A	W	282	75	*n*+	n	metal	yes	40	29.3 (15.7)	6.24 (4.09)
SRL289B	W	282	75	*n*+	l	metal	no	-	24.1	2.98
SRL289D	W	282	150	*n*+	n	metal	yes	234	60.6	9.11
SRL290A	W	282	75	*p*+	n	metal	yes	40	29.8 (15.7)	8.15 (5.20)
SRL290C	W	282	75	poly	n	metal	yes	40	(16.0)	(3.46)
SRL287e	W	150	12	*n*+	n	metal	yes	-	9.4 (5.2)	3.35 (2.24)
SRL287e	Al	150	12	*n*+	n	metal	yes	-	(6.6)	(2.47)
SRL287f	W	150	12	*n*+	n	metal	no	-	8.7	3.24
SRL289f	W	150	12	*n*+	l	metal	no	-	9.0	1.45
SRL289g	W	150	12	*n*+	n	metal	yes	1.7	11.6 (6.4)	3.71 (2.47)
SRL289h	W	150	18	*n*+	n	metal	yes	5.3	13.8	4.06
SRL290f	W	150	12	*p*+	n	metal	yes	1.7	12.5 (6.9)	5.18 (3.38)
SRL290h	W	150	12	poly	n	metal	yes	1.7	(6.5)	(2.08)
SRL291f	W	150	12	*n*+	n	*n*+	no	-	12.5	4.64

3.3.4 Comparison with simulations

As stated earlier, there was an initial discrepancy between the simulated results and the experimental results: the simulated power consumptions were about twice that of the experimental ones. It was found by Cambridge University that the thermal conductivity of the silicon nitride film used was only 2.2 W/mK, which is much smaller than 20 W/mK, used in the initial simulations [3.5]. This new value is a typical value for a silicon nitride film deposited by PE-CVD, whereas the previous value is the one deposited by LP-CVD.

Figure 3.17 shows a comparison between the measured and simulated power consumptions using this new value, which shows much closer agreement. For example, the simulated power consumption for 500 °C operation is 31.0 mW, which is only 17 % larger than the measured value. Therefore, it is possible to predict the characteristics of micro-hotplates using simple 2D FEM simulation.

The simulated curve in figure 3.17 is more nonlinear than the experimental one, indicating that the simulation exaggerates the effect of convection. This is probably due to the assumption for the heat loss to the air in the 2D simulation (*i.e.* Heat loss to the air is assumed to be the same as [2.6]). It may be concluded that the more heat, which is first transferred to the air, is then conducted to other parts of the chip or the package in the proposed device than the one tested in [2.6].

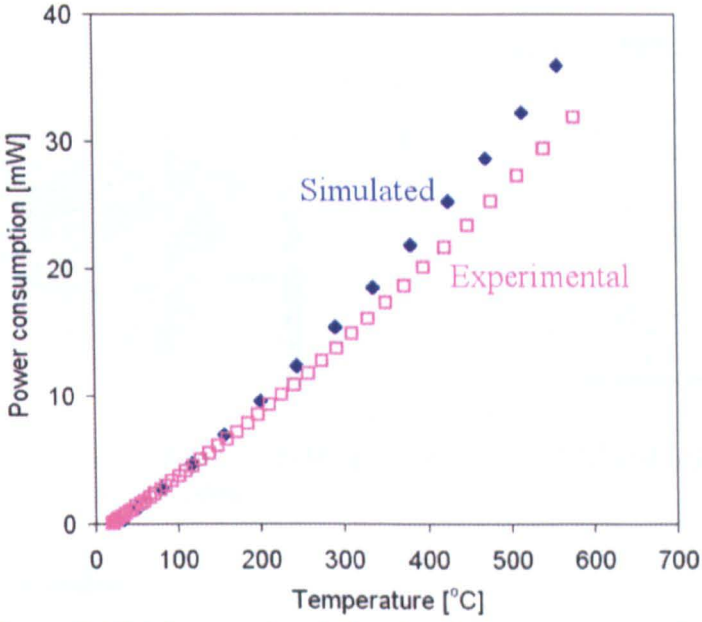

Figure 3.17. Measured and simulated power consumption of standard large micro-hotplate (SRL287A).

3.3.5 Membrane deformation

Membrane deformation of a micro-hotplate (SRL290A) was characterised using an optical interferometer (Wyko/NT2000) at room temperature, 350 °C and 500 °C. The results are shown in figure 3.18. It was found that the membrane deformed at room temperature and the deformation increased as the temperature was elevated. The cause of this is the difference of internal stress (and its temperature dependence due to the temperature expansivity) of each film. The maximum deflection is *ca.* 10 μm at 500 °C, and this value is not significant compared with the membrane radius of 282 μm, indicating excellent mechanical stability at high temperatures. This small deformation should not affect the gas sensing characteristics of any sensing films (and is shown to be the case in chapters 5 and 6).

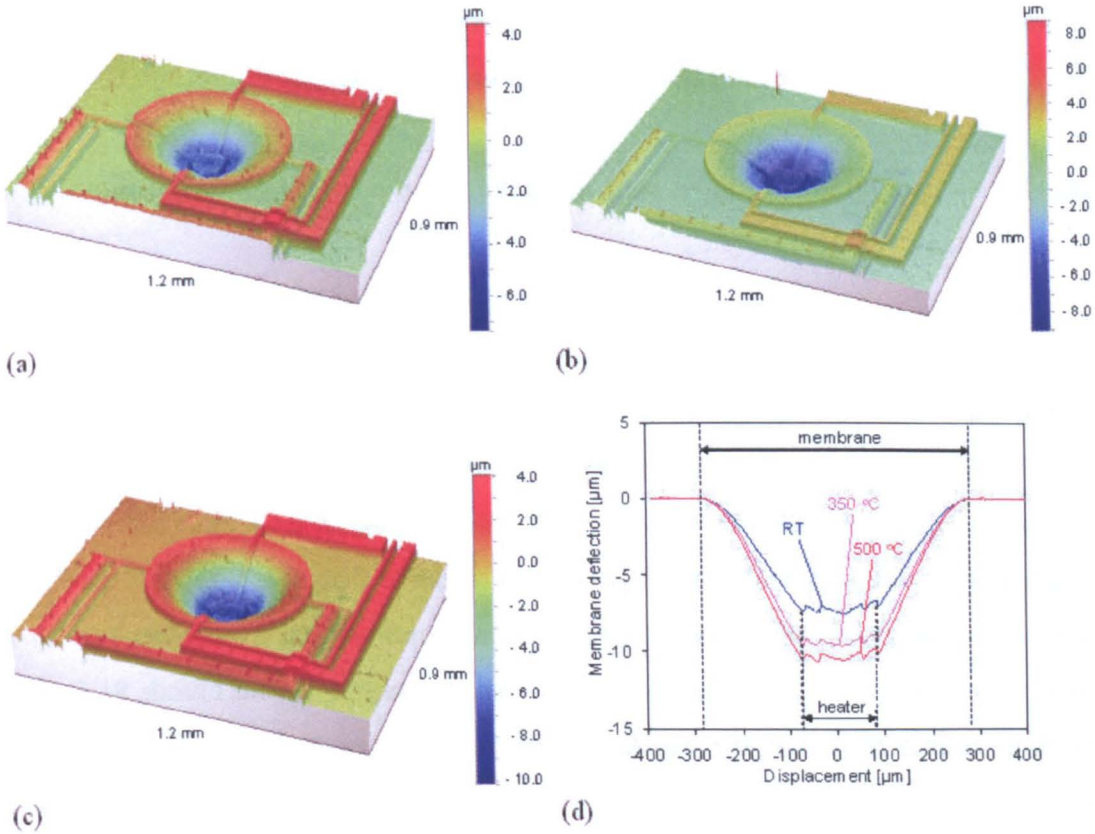

Figure 3.18. Wyko images at (a) room temperature, (b) 350 °C and (c) 500 °C, and (d) cross-sectional deflection profiles.

3.3.6 Long term stability

The long term stability is a characteristic of micro-hotplates that cannot be predicted using FEM simulation, and is an important parameter. The micro-hotplates with different heater material (SRL288A for $n+$, SRL290A for $p+$ and SRL290C for polysilicon) were tested. They were continuously operated with a constant operating voltage in a temperature controlled room at 20 °C. Two devices were tested for each heater material at 350 °C and one device for each material at 500 °C. The temperatures were chosen to be typical temperatures of metal oxide gas sensors (350 °C) and pellistors (500 °C). The resistances were measured from time to time during the test period of 500 hours.

The results are shown in figure 3.19. Two devices showed almost identical resistance drift at 350 °C for all the materials, indicating the accuracy of the experiments. It was found that the $p+$ heater was much more stable than $n+$ or polysilicon (n-type) at both 350 and 500 °C. The drift of the $p+$ heater was less than 1 % after being operated at 500 °C for 500 hours.

It had been expected that the single crystal silicon would have better reliability than polysilicon. However, the following observations had not been predicted:

1. The polysilicon heater has a better reliability than *n*+ at 350 °C (though *n*+ is better at 500 °C).
2. The *p*+ heater has a far better reliability than *n*+.

The precise cause of neither observation 1 or 2 is not known, and thus further experiments are needed to find it (*e.g.* Transmission electron microscopy (TEM) analysis before and after reliability tests). Here a possible reason for observation 2 is described. The resistance drift of single crystal silicon may be due to the stress induced by the deformation of the membrane at high temperatures. The deformation shown in figure 3.18 should induce a stress in the resistive heater. Interestingly, Demenet *et al.* reported that the yield stress of n-type heavily doped single crystal silicon is much lower than that of intrinsic silicon, whereas p-type doping has only a small effect on yield stress [3.6]. The reported values of yield stress at 500 °C are 60, 180 and 210 MPa for n-type (6×10^{18} cm^{-3}), p-type (1×10^{18} cm^{-3}), and intrinsic silicon. This lower n-type value is natural because the dislocation velocity of heavily doped n-type silicon is much faster (*ca.* 10 ×) than that of p-type silicon at 500 °C [3.7]. Therefore, it is possible that the membrane deformation is causing an increased plastic deformation of *n*+ over p+ during operation. Furthermore, it is also known that the dislocation motion during plastic deformation causes the multiplication of dislocations [3.8], and it is these dislocations that could cause the increase in the resistivity, hence resistance [3.9]. This would result in an increased drift in *n*+ heaters over *p*+ (observation 2).

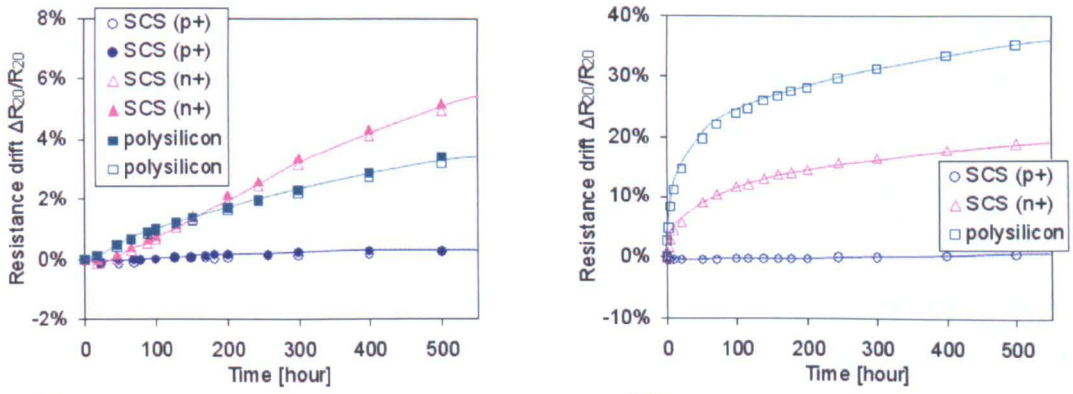

(a) (b)

Figure 3.19. Resistance drift of the micro-hotplates at (a) 350 °C and (b) 500 °C.

3.4 Conclusions

In this chapter, we have described the fabrication and characterisation of the novel SOI-CMOS micro-hotplates employing single crystal silicon as heater materials. The fabrication was performed using three commercial foundries: XFAB (Germany) for SOI-CMOS process, Silex Microsystems (Sweden) for DRIE and Pac Tech (Germany) for Au/Ni electroless plating. The proposed fabrication process makes the best use of a commercial SOI-CMOS process as follows:

1. The trench etching process to isolate MOSFETs is used to define the heater structure.
2. The source and drain implantation process ($n+$ or $p+$) is used to dope single crystal silicon and form resistive heaters.

This makes it possible to integrate the micro-hotplate with associated circuitry without any additional processing. Two types of metallization were used in the SOI-CMOS process: tungsten and aluminium, and both types were fabricated successfully with very low standard deviations of resistances of less than 2 %.

It was found that the fabricated devices have ultra-low power consumption and low operating voltage of 9.4 mW, 3.35 V for calorimeter (SRL287e) and 11.6 mW, 3.71 V for chemoresistor (SRL289g), both to operate at 500 °C, which we believe are the smallest reported in the literatures. Furthermore, the following facts, which can be used to improve the characteristics of micro-hotplates further, were found:

1. 2D FEM simulation, which is much simpler than 3D ones, provides good agreement with experiments, and can be used when designing micro-hotplates.
2. The power consumption of micro-hotplates, with the size of this range, are governed by conduction through the membrane only, and thus can be predicted using only membrane to heater ratio.
3. It is possible to decrease the operating voltage of the micro-hotplates without changing the power consumption by decreasing the resistance value of the heaters.

Furthermore, and the most importantly, long term stability tests of the micro-hotplates were performed for the first time. It was found that the drift of the micro-hotplates with $p+$ resistive heater is only less than 1 % even after operated at 500 °C for 500 hours, which is significantly smaller than that with traditional polysilicon or even $n+$. This is a significant observation when considering the commercialisation of micro-hotplates and calibration periods.

References

[3.1] X-FAB Semiconductor Foundries, "Process Specification XI10 – 1.0 μm process", June 2001.

[3.2] Z. Tang, S.K.H. Fung, D.T.W. Wong, P.C.H. Chan, J.K.O. Sin and P.W. Cheung, "An integrated gas sensor based on tin oxide thin-film and improved micro-hotplate", Sensors and Actuators B 46, 1998, pp.174-179.

[3.3] J.W. Gardner, V.K. Varadan and O.O. Awadelkarim, "Microsensors, MEMS, and Smart Devices", Chichester: Wiley, 2001.

[3.4] U. Dibbern, "A substrate for thin-film gas sensors in microelectronic technology", Sensors and Actuators B, 2, pp. 63-70, 1990.

[3.5] S.Z. Ali, P.K. Guha, C.C.C. Lee, F. Udrea, W.I. Milne, T. Iwaki, J.A. Covington, J.W. Gardner, S. Maeng and J. Park, "High Temperature SOI CMOS Tungsten Micro-Heaters", Proceedings of IEEE Sensors 2006, 2006, pp.847-850.

[3.6] J. L. Demenet, J. C. Desoyer, J. Rabier and P. Veyssiere, "On the plasticity of silicon below 650 °C", Scripta Metallurgica, Vol. 18, 1984, pp. 41-45.

[3.7] J. R. Patel, L. R. Testardi, and P. E. Freeland, "Electronic effects on dislocation velocities in heavily doped silicon", Physical Review B, Vol.13, No. 8, 1976, pp. 3548-3557.

[3.8] K. Sumino, "Deformation behavior of silicon", Metallurgical and Materials Transactions A, Vol. 30A, 1999, 1465-1479.

[3.9] R. H. Glaenzer and A. G. Jordan, "The electrical properties of dislocations in silicon –II, The effects in conductivity", Solid-State Electronics, 1969, Vol. 12, pp. 259-266.

CHAPTER 4

Novel temperature modulation technique for carbon black/polymer composite chemoresistors and its theoretical derivation

4.1 Introduction

As described in chapter 1, carbon black/polymer composite chemoresistors are attractive sensors for battery-operated gas/vapour detectors [4.1], because they operate close to room temperature and so require very low power consumption (~ mW) when compared with commercial metal oxide chemoresistors (*e.g.* 500 mW) [4.2].

Temperature modulation is a method not only to reduce power consumption but also to enable a single sensor to detect more than one vapour (or odour). This technique has been previously investigated for resistive metal oxide based gas sensors [4.3], but, to date, no one has used this technique for carbon black/polymer composite sensors. Thus it is believed to be the first attempt to do so. It is known that the resistance of carbon black/polymer composites has a strong temperature coefficient; in fact based upon solvation theory the logarithm of their response is simply proportional to the inverse of the absolute temperature [4.4]. In practice this limits the maximum operating temperature (*e.g.* 60 °C) and thus previously it has not been seen as an obvious choice of measurement technique to enhance selectivity.

In this chapter, a novel temperature modulation technique for resistive carbon black/polymer composite sensors is proposed. Temperature transient signals are generated and analysed in order to identify and quantify different organic vapours in air.

4.2 Modelling of transient conductance associated with a temperature step in a single vapour

A carbon black/polymer composite film comprises an insulating polymer into which carbon black nano-particles are dispersed to form electrical pathways. When exposed to a vapour, the molecules (solute) diffuse (*i.e.* partition) into the film (solvent) causing it to swell. This swelling increases the average separation of the conducting nanospheres and thus increases the electrical resistance of the film. Previous work has shown that the change in electrical resistance is approximately proportional to the concentration of the vapour in air, *i.e.* it obeys Henry's adsorption law at low concentrations. In a linear solvation process, the concentration c of vapour molecules dissolved in the polymer is simply proportional to that in the vapour phase. The proportional constant or partition coefficient $K(T)$ is defined as:

$$K(T) = \frac{c_{polymer}(T)}{c_{vapour}} \tag{4.1}$$

where c_{vapour} is the vapour concentration in air and $c_{polymer}(T)$ is its concentration in the polymer film.

It is well known that the partition coefficient is a function of temperature:

$$\Delta H_0 = -RT \ln[K(T)] \tag{4.2}$$

where ΔH_0 is the standard enthalpy change for the interaction between the polymer and the vapour molecule, which is a constant specific to the system, and R is the gas constant [4.5]. Thus, if temperature increase from T_1 to T_2 ($T_1 < T_2$) under constant ambient vapour concentration, then the vapour concentration in the polymer decreases from $c_{polymer}(T_1)$ to $c_{polymer}(T_2)$. In other words vapour molecules have diffused out of the polymer and into the air as $c_{polymer}(T_2)$ is smaller than $c_{polymer}(T_1)$. (Note: When the

temperature is reduced from T_2 to T_1, vapour molecules diffuse into the polymer from the air). The diffusion process is governed by a diffusion coefficient of the vapour at T_2, which is specific to the type of vapour and polymer (Note: We assume that the diffusion takes place at T_2, i.e. that the temperature change is instantaneous. This is not an unreasonable assumption when considering the thermal time constant for an SOI membrane with an embedded heater is microseconds as the heat only has to travel about 2.5 microns.). We can use the behaviour of the transient signals to identify different organic vapours in air.

To calculate this transient conductance for a step temperature change from T_1 to T_2, we first assume that the diffusion of vapour into the polymer is a linear process and simply follows Fick's law [4.6] and thus:

$$\frac{\partial c(x,t)}{\partial t} = D_{T2}\frac{\partial^2 c(x,t)}{\partial x^2} \quad (0 < x < h) \tag{4.3}$$

where c is the concentration of the vapour in the polymer, h is the thickness of the film. The initial concentration profile is uniform at T_1:

$$c(x,0) = c_{polymer}(T_1) \quad (0 < x < h) \tag{4.4 a}$$

Boundary conditions are as follows:

$$c(0,t) = c_{polymer}(T_2) \tag{4.4 b}$$

$$\frac{\partial c}{\partial x} = 0 \quad (x = h) \tag{4.4 c}$$

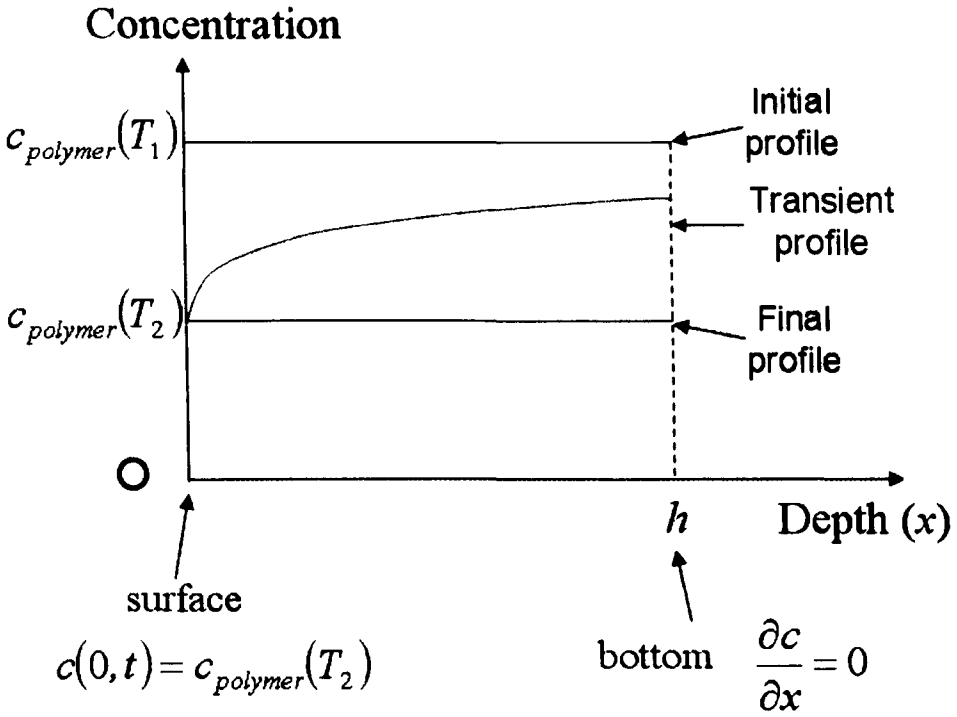

Figure 4.1. Illustration of the diffusion problem when temperature increases instantaneously from T_1 to T_2.

Equation (4.4 b) shows that the concentration at the surface of the polymer is independent of time and a constant value of $c_{polymer}(T_2)$, and equation (4.4 c) expresses the condition where there is no flux through the substrate on which the film lies, i.e. it is impermeable. The analytical solution to the model is sketched out in figure 4.1.

Solving equation (4.3) under the conditions of equations (4.4 a) – (4.4 c) and using equation (4.1), we derive the following expression for the vapour molecule concentration profile in the polymer (The solution for the partial differential equation (4.3) is found in *e.g.* [4.7]):

$$c(x,t) = c_{vapour}\left[K(T_2) - \frac{4}{\pi}(K(T_2) - K(T_1)) \cdot \sum_{m=1}^{\infty}\left[\frac{1}{2m-1} exp\left(-\frac{\pi(2m-1)^2 D_{T2}}{4h^2} t\right) sin\left(\frac{\pi}{2h}(2m-1)x\right)\right]\right] \quad (4.5)$$

The change in local conductivity is assumed linearly proportional to the local vapour concentration, hence:

$$\Delta\sigma(x) = -Nc(x) \tag{4.6}$$

where N is a constant. To calculate the fractional difference of the transient conductance G of a thin film sensor, it is necessary to integrate the local conductance change along a line orthogonal to the film plane (Note: This assumes that the electric field is a constant within the field and so independent of distance x; and is a reasonable approximation when the interdigitated electrode gap is larger than the film thickness. Otherwise the electric field is non-linear and the line integral has a geometric term):

$$\begin{aligned}\frac{\Delta G(t)}{G_{T2,dry}} &= \frac{G_{T2}(t) - G_{T2,dry}}{G_{T2,dry}} = \frac{1}{h}\int_0^h \Delta\sigma(x)dx \\ &= -Nc_{vapour}\left[K(T_2) - \frac{8}{\pi^2}\{K(T_2) - K(T_1)\}\cdot\right. \\ &\left.\sum_{m=1}^{\infty}\left[\frac{1}{2m-1}exp\left(-\frac{\pi(2m-1)^2 D_{T2}}{4h^2}t\right)\right]\right]\end{aligned} \tag{4.7}$$

where $G_{T2,dry}$ is the conductance in dry air (without any vapours). Using the following well-known formula to calculate the infinite series (see [4.8]):

$$\sum_{k=1}^{\infty}\frac{1}{(2k-1)^2} = \frac{\pi^2}{8} \tag{4.8}$$

we find the initial and final values of the fractional change in conductance as follows:

$$\frac{\Delta G(0)}{G_{T2,dry}} = -Nc_{vapour}K(T_1) \tag{4.9 a}$$

$$\frac{\Delta G(\infty)}{G_{T2,dry}} = -Nc_{vapour}K(T_2) \tag{4.9 b}$$

These parameters are proportional to both vapour concentration and partition coefficient at the two temperatures. Using equations (4.7), (4.9 a) and (4.9 b), the amplitude and the normalized transient of (4.7) is calculated as follows:

$$\text{(Amplitude)} \quad \left|\frac{\Delta G(\infty)}{G_{T2,dry}} - \frac{\Delta G(0)}{G_{T2,dry}}\right| = N\left[K(T_1) - K(T_2)\right]c_{vapour} \tag{4.10 a}$$

$$\text{(Normalized transient)} \quad \left[\frac{\Delta G(t)}{G_{T2,dry}} - \frac{\Delta G(0)}{G_{T2,dry}}\right] \Bigg/ \left|\frac{\Delta G(\infty)}{G_{T2,dry}} - \frac{\Delta G(0)}{G_{T2,dry}}\right| = 1 - \frac{8}{\pi^2}\sum_{m=1}^{\infty}\left[\frac{1}{2m-1}exp\left(-\frac{\pi(2m-1)^2 D_{T2}}{4h^2}t\right)\right] \tag{4.10 b}$$

The other transient (temperature decreased from T_2 to T_1) is found the same way and thus the results are written as follows (Note: Here the diffusion coefficient is D_{T1} rather than D_{T2} as the diffusion is assumed to take place at T_1 this time):

(Concentration profile)

$$c(x,t) = c_{vapour}\left[K(T_1) - \frac{4}{\pi}\left(K(T_1) - K(T_2)\right)\cdot \sum_{m=1}^{\infty}\left[\frac{1}{2m-1}exp\left(-\frac{\pi(2m-1)^2 D_{T1}}{4h^2}t\right)sin\left(\frac{\pi}{2h}(2m-1)x\right)\right]\right] \tag{4.11}$$

(Fractional difference of the transient conductance)

$$\frac{\Delta G(t)}{G_{T1,dry}} = \frac{G_{T1}(t) - G_{T1,dry}}{G_{T1,dry}} = -Nc_{vapour}\left[K(T_1) - \frac{8}{\pi^2}\left\{K(T_1) - K(T_2)\right\}\cdot \sum_{m=1}^{\infty}\left[\frac{1}{2m-1}exp\left(-\frac{\pi(2m-1)^2 D_{T1}}{4h^2}t\right)\right]\right] \tag{4.12}$$

(Amplitude of the fractional difference of the transient conductance)

$$\left|\frac{\Delta G(\infty)}{G_{T1,dry}} - \frac{\Delta G(0)}{G_{T1,dry}}\right| = N\left[K(T_1) - K(T_2)\right]c_{vapour} \tag{4.13 a}$$

(Normalized fractional difference of the transient conductance)

$$\left[\frac{\Delta G(t)}{G_{T1,dry}} - \frac{\Delta G(\infty)}{G_{T1,dry}}\right] \Bigg/ \left|\frac{\Delta G(\infty)}{G_{T1,dry}} - \frac{\Delta G(0)}{G_{T1,dry}}\right| = \frac{8}{\pi^2}\sum_{m=1}^{\infty}\left[\frac{1}{2m-1}exp\left(-\frac{\pi(2m-1)^2 D_{T1}}{4h^2}t\right)\right] \tag{4.13 b}$$

From equations (4.10 a) and (4.10 b) (or (4.13 a) and (4.13 b)), we can conclude:

a. The amplitude of the fractional difference of transient conduction is proportional to the ambient vapour concentration (proportional constant is $N\left[K(T_1) - K(T_2)\right]$).
b. The shape of the normalized fractional difference of transient conductance curve depends on the diffusion coefficient, which is vapour specific, but independent on the ambient vapour concentration.

Therefore, it should be possible to identify different vapours with just one sensor using the shape of the curve and then quantify them using the amplitude.

It should be noted that we have considered an ideal situation i.e. the thermal response time of the micro-hotplate is negligible, and thus used the time independent conductance in dry air $G_{T2,dry}$ to calculate the fraction for equations (4.7) and (4.12). However, in practice, the response time of the electrical conductance of polymer has a finite value (*e.g.* 10 ms) even in dry air, and thus the following expression with time dependent conductance in dry air should be used to pre-process the experimental data rather than equation (4.7) and (4.12):

$$\frac{\Delta G(t)}{G_{T2,dry}(t)} = \frac{G_{T2}(t) - G_{T2,dry}(t)}{G_{T2,dry}(t)} \tag{4.14}$$

Therefore, we require the transient conductance of both with and without vapours to calculate (4.14).

Finally, concentration profiles of equations (4.5) and (4.11) for $h = 1$ [μm] and $D_{T1} = D_{T2} = 1 \times 10^{-8}$ [cm^2/s] is calculated and plotted in figure 4.2. Also, a normalized fractional difference of transient conductance when temperature increases from T_1 to T_2 for $h = 1$ [μm] and $D_{T2} = 1 \times 10^{-7}$, 1×10^{-8}, 1×10^{-9} [cm^2/s] is calculated and plotted in figure 4.3.

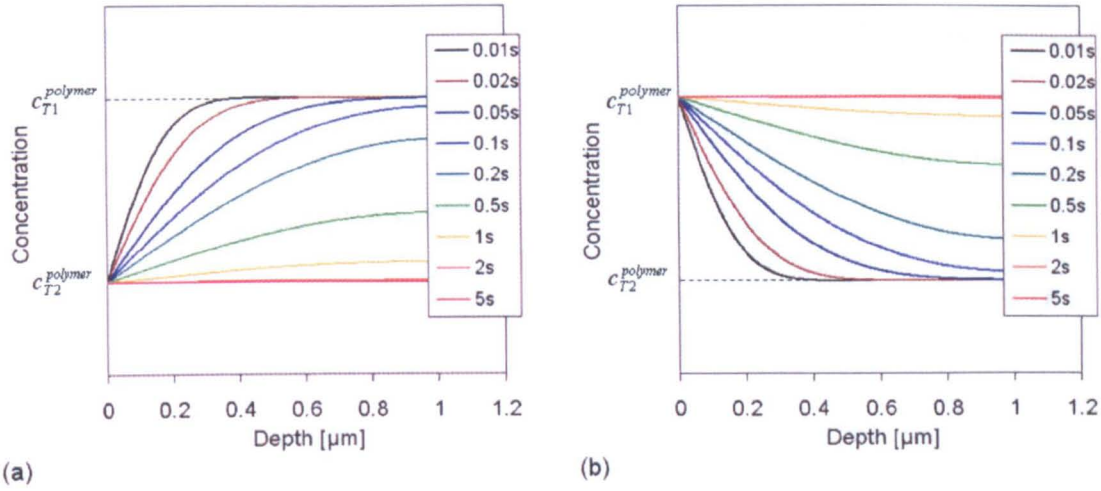

Figure 4.2. Calculated transient concentration profiles (a) when temperature step increases from T_1 to T_2 and (b) when temperature step decreases from T_2 to T_1.

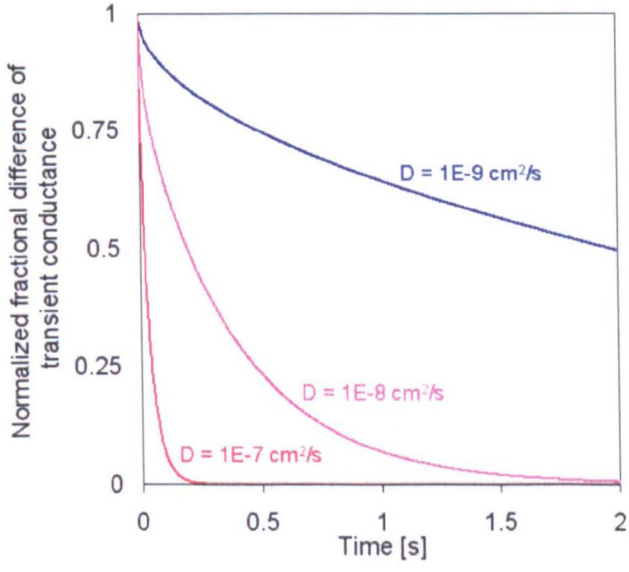

Figure 4.3. Calculated normalized fractional difference of transient conductance when temperature steps up from T_1 to T_2.

4.3 Modelling of transient conductance associated with a temperature step in a mixture of vapours

In this section, transient conductance of carbon black/polymer composite associated with a temperature step in a mixture of n vapours is discussed. Again, we first consider the transient when the temperature steps up from T_1 to T_2 ($T_1 < T_2$)). Assuming that the diffusion coefficient of each vapour molecule species is not affected by other vapour species, the diffusion equation for each vapour can be solved independently and in exactly the same way as described in the previous section. Thus the transient concentration profile of each vapour is written as follows:

$$c_i(x,t) = c_{vapour,i}\left[K_i(T_2) - \frac{4}{\pi}(K_i(T_2) - K_i(T_1))\cdot \sum_{m=1}^{\infty}\left[\frac{1}{2m-1}exp\left(-\frac{\pi(2m-1)^2 D_{T2,i}}{4h^2}t\right)sin\left(\frac{\pi}{2h}(2m-1)x\right)\right]\right] \quad (4.15)$$

where i is the suffix for each vapour species. Previous work has shown that the response of carbon/black polymer composite is generally linearly additive for organic vapours [4.5]. Therefore it is natural to assume that the change in local conductance is proportional to the weighted sum of the local concentration of all the vapours in the mixtures:

$$\Delta\sigma(x) = -\sum_{i=1}^{n} N_i c_i(x) \quad (4.16)$$

where N_i is the proportional constant which is specific to the type of vapours. Thus the fractional response is:

$$\frac{\Delta G(t)}{G_{T2,dry}(t)} = \frac{G_{T2}(t) - G_{T2,dry}(t)}{G_{T2,dry}(t)} = \frac{1}{h}\int_0^h \Delta\sigma(x)dx$$
$$= \sum_{i=1}^{n} N_i c_{vapour,i}\left[K_i(T_2) - \frac{8}{\pi^2}\{K_i(T_2) - K_i(T_1)\}\cdot \sum_{m=1}^{\infty}\left[\frac{1}{2m-1}exp\left(-\frac{\pi(2m-1)^2 D_{T2,i}}{4h^2}t\right)\right]\right] \quad (4.17)$$

This is apparently the superposition of the transient for each vapour. Using (4.8) again we find following expressions:

$$\frac{\Delta G(0)}{G_{T2,dry}} = \sum_{i=1}^{n} N_i K_i(T_1)\cdot c_{vapour,i} \quad (4.18\text{ a})$$

$$\frac{\Delta G(\infty)}{G_{T2,dry}} = \sum_{i=1}^{n} N_i K_i(T_2)\cdot c_{vapour,i} \quad (4.18\text{ b})$$

(Amplitude)

$$A = \left|\frac{\Delta G(\infty)}{G_{T2,dry}} - \frac{\Delta G(0)}{G_{T2,dry}}\right| = \sum_{i=1}^{n} N_i\left[K_i(T_1) - K_i(T_2)\right]\cdot c_{vapour,i}$$
$$\equiv \sum_{i=1}^{n} a_i \cdot c_{vapour,i} \quad (4.19\text{ a})$$

(Normalized transient)

$$\left[\frac{\Delta G(t)}{G_{T2,dry}} - \frac{\Delta G(\infty)}{G_{T2,dry}}\right] \Big/ \left[\frac{\Delta G(0)}{G_{T2,dry}} - \frac{\Delta G(\infty)}{G_{T2,dry}}\right]$$
$$= \sum_{i=1}^{n}\left[1 - a_i c_{vapour,i} \Big/ \sum_{i=1}^{n} a_i c_{vapour,i} \cdot \frac{8}{\pi^2}\sum_{m=1}^{\infty}\left[\frac{1}{2m-1}exp\left(-\frac{\pi(2m-1)^2 D_{T2}}{4h^2}t\right)\right]\right] \quad (4.19\text{ b})$$
$$= \sum_{i=1}^{n}\left[1 - a_i c_{vapour,i}/A \cdot f_i(t)\right]$$

The other transient (when temperature steps from T_2 to T_1) is modelled almost the same way and thus the results are just written as follows:

(Concentration profile)

$$c_i(x,t) = c_{vapour,i}\left[K_i(T_1) - \frac{4}{\pi}(K_i(T_1) - K_i(T_2))\cdot \sum_{m=1}^{\infty}\left[\frac{1}{2m-1}exp\left(-\frac{\pi(2m-1)^2 D_{T1,i}}{4h^2}t\right)sin\left(\frac{\pi}{2h}(2m-1)x\right)\right]\right] \quad (4.20)$$

(Fractional difference of the transient conductance)

$$\frac{\Delta G(t)}{G_{T1,dry}} = \frac{G_{T1}(t) - G_{T1,dry}}{G_{T1,dry}} = \sum_{i=1}^{n} N_i c_{vapour,i}\left[K_i(T_1) - \frac{8}{\pi^2}\{K_i(T_1) - K_i(T_2)\}\cdot \sum_{m=1}^{\infty}\left[\frac{1}{2m-1}exp\left(-\frac{\pi(2m-1)^2 D_{T1,i}}{4h^2}t\right)\right]\right] \quad (4.21)$$

(Amplitude of the fractional difference of the transient conductance)

$$A = \left|\frac{\Delta G(\infty)}{G_{T2,dry}} - \frac{\Delta G(0)}{G_{T2,dry}}\right| = \sum_{i=1}^{n} N_i[K_i(T_1) - K_i(T_2)]\cdot c_{vapour,i} \equiv \sum_{i=1}^{n} a_i \cdot c_{vapour,i} \quad (4.22\text{ a})$$

(Normalized fractional difference of the transient conductance)

$$g(t) = \left[\frac{\Delta G(t)}{G_{T2,dry}} - \frac{\Delta G(0)}{G_{T2,dry}}\right] \Big/ \left|\frac{\Delta G(\infty)}{G_{T2,dry}} - \frac{\Delta G(0)}{G_{T2,dry}}\right| = \sum_{i=1}^{n}\left[a_i c_{vapour,i} \Big/ \sum_{i=1}^{n} a_i c_{vapour,i} \cdot \frac{8}{\pi^2}\sum_{m=1}^{\infty}\left[\frac{1}{2m-1}exp\left(-\frac{\pi(2m-1)^2 D_{T2}}{4h^2}t\right)\right]\right] \equiv \sum_{i=1}^{n}\left[a_i c_{vapour,i}/A \cdot f_i(t)\right] \quad (4.22\text{ b})$$

From equations (4.19 a) and (4.19 b) (or (4.22 a) and (4.22 b)), it can be concluded that:

c. The amplitude of the fractional difference of transient conductance is an weighted sum of the all the ambient vapour concentrations, where the weight is $a_i = N_i[K_i(T_1) - K_i(T_2)]$).

d. The shape of the normalized fractional difference of transient conductance curve is an weighted average of the normalized transient curve $f_i(t)$ of the all the vapours, where the weight is $a_i c_{vapour,i}$.

From these conclusions, it is possible to identify and quantify each vapour in a mixture. Again the transient when temperature steps up from T_1 to T_2 is first considered. Suppose a transient curve for a mixture with the amplitude of A_{exp} and the normalized transient curve of (t_j, g_j) (j =1,...., N) (interval: Δt) is measured. We can find $c_{vapour,i}$ using a least-squares fit i.e. choosing $c_{vapour,1}$, ..., $c_{vapour,n}$ which minimise the following sum of the squares:

$$\chi^2 = \sum_{j=1}^{N}[g_j - g((j-1)\Delta t)]^2$$
$$= \sum_{j=1}^{N}\left[g_j - \sum_{i=1}^{n}[a_i c_{vapour,i}/A_{exp} \cdot f_i((j-1)\Delta t)]\right]^2 \quad (4.23)$$

This is achieved by solving the following equations simultaneously:

$$\begin{cases} \dfrac{\partial \chi^2}{\partial c_{vapour,1}} = 0 \\ \vdots \\ \dfrac{\partial \chi^2}{\partial c_{vapour,n}} = 0 \end{cases} \quad (4.24)$$

These equations can be solved generally as long as the following conditions are satisfied:

(1) a_i and $f_i(t)$ are known

(2) (number of type of vapours, n) < (number of data points over time, N)

Conidtion (1) can easily be achieved by pre-measuring the transients for all the possible single vapours. Also, condition (2) is normally satisfied because the number of type of vapours (n) is typically less than 10 and the number of data points over time (N) is typically more than 10 (e.g. For transient time constant 1 sec and interval time (Δt) 10 ms, N is 1000) Therefore, it can be concluded that it is possible to identify and quantify each vapour in a mixture comprised of n type of vapours using this technique.

4.4 Conclusions

In this chapter, a novel temperature modulation technique for a single carbon black/polymer composite sensor has been proposed in order to enhance its ability to discriminate between different vapours. The technique can be summarised as follows:

1. Apply a square wave voltage to a resistive micro-heater to step change the sensor temperature and measure the transient sensor conductance in the presence of different vapours.
2. Use the fractional difference in transient conductance as the pre-processing feature.
3. For a single vapour, the amplitude of the fractional difference of transient conductance is used to predict the concentration; whilst the shape of the normalized curve (which is independent of vapour concentration but dependent upon vapour type) to predict vapour type. For a mixture, fractional difference of transient conductance is predicted to be superposition of those of single vapours, and thus can be used to both identify and quantify each vapour in a mixture.

The proposed technique is demonstrated in chapter 5, and more sophisticated signal/data processing ways to identify and quantify each vapour in a mixture is discussed in chapter 6.

References

[4.1] M.C. Lonergan, E.J. Severin, B.J. Doleman, S.A. Beaber, R.H. Grubbs, and N.S. Lewis, "Array-Based Vapor Sensing Using Chemically Sensitive, Carbon Black-Polymer Resistors", Chem. Mater., 8, pp. 2298–2312, 1996.

[4.2] J.W. Gardner, V.K. Varadan and O.O. Awadelkarim, Microsensors "MEMS and Smart Devices", Chichester: Wiley, 2001, pp. 227-302.

[4.3] E. Llobet, R. Ionescu, S. Al-Khalifa, J. Brezmes, X. Vilanova, X. Correig, N. Bârsan and J.W. Gardner, "Multicomponent gas mixture analysis using a single tin oxide sensor and dynamic pattern recognition", IEEE Sensors Journal, 1, 2001, pp. 207-212.

[4.4] Y.S. Kim and Y.S. Yang, "Additional thermodynamic feature extraction from chemoresistive carbon black-polymer composite sensors by temperature modulation", Sensors and Actuators B, 121, 2007, pp. 507-514.

[4.5] E.J. Severin, "Array based vapor sensing using conductive carbon black-polymer composite thin film detectors", PhD Thesis, California Institute of Technology, 1999.

[4.6] S.M. Briglin and N.S. Lewis, "Characterization of the temporal response profile of carbon black-polymer composite detectors to volatile organic vapors", J. Phys. Chem. B, 107, 2003, pp. 11031-11042.

[4.7] J. Crank, "The mathematics of diffusion", Second edition, Bristol: Oxford University Press, 1975.

[4.8] A.P. Prudnikov, Yu.A. Brychkov and O.I. Marichev (Translated from the Russian by N.M. Queen), "Integrals and series", Vol.1, Elementary functions. New York : Gordon and Breach Science Publishers, 1986.

CHAPTER 5

Characterisation of temperature-modulated carbon black/polymer composite sensors

5.1 Introduction

In chapter 4, a novel temperature modulation technique was proposed and theoretically modelled, employing a single carbon black/polymer composite resistive sensor. The temperature is modulated between two values by applying a square wave signal, then using the on and off transient curves to detect different vapours. The aim of this chapter is to study the proposed technique experimentally, and thus demonstrating its real-world application.

A carbon black/polyvinylpyrrolidone (PVP) composite was chosen as a prototypical sensing material, synthesized and deposited onto a micro-hotplate containing resistive electrodes (detailed in chapters 2 and 3) to form a chemoresistor. A square wave voltage was applied to the resistive heater to modulate the temperature periodically between two set points, and the transient sensor responses were measured in the presence of a series of vapours, namely water, methanol, ethanol, and a mixture of water and methanol. The polymer was chosen as it has a known high partition coeffient for these polar compounds. Different polymers could be chosen to detect non-polar organic compounds, such as isoprene.

5.2 Deposition of carbon black/polymer composite materials

The device SRL291C (or SRL291D, which is identical to SRL291C) has resistive electrodes with an electrode aspect ratio of 16. Aluminium metallization devices were used, as they have electroless-plated gold electrodes to make good, stable ohmic contact with the polymer). Carbon black/polyvinylpyrrolidone (PVP) composite (20 wt % carbon black), as stated before, was chosen as the sensing material. PVP in powder form was used with a molecular weight of *ca.* 40,000, supplied by Sigma Aldrich (UK). The structural formula of PVP is shown in figure 5.1. The polymer contains two atoms with strong electronegativity *i.e.* oxygen and nitrogen (electronegativity of oxygen and nitrogen atoms are 3.5 and 3.0 in Pauling's definition) [5.1]. Therefore it is expected that the carbon black/PVP composite has a larger sensitivity to polar vapours, such as alcohols than non-polar vapours. The carbon black nanospheres with a diameter of typically 50 - 80 nm (Black Pearls 2000) were supplied by Cabot Corporation (USA). The PVP was dissolved in pure ethanol at 50 °C using a magnetic stirrer for 12 hours. Then 0.3 g of carbon black was added and mixed with 20 ml of ethanol using a flask shaker (Griffin and George, UK) for 10 min. The mixture was deposited onto a micro-hotplate using a commercial air brush (HB-BC or HP-CP Iwata, Japan) through a mask made by micro-stereolithography. The device was bonded on a 68 pin ceramic package prior to deposition, and the resistance of the film was measured during deposition in order to control the thickness. The mask has two circular holes, both of which had a diameter of 400 μm, and the distance between their centres are 1.0 mm. One circular hole defined the area of the sensing film on the devices, and the other was used to measure the thickness of the film (It is difficult to measure the thickness of the sensing film on the micro-hotplate due to the membrane deformation as mentioned in chapter 3). After deposition, heat-treatment at 50 °C for 24 hours was carried out in an oven to dry out the solution and stabilize the sensor resistances. Finally, the sensors were exposed to the flow of dry air at 25 °C for 12 hours using an FIA (flow injection analysis) test station (described later).

Table 5.1 lists the three devices used in this thesis and figure 5.2 shows their photographs. They are referred to as PVP2, PVP8 and PVP11. PVP2 was deposited on 3rd March 2007, and PVP8 and PVP11 on 6th July 2007. The resistances of the film were 4.43, 1.91 and 13.65 kΩ, respectively, at 25 °C in the dry air environment in the FIA test station. The film thickness was measured using an optical interferometer

(Wyko/NT2000). The thickness of PVP8 was found to be *ca.* 6 μm. The thicknesses of PVP2 and PVP11 were difficult to measure as they were comparable with the measurement noise (typically 2 - 3 μm) caused by the surface roughness. Therefore, it has been decided to estimate the thickness of PVP11, which was deposited from the same solution on the same day as PVP8, by assuming that the resistance of the film is inversely proportional to the resistance. The estimated thickness of PVP11 was *ca.* 0.8 μm. The thickness of PVP2 was also estimated to be *ca.*1.9 μm using the same assumption. However PVP2 is not used in this thesis when discussing the thickness dependence, as it was deposited from a different solution synthesized on a different date.

Table 5.1. List of sensors used.

	Micro-hotplate	Resistance [kΩ]	Thickness [μm]	Sheet resistance [kΩ]
PVP2	SRL291C	4.43	1.9	70.9
PVP8	SRL291D	1.91	6.0	30.6
PVP11	SRL291C	13.65	0.8	218.4

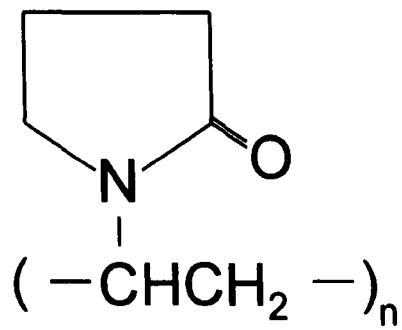

Figure 5.1. Structural formula of polyvinylpyrrolidone (PVP).

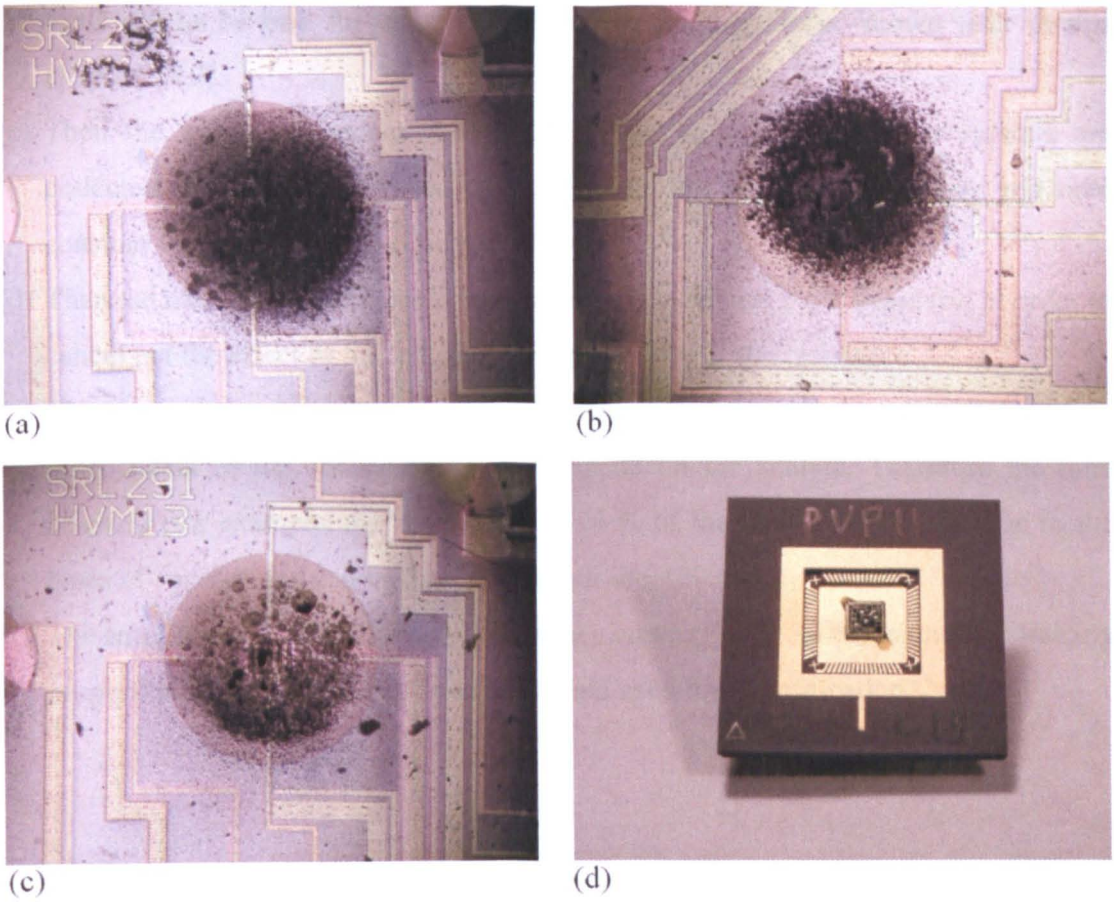

(a) (b) (c) (d)

Figure 5.2. Photographs of the SOI micro-hotplates with carbon black/PVP composite films. (a) PVP2, (b) PVP8, (c) PVP11, (d) PVP11 bonded on 68 pin ceramic package.

5.3 Characterisation

5.3.1 Processing the experimental data

Before discussing any experimental results, the way to apply the proposed technique to the experimental data is explained conceptually using figure 5.3 as follows:

(a) The temperature is modulated with the square wave using the micro-hotplate heater. Here only the off transient is considered for simplicity.

(b) The transient conductance signal of the carbon black/PVP composite film in dry air is first collected. The conductance changes (with relatively small time constant) even in the dry air, since carbon black/polymer composite generally have finite temperature coefficients of resistances (Here the temperature coefficient of the resistance of the carbon black/PVP composite film is assumed to be negative. This

turns out to be true for all the films studied in this thesis, shown later in this chapter) [5.2].

(c) Then the transient conductance signals of the sensors in different vapours are collected. The larger the vapour concentration, the larger the amplitude and time constant of the conductance change.

(d) Then the fraction is calculated using the signals in figures 5.3 (b) and (c), in order to cancel out the effect of the temperature dependence of the resistance.

(e) The transient curves are normalized. The shape of the resultant curve should be independent of the concentration, but depend on the analyte. Therefore the time constant (for example, the time to reach 50 % of the final value) is specific to the types of vapours and can be used for vapour identification.

(f) The amplitude of the fractional conductance curve (figure 5.3 (d)) should be linearly proportional to the vapour concentration and used for quantification.

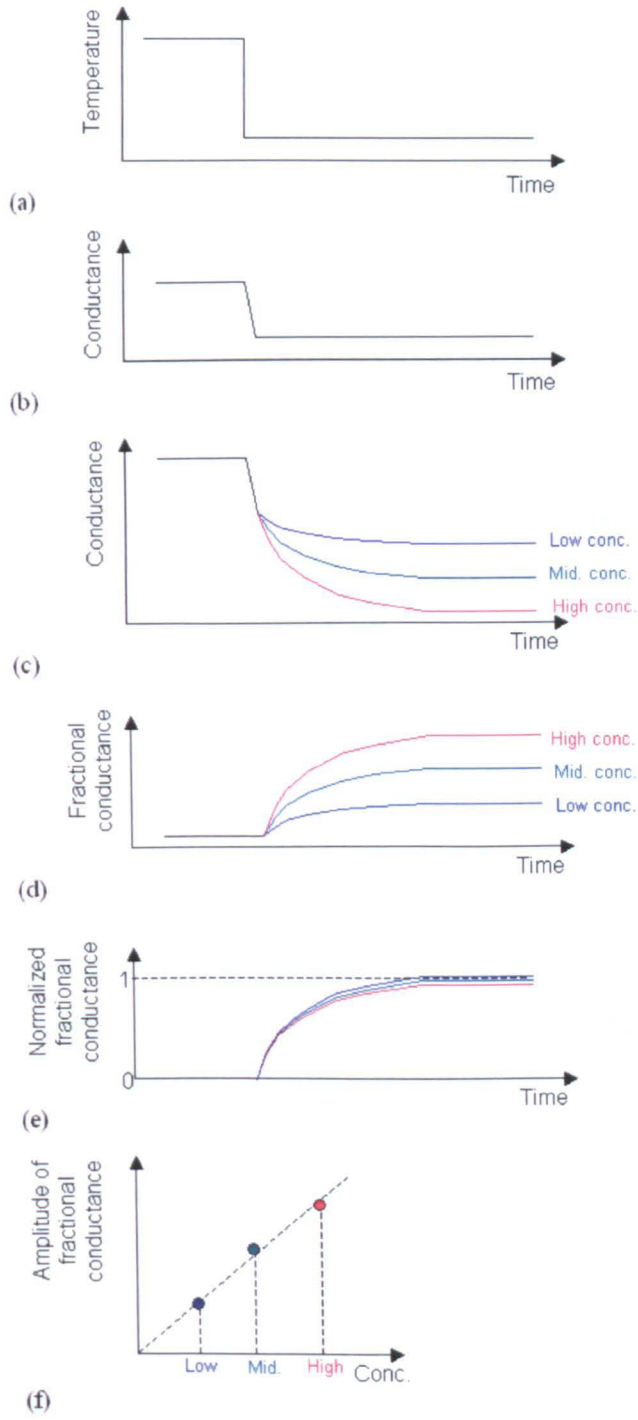

Figure 5.3. Conceptual illustration of the proposed technique. (a) Temperature off transient, (b) off transient of the sensor conductance in dry air (without vapours), (c) off transient of sensor conductance in vapours of three different concentrations, (d) fractional conductance in vapours, (e) normalized fractional conductance in vapours, (f) amplitude of fractional conductance.

5.3.2 Experiments and results

Temperature modulation experiments of the three devices (PVP2, PVP8 and PVP11) were performed. The devices were bonded onto ceramic packages and mounted in a temperature controlled stainless steel chamber in a fully automated FIA test station. The temperature of the carbon black/PVP composite film was controlled by applying a voltage to the micro-hotplate. The temperatures used in the experiments were 25 °C, 35 °C, 45 °C and 55 °C, which require operating voltages (and powers) of 0 V (0 mW), 0.78 V (0.8 mW), 1.10 V (1.6 mW) and 1.35 V (2.4 mW), respectively. The accuracy of the temperature modulation amplitude was ± 0.3 °C. The concentrations of water, methanol and ethanol vapours in the chamber were controlled independently with the uncertainty of only 5 %. A constant current of 10 μA was applied to the carbon black/PVP composite film and the voltage was recorded every 10 ms. The testing system is described in more detail in appendix A.

The results are discussed in the following order: (a) demonstration of the processing procedure, (b) concentration and vapour type dependence, (c) thickness dependence, (d) temperature dependence and (e) mixture effect.

(a) Demonstration of the processing procedure

First of all, the concentration dependence of water vapour was studied using its 'temperature off' transient to demonstrate the procedure of figure 5.3. Temperature modulation experiments of the device PVP2 were carried out with the presence of water vapour of different concentrations (0 ppm, 1000 ppm, 2000 ppm, 3000 ppm, 4500 ppm, 6000 ppm). The amplitude and frequency of the applied square wave voltage is 0.78 V (*i.e.* temperature modulation between 25 °C and 35 °C) and 50 mHz.

Figure 5.4 (a) shows the results. The temperature is 35 °C from 0 s to 10 s and 20 s to 30 s, and is 25 °C from 10 s to 20 s. (The conductance in dry air shows lower conductance at 25 °C, indicating the temperature coefficient of resistance is negative). Then, by calculating the fraction using the curves from 10 s to 20 s (temperature off transient) with and without vapour, we obtain figure 5.4 (b). Finally, the normalized fractional conductance curves and the amplitude of the fractional conductance curves are plotted as shown in figures 5.4 (c) and (d). It was found that the shape of the normalized curves does not depend on vapour concentration and the amplitude of the

fractional transient conductance curves is linearly proportional to the concentration, both as expected.

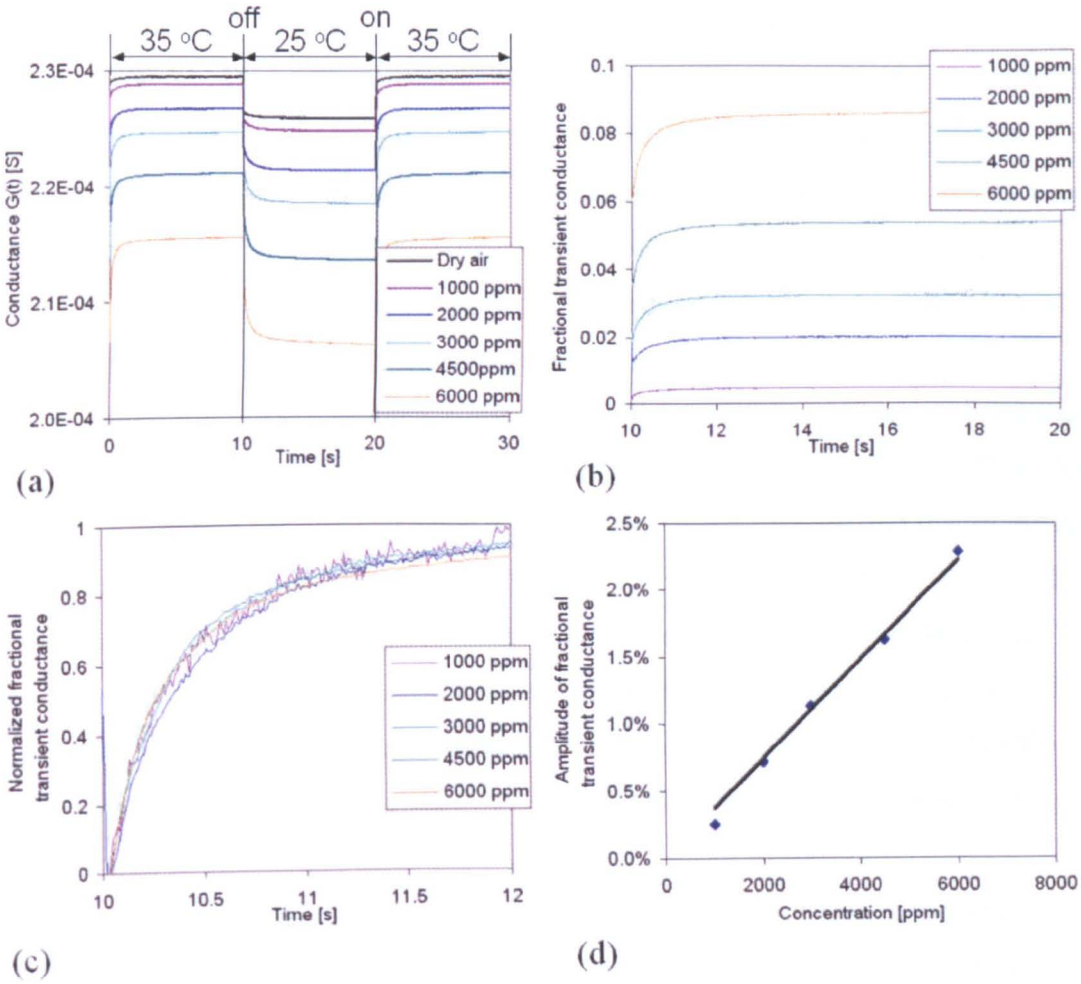

Figure 5.4. Demonstration of the processing data using the experimental results for water vapour. (a) Raw data, (b) fractional transient conductance, (c) normalized fractional transient conductance and (d) amplitudes of fractional transient conductance.

(b) Concentration and vapour type dependence

Here the results of temperature modulation experiments of device PVP2 are discussed. The experiments were performed in the presence of water, methanol and ethanol vapours of different concentrations (water: 0 ppm, 1000 ppm, 2000 ppm, 3000 ppm, 4500 ppm, 6000 ppm, methanol: 1360 ppm, 2710 ppm, 4070 ppm, 5430 ppm, ethanol: 2270 ppm, 4540 ppm, 6810 ppm, 9080 ppm). The amplitude of the applied square wave voltage is 0.78 V (*i.e.* temperature modulation between 25 °C and 35 °C), and the

frequency 50 mHz for water and methanol and 1.67 mHz for ethanol (Lower frequency was used for ethanol due to its smaller diffusion coefficient in PVP compared to water and methanol).

Figures 5.5, 5.6 and 5.7 are the normalized fractional transient conductance curves of the (a) off and (b) on transients in water, methanol and ethanol vapours. The curves for water and methanol are averages of 30 transients and that for ethanol is an average of 3 transients. (For ethanol, the data taken in every 10 ms were averaged and plotted every 0.3 s for noise reduction). The results indicate that the shape of the normalized fractional transient conductance curves are independent of vapour concentration but depend on vapour type, as predicted.

Table 5.2 lists the time constants of the normalized fractional transient conductance curves. The time constant of water is the smallest and that of ethanol the largest. Considering that the molecular mass of water is the smallest and that of ethanol is the largest, this result indicates that the species with low molecular mass diffuse faster (molecular mass of water, methanol and ethanol are 18, 32 and 46 [5.3]). The time constant of off transient is smaller than that of on transient for each vapour. This is reasonable, considering that the temperature of off transient (25 °C) is lower than that of on transient (35 °C) and the diffusion coefficient tends to be larger at higher temperatures.

Figure 5.8 plots the amplitude of fractional transient conductance vs concentration of water, methanol and ethanol for both the (a) off and (b) on transients. The amplitude of the fractional transient conductance curve of all water, methanol and ethanol for both the off and on transients is linearly proportional to the concentration, again, as predicted.

Finally, identification and quantification of vapours were carried out. The amplitude of the fractional transient conductance vs the time constant ($t_{50\%}$) for the off and on transient was plotted as shown in figure 5.9[1]. The plots clearly show that identification and quantification of water, methanol and ethanol vapour was successfully carried out using the proposed technique with either the off or on transient of the temperature modulated signal.

[1] The more precise measure of the time constant is known to be 10 % - 90 % rise (or fall) time. Here 50 % rise (or fall) time is used for simplicity.

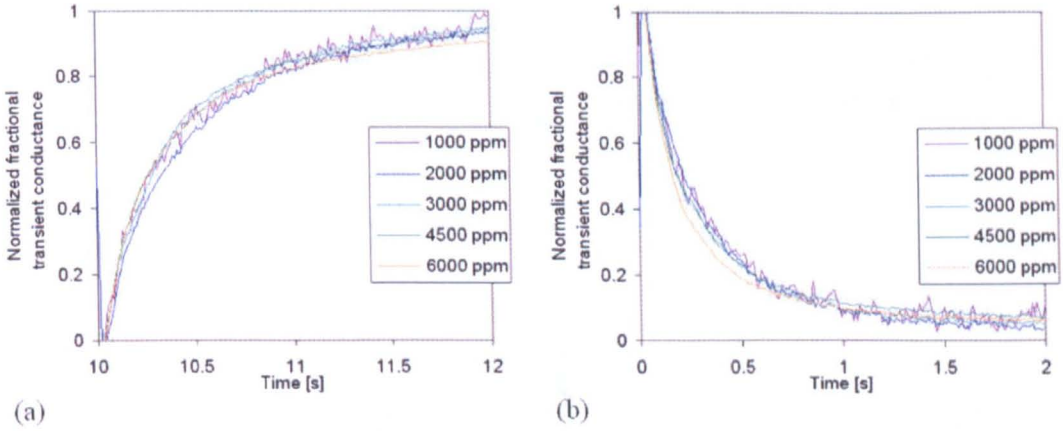

Figure 5.5. Normalized fractional transient conductance of water vapour at various concentrations: (a) off transient and (b) on transient.

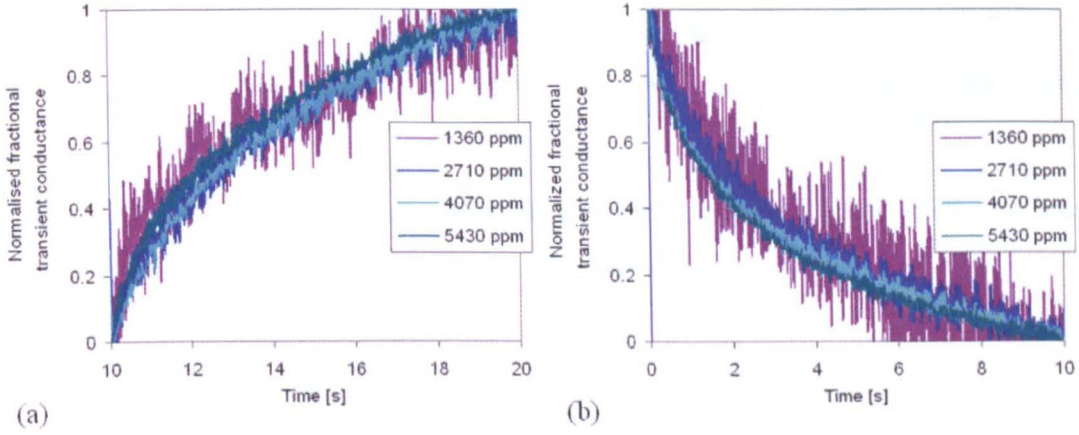

Figure 5.6. Normalized fractional transient conductance of methanol vapour at various concentrations: (a) off transient and (b) on transient.

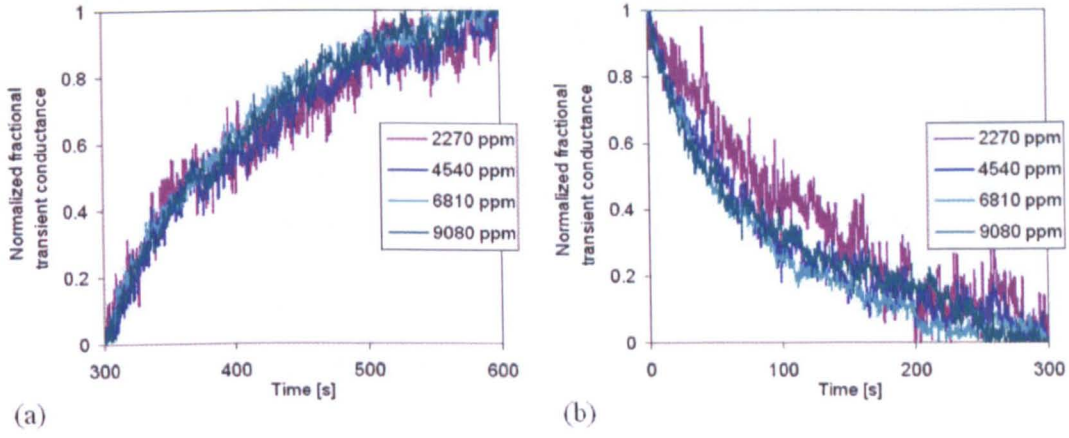

Figure 5.7. Normalized fractional transient conductance of ethanol vapour at various concentrations: (a) off transient and (b) on transient.

Table 5.2. Time constants ($t_{50\%}$) of normalized fractional transient conductance curves of PVP2 in water, methanol and ethanol vapour.

	water	methanol	ethanol
off transient	0.20 s	1.7 s	60 s
on transient	0.29 s	2.3 s	75 s

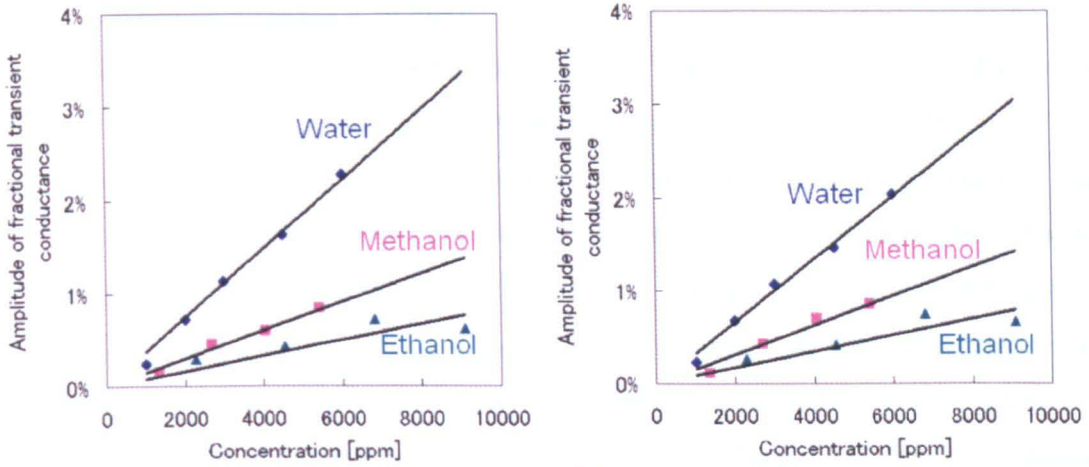

Figure 5.8. Amplitudes of fractional transient conductance of water, methanol and ethanol vapours: (a) off transient and (b) on transient.

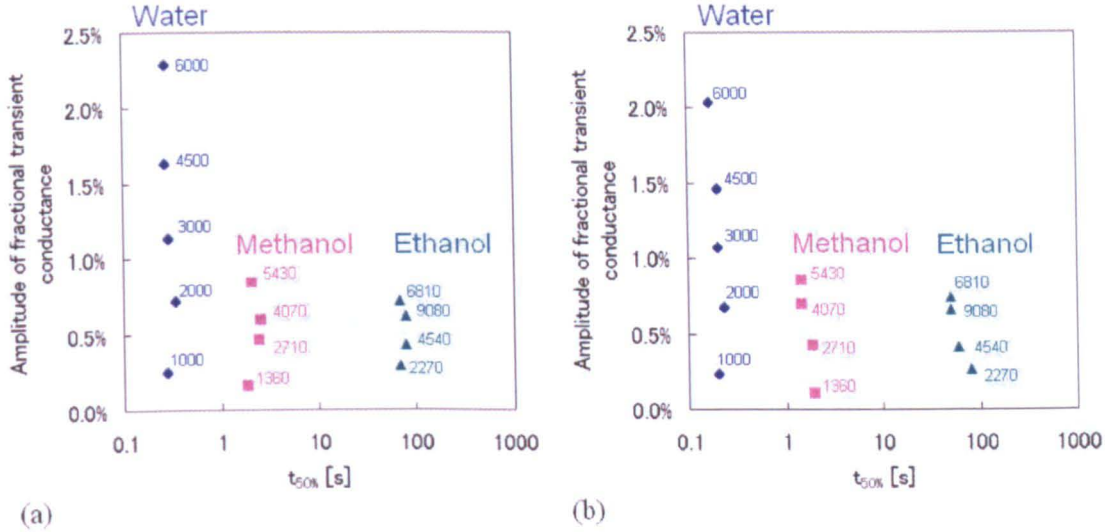

Figure 5.9. Identification and quantification of water, methanol and ethanol vapour using (a) off transient and (b) on transient.

(c) Thickness dependence

The thickness dependence was also investigated. For this experiment, devices PVP8 and PVP11 were used. Their thickness is *ca.* 6.0 μm and *ca.* 0.8 μm, respectively. The devices were tested to water with a concentration of 3000 ppm. The amplitude of the applied square wave voltage was 0.78 V (*i.e.* temperature modulation between 25 °C and 35 °C), and the frequency 50 mHz.

Figure 5.10 shows the normalized transient fractional conductance of both (a) off and (b) on transient, and table 5.3 lists the time constants ($t_{50\%}$) of PVP8 and PVP11 for both off and on transient. The time constant of the thicker film (PVP8) is 17.5 and 11.0 times as large as that of thinner film (PVP11) in off and on transient, respectively. The results suggest it is possible to modify the time constant of the proposed technique by simply modifying the thickness of the sensing film. This will allow the detection of molecules with much smaller diffusion coefficient in a shorter period of time. The theory in chapter 4 predicts that the time constant should be proportional to the square of the thickness. Therefore, the time constant of the thicker film should be (6.0 μm/0.8 μm)^2 = 56 times as much as that of the thinner one, theoretically. The discrepancy between the experiments and the theory is probably reasonable considering the uncertainty in deposition and thickness measurements and the variation in thickness of the film across the sensor.

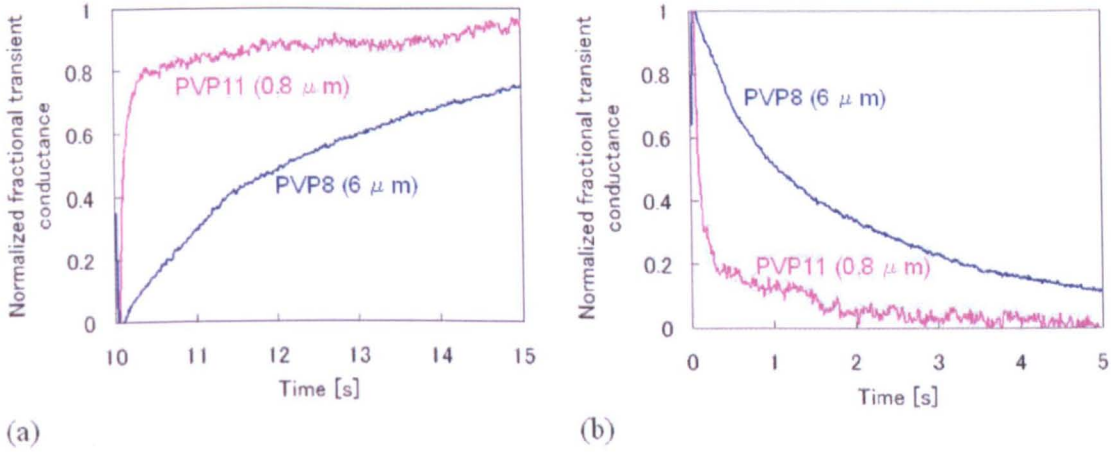

Figure 5.10. Normalized fractional transient conductance of PVP8 and PVP11 at 3000 ppm water vapour: (a) off transient and (b) on transient.

Table 5.3. Time constants ($t_{50\%}$) of normalized fractional transient conductance curves of PVP8 and PVP11 at 3000 ppm water vapour.

	PVP8 (6.0 μm)	PVP11 (0.8 μm)
off transient	2.1 s	0.12 s
on transient	1.1 s	0.10 s

(d) Temperature dependence

The temperature dependence of the steady state and transient state were investigated using methanol vapour with a concentration of 2710 ppm using the PVP11 sensor. (Measurements were also carried out in dry air for comparison). The amplitude of the applied square wave voltage was 0.78 V, 1.10 V and 1.35 V, which corresponds to temperature modulation of 25 °C ↔ 35 °C, 25 °C ↔ 45 °C and 25 °C ↔ 55 °C, respectively. The frequency is 10 mHz (retention time: 50 s).

First of all, the steady state conductance with and without methanol vapour was considered. The conductance values taken after 50 s (= retention time) from the off or on transient are used as the saturated values (or steady state values) and shown in tables 5.4, 5.5 and 5.6. Figure 5.11 shows the plot of logarithm of the steady state response ($(G_{dry} - G_{methanol})/G_{dry}$) vs the inverse of the absolute temperature ($1/T$). Their relation is linear, and this is expected as steady state response is known to follow the following relationship:

$$\frac{\Delta G}{G_{dry}} = \frac{G_{dry} - G_{methanol}}{G_{dry}} \propto \exp\left(-\frac{\Delta H_0}{RT}\right) \tag{5.1}$$

where H_0 is the standard enthalpy change for the interaction between the polymer and the vapour molecule and R the gas constant [5.4]. Therefore, it is possible to calculate the standard enthalpy from the slope of figure 5.11, and the value was found to be –27.5 [kJ/mol]. The negative value indicates that the absorption is exothermic reaction, and the relatively small value (< 30 kJ) shows that the adsorption mechanism is physisorption rather than chemical reaction [5.4].

Table 5.4. Saturated conductance when the temperature was modulated between 25 °C and 35 °C with and without methanol vapour.

	G_{dry}	$G_{methanol}$	$\Delta G/G_{dry}$
25 °C	7.412E-05	7.230E-05	2.46%
35 °C	7.538E-05	7.404E-05	1.78%

Table 5.5. Saturated conductance when the temperature was modulated between 25 °C and 45 °C with and without methanol vapour.

	G_{dry}	$G_{methanol}$	$\Delta G/G_{dry}$
25 °C	7.416E-05	7.230E-05	2.51%
45 °C	7.651E-05	7.555E-05	1.26%

Table 5.6. Saturated conductance when the temperature was modulated between 25 °C and 55 °C with and without methanol vapour.

	G_{dry}	$G_{methanol}$	$\Delta G/G_{dry}$
25 °C	7.415E-05	7.232E-05	2.47%
55 °C	7.746E-05	7.677E-05	0.89%

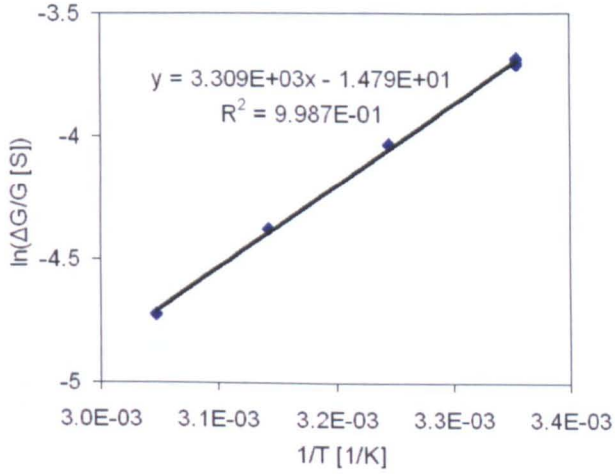

Figure 5.11. Temperature dependence of steady state response in methanol vapour.

Then the transient behaviour was investigated. Figures 5.12 (a) and (b) are the normalized fractional transient conductance curves of the off and on transient when the temperature modulated in the following ways: 25 °C ↔ 35 °C, 25 °C ↔ 45 °C and 25

°C ↔ 55 °C. The signals are the averages of the 6 transients. By subtracting the signals of figure 5.12 (b) from the unity, and plotting with those shown in figure 5.12 (a), the curves in figure 5.12 (c) are obtained. The figure shows that the transient becomes faster as the temperature increases, as predicted. Figure 5.12 (d) shows that the relationship between the logarithm of the response time ($t_{50\%}$) and the inverse of the temperature ($1/T$) is linear. Since the diffusion coefficient is inversely proportional to the time constant, it is apparent that the temperature dependence of the diffusion coefficient is Arrhenius type, with the activation energy (E_a) of 0.40 eV, which was calculated by the following equation:

$$E_a = k_B \times (slope) \tag{5.2}$$

where k_B is the Boltzmann constant.

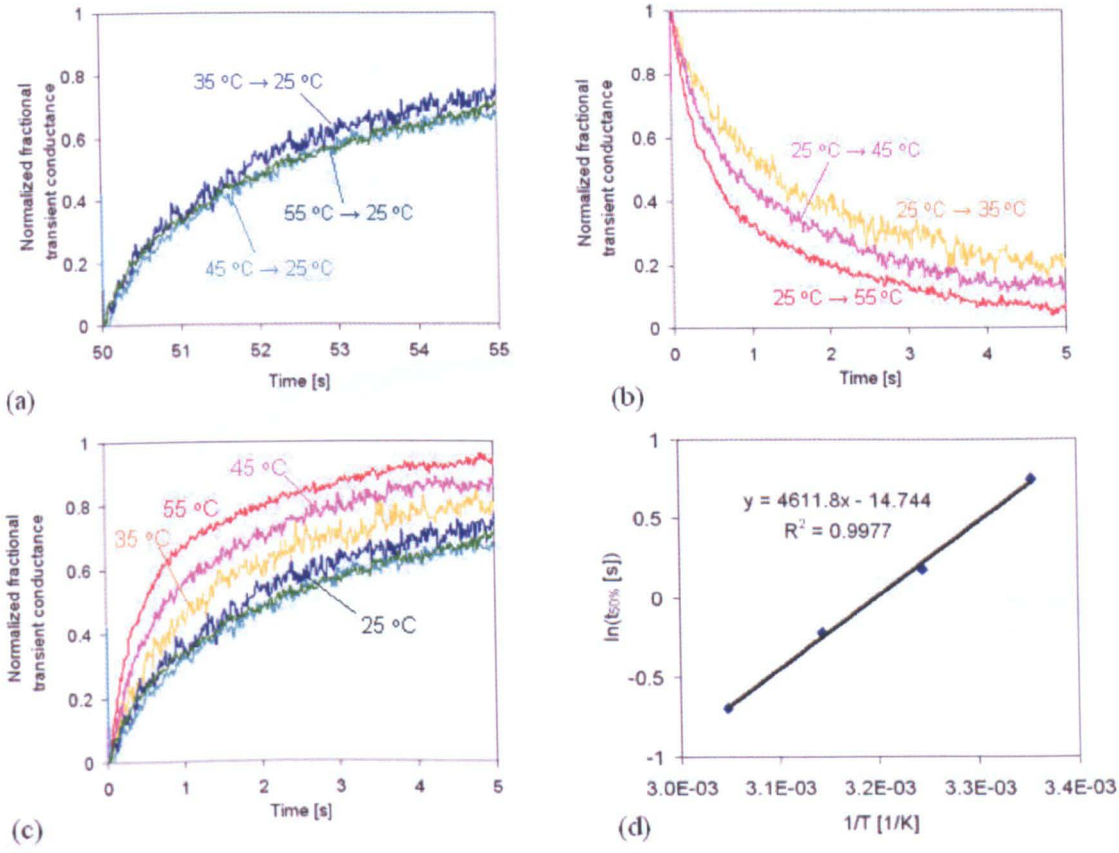

Figure 5.12. Temperature dependence of the steady state response in methanol vapour: (a) off transient, (b) on transient, (c) off and on transient and (d) logarithm of time constant vs inverse of absolute temperature.

(e) Mixture

Finally, the effect of a binary mixture was investigated. The device PVP2 was tested to a mixture of 2000 ppm water and 2710 ppm methanol. The amplitude and frequency of the applied square wave voltage was 0.78 V (*i.e.* temperature modulation between 25 °C and 35 °C) and frequency of 50 mHz.

Figures 5.13 (a) and (b) show the normalized transient fractional conductance of both the (a) off and (b) on transient in the mixture. The results of single vapour of 2000 ppm and 2710 ppm methanol and the predicted curves from the single vapour results are also plotted in the same figures. Table 5.7 shows the amplitude of all the above curves (before normalization) including the prediction. It was found that the experimental curve in the mixture is close to that of the predicted.

The results indicate that the above technique can probably be employed to identify and quantify each vapour in a binary mixture. However, one issue should be pointed out. The technique uses monotonously increasing (or decreasing) curves only. This means it is needed to separate out several curves with different time constants from noisy experimental curves in order to deal with a mixture with several different vapours, a process that is not always easy.

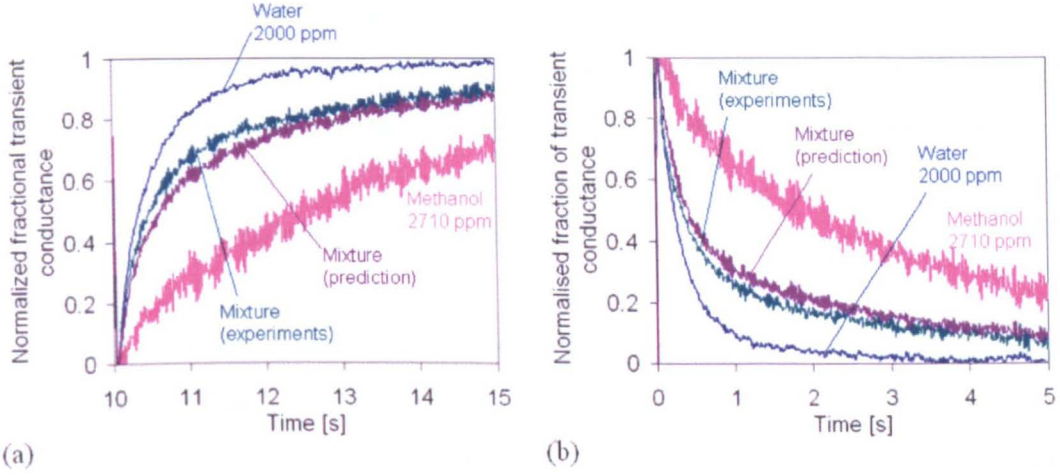

Figure 5.13. Normalized fractional transient conductance of PVP2 in a mixture of 2000 ppm water and 2710 ppm methanol vapour: (a) off transient and (b) on transient.

Table 5.7. Amplitude of fractional transient conductance in a single vapour of water and methanol, and the mixture.

Water 2000 ppm	Methanol 2710 ppm	Mixture (experiments)	Mixture (prediction)
0.72 %	0.46 %	1.21 %	1.18 %

5.4 Conclusions

In this chapter, the deposition of carbon black/polyvinylpyrrolidone composite films onto SOI micro-hotplates was carried out to form chemoresistors. The sensors were first tested to water, methanol and ethanol vapours with various concentrations (water: 0 ppm, 1000 ppm, 2000 ppm, 3000 ppm, 4500 ppm, 6000 ppm, methanol: 1360 ppm, 2710 ppm, 4070 ppm, 5430 ppm, ethanol: 2270 ppm, 4540 ppm, 6810 ppm, 9080 ppm) in order to justify the technique proposed in chapter 4 and to demonstrate identification and quantification.

The proposed technique was proven to be correct for single vapours by confirming the following facts.

1. The shape of the normalized fractional conductance of transient curves does not depend on the concentration but depends only on vapour type for water, methanol and ethanol at the above concentration range.
2. The amplitude of the fractional transient conductance is linearly proportional to the concentration of water, methanol and ethanol at the above concentration range.

Furthermore, the following facts were found:

3. The time constant of the thicker film (PVP8, 6 μm) is 10 - 20 times as large as that of the thinner film (PVP11, 0.8 μm) in off and on transient, for 3000 ppm water. This is consistent with linear diffusion theory (*i.e.* the time constant is proportional to the square of the thickness), considering the uncertainty of the thickness measurement.
4. The temperature dependence of the steady state response of 2710 ppm methanol vapour is consistent with the temperature dependence of the partition coefficient (the power law).

5. The diffusion coefficient of 2710 ppm of methanol vapour has a higher value at higher temperature (Arrhenius type).

The technique was applied to a mixture of water and methanol with the concentrations of 2000 ppm and 2710 ppm, respectively. The results indicate that the transient curves of the mixture are the superposition of single vapours, though more experiments are needed to confirm this observation.

The powers needed to keep the temperature at 35, 45 and 55 °C continuously were 0.8, 1.6 and 2.4 mW, respectively. Considering the temperature modulation was performed by applying a square wave voltage (produced by simply turning off and on the operating voltage of the heater) with the duty ratio of 50 %, the operating power of the sensor is the half of the above values *i.e.* 0.4, 0.8 and 1.2 mW for 35, 45 and 55 °C, respectively. The value is by far the smaller than those of metal oxide based chemoresistors. For example, Llobet *et al.* reported on results of multi-component gas mixture analysis using Pd doped tin oxide film on a platinum based micro-hotplate [5.5]. They modulated the temperature between 243 °C and 405 °C by applying a sinusoidal wave voltage, and it requires much more than 80 mW (which is a value needed to operate their micro-hotplate at the minimum temperature of 243 °C continuously [5.6]). In addition, it should be noted that only the large micro-hotplates (SRL291C and SRL291D) were used in the project, and it is possible to reduce the power consumption by more than 50 % by using the small micro-hotplates as shown in chapter 3.

Finally, two issues of the proposed technique are pointed out. First of all, it is not always easy to identify the components of a mixture practically. This is because all the transient curves of the components are monotonously increasing (or decreasing). Secondly, the technique requires the signal in the dry air as the baseline. Since the baseline resistance is not guaranteed to be stable, it is needed to measure the zero gas transient on a regular basis. An improved technique to obviate these two issues is proposed in chapter 6.

References

[5.1] L. Pauling, "The Nature of the Chemical Bond", 3rd ed., Cornell Univ. Press, 1960.

[5.2] N.C. Das, T.K. Chaki, D. Khastgir, "Effect of processing parameters, applied pressure and temperature on the electrical resistivity of rubber-based conductive composites", Carbon 40, pp. 807-816, 2002.

[5.3] D.R. Lide, "Handbook of Chemistry & Physics 87th Edition 2006-2007", CRC, 2006.

[5.4] Y.S. Kim and Y.S. Yang, "Additional thermodynamic feature extraction from chemoresistive carbon black-polymer composite sensors by temperature modulation", Sensors and Actuators B, 121, pp. 507-514, 2007.

[5.5] E. Llobet, R. Ionescu, S. Al-Khalifa, J. Brezmes, X. Vilanova, X. Correig, N. Bârsan, "Multicomponent gas mixture analysis using a single tin oxide sensor and dynamic pattern recognition", IEEE Sensors Journal, Vol. 1, No. 3, pp. 207-213, 2001.

[5.6] A. Pike and J.W. Gardner, "Thermal modelling and characterisation of micropower chemoresistive silicon sensors", Sensors and Actuators B, 45, pp. 19-26, 1997.

CHAPTER 6

Zero-gas free signal processing technique for low-cost environmental applications

6.1 Introduction

In chapter 5, the novel temperature modulation technique proposed in chapter 4 was applied successfully to the detection of single vapours in air. However, the technique was found to have some significant drawbacks when applied to carbon black/polymer composite sensors:

1. It was not easy to identify the components when mixed, as the curves used are always monotonously increasing (or decreasing). This restricts its application to identifying individual vapours in air and not mixtures.
2. The technique requires the measurement of the transient conductance of air (zero gas). This means that it is necessary to measure the zero gas transients on a regular basis and ideally before each measurement of a vapour – adding complexity and costs to an instrument. Secondly, the sensor cannot be used easily in environments where there is no zero gas (unless a bottle is included within the unit). This limits the practical application of the sensor.

In this chapter, an improved technique is proposed that negates these two limitations and thus significantly enhances the use of thermally-modulated polymer composite based sensors.

6.2 Improved signal processing technique

The novel technique proposed in this chapter uses both the off and on transient, unlike the previous technique described in chapters 4 and 5. First, the technique is explained conceptually, then it is expressed mathematically and finally simulations are presented.

The conceptual explanation of the proposed technique is depicted in figure 6.1. Here, rectangular temperature modulation occurs between two temperatures T_1 and T_2 ($T_1 < T_2$) in the presence of the vapour. Figures 6.1 (a) and (b) are the conductances of the sensor during the off and on transients. They are aligned so that their temperature changes occur at the same time for the purpose of the following discussion. Furthermore, the thermal response time of the micro-hotplate is smaller than the thermal time constant of the diffusion effect as shown in chapter 5. The diffusion constants of off-transients are smaller than those of on-transients because the temperature is lower. Here, $G_{1,\infty}$ and $G_{2,\infty}$ are the steady state conductance at temperatures T_1 and T_2 of the vapour, respectively.

Next, by simply adding the curves in figures 6.1 (a) and (b), we find the curve shown in figure 6.1 (c). A peak is formed as a consequence of the difference in the diffusion constants for the off and on transients. Although, the steady state conductance $G_{1,\infty}$ and $G_{2,\infty}$ are the values in a vapour ambient, they will be affected by the baseline drift described in the previous chapter. However, it is always possible to find these values by waiting long enough for diffusion phenomenon to equilibrate. Then, by subtracting the curve in figure 6.1 (c) by ($G_{1,\infty}$+ $G_{2,\infty}$), we obtain the curve shown in figure 6.1(d).

The following predictions about the characteristics of the resultant curve are made:

a. The time of the peak depends only on the diffusion coefficient at T_1 and T_2 (independent of the vapour concentration) and thus is specific to vapour type.
b. The height of the peak is linearly proportional to the vapour concentration since the amplitudes of both the off and on transients are proportional to the vapour concentration.
c. The curve for a mixture will simply be the superposition of each vapour assuming that the species are independent of each other. (Small interactions could be modelled by extension to a perturbation or non-linear model)

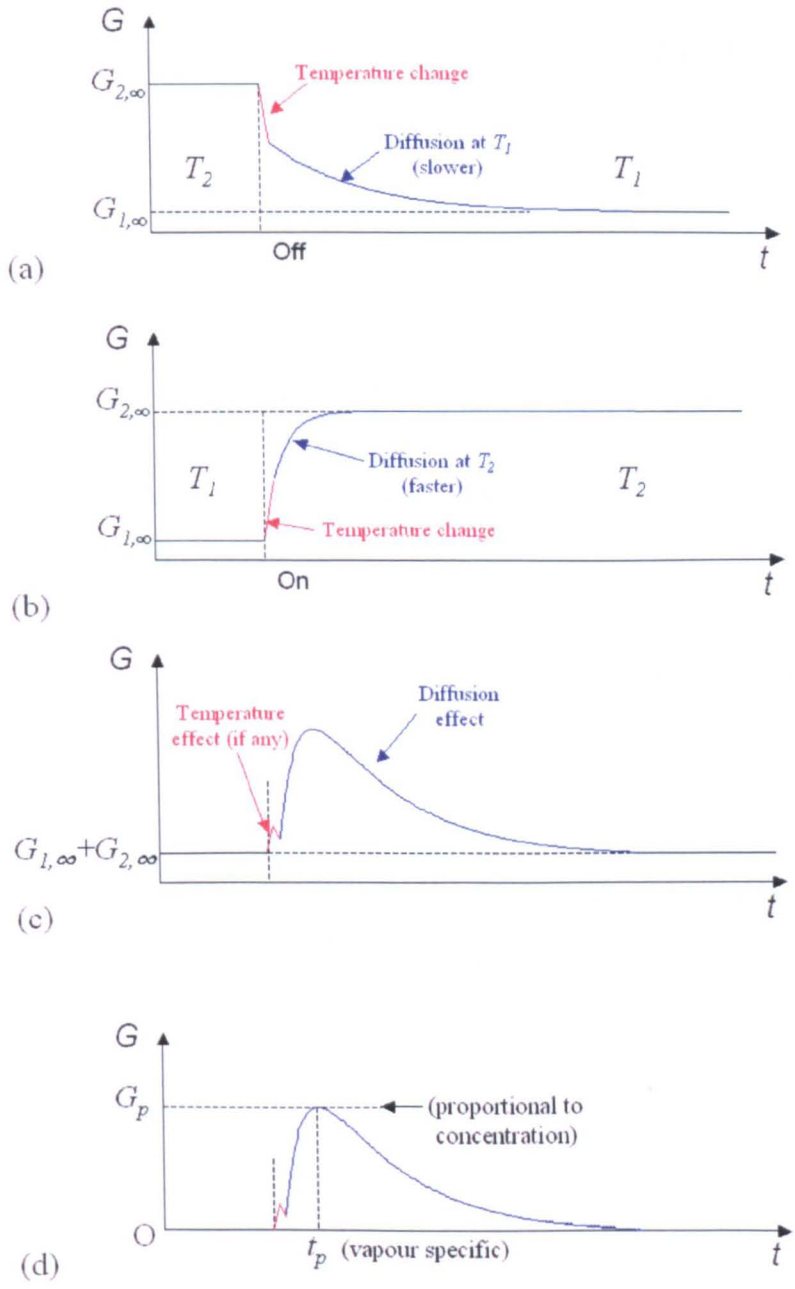

Figure 6.1. (a) Sensor conductance for off transient, (b) sensor conductance for on transient, (c) sum of off and on transient, (d) final curve for identification and quantification (G: conductance, t: time).

To verify the predictions of a and b, a rigorous mathematical discussion is now given (Note: Prediction c is not proven mathematically, but is shown to be true experimentally. The assumption for the prediction c is needed for Fick's equation). The fractional difference of the off and on transient conductances can be written by:

(off-transient)

$$G_{T1}(t) = G_{T1,dry}(t)\left[1 - Nc_{vapour}\left[K(T_1) - \frac{8}{\pi^2}\{K(T_1) - K(T_2)\}\cdot \sum_{m=1}^{\infty}\left[\frac{1}{2m-1}exp\left(-\frac{\pi(2m-1)^2 D_{T1}}{4h^2}t\right)\right]\right]\right] \tag{6.1}$$

(on-transient)

$$G_{T2}(t) = G_{T2,dry}(t)\left[1 - Nc_{vapour}\left[K(T_2) - \frac{8}{\pi^2}\{K(T_2) - K(T_1)\}\cdot \sum_{m=1}^{\infty}\left[\frac{1}{2m-1}exp\left(-\frac{\pi(2m-1)^2 D_{T2}}{4h^2}t\right)\right]\right]\right] \tag{6.2}$$

These equations can be obtained from equations (4.12) and (4.7). Simply summing equations (6.1) and (6.2) gives

$$\begin{aligned} G_s(t) &= G_{T1}(t) + G_{T2}(t) \\ &= \left[G_{T1,dry}(t)\{1 - Nc_{vapour}K(T_1)\} + G_{T2,dry}(t)\{1 - Nc_{vapour}K(T_2)\}\right] \\ &+ G_{T1,dry}(t)Nc_{vapour}\frac{8}{\pi^2}\{K(T_1) - K(T_2)\} \\ &\cdot \sum_{m=1}^{\infty}\left[\frac{1}{2m-1}\exp\left(-\frac{\pi(2m-1)^2 D_{T1}}{4h^2}t\right)\right] \\ &- G_{T2,dry}(t)Nc_{vapour}\frac{8}{\pi^2}\{K(T_1) - K(T_2)\} \\ &\cdot \sum_{m=1}^{\infty}\left[\frac{1}{2m-1}\exp\left(-\frac{\pi(2m-1)^2 D_{T2}}{4h^2}t\right)\right] \end{aligned} \tag{6.3}$$

The equation converges to the following value at the limit when t tends to infinity, *i.e.* t is much greater than the time constant:

$$G_s(\infty) = G_{T1,dry}(\infty)\{1 - Nc_{vapour}K(T_1)\} + G_{T2,dry}(\infty)\{1 - Nc_{vapour}K(T_2)\} \tag{6.4}$$

Since the thermal time constant of the micro-hotplate is much smaller than those of vapour molecule diffusion, the first and second term of the right hand side of equation (6.3) converges much faster than the third term. Therefore,

$$G_s(t)-G_s(\infty)=Bc_{vapour}\left[G_{T1,dry}(\infty)\cdot\sum_{m=1}^{\infty}\left[\frac{1}{2m-1}exp\left(-\frac{\pi(2m-1)^2 D_{T1}}{4h^2}t\right)\right]\right.$$
$$\left.-G_{T2,dry}(\infty)\cdot\sum_{m=1}^{\infty}\left[\frac{1}{2m-1}exp\left(-\frac{\pi(2m-1)^2 D_{T2}}{4h^2}t\right)\right]\right] \quad (t>>t_m) \qquad (6.5a)$$

$$B\equiv N\frac{8}{\pi^2}\{K(T_1)-K(T_2)\} \qquad (6.5b)$$

where t_m is the response time of the micro-hotplate, and B is a constant. Equation (6.5) corresponds to the curve in figure 6.1 (d).

The equation (6.5) clearly shows that its shape depends only on the diffusion coefficients (apart from parameters that are specific to the sensor *i.e.* h, $G_{T1,dry}(\infty)$ and $G_{T2,dry}(\infty)$) and thus proves prediction a. The amplitude is proportional to the concentration of the vapour and so proves prediction b.

Later in this chapter, ($G_s(t)$ - $G_s(\infty)$) is simply referred to as the "response", and the term "fractional response" denotes a response divided by (G_1 + G_2), which is used when comparing the responses of two sensors with different conductivities.

The response of equation (6.5) was plotted in figure 6.2. Here, the temperature dependence of the diffusion coefficient is assumed to be Arrhenius type (Note: This was shown to be correct for methanol vapour in chapter 5):

$$\frac{D(T)}{D(25^oC)}=exp\left[-\frac{E_a}{k_B}\left(\frac{1}{T+273.15}-\frac{1}{25+273.15}\right)\right] \qquad (6.6)$$

where E_a is the activation energy, T is the temperature in Kelvin, and k_B is the Boltzmann constant. The curves for h = 1 [μm], $D(25\ ^oC)$ = 1 × 10^{-7}, 1 × 10^{-8}, 1 × 10^{-9} [cm^2/s] and E_a = 0.40 [eV] (Measured value for methanol. See chapter 5) when temperature modulated between 25 °C and 55 °C, is calculated and plotted in figure 6.2.

It demonstrates that species with different diffusion coefficients can be separated by the time of their peaks.

Next, the dependence of temperature modulation amplitude is studied. The temperature dependence of the partition coefficient is assumed to be described by the following equation (Note: This was again shown to be correct for methanol in chapter 5):

$$\frac{K(T)}{K(25^{o}C)} = exp\left[-\frac{\Delta H_0}{R}\left(\frac{1}{T+273.15}-\frac{1}{25+273.15}\right)\right] \tag{6.7}$$

where ΔH_0 is the standard enthalpy change for the interaction between the polymer and the vapour molecule, and R the gas constant. The curves for h = 1 [μm], ΔH_0 = - 27.5 [kJ/mol] (Measured value for methanol vapour. See chapter 5) with the temperature modulations of 25 °C ↔ 55 °C, 35 °C ↔ 55 °C and 45 °C ↔ 55 °C are calculated and plotted in figure 6.3 (a). Relative values (the values for the temperature modulation of 25 °C ↔ 55 °C is defined as unity) of the height of the peaks and FWHMs (full width at half maximum) are plotted in figure 6.3 (b), indicating the greater the temperature modulation amplitude, the higher and narrower the peak. Therefore, it is predicted that the larger temperature amplitude is preferred for this improved technique.

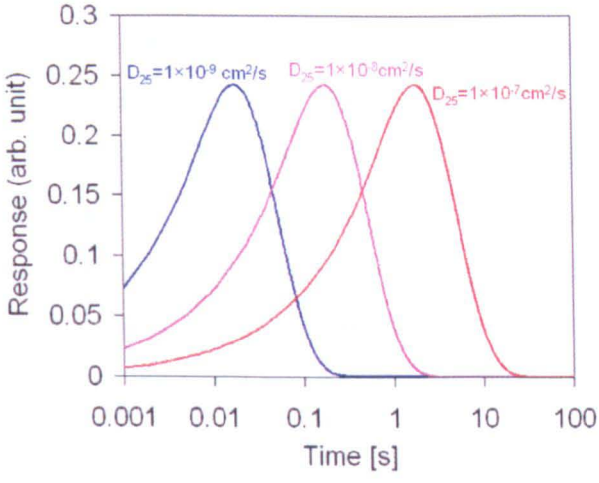

Figure 6.2. Simulated response using the improved signal processing technique for different diffusion coefficients.

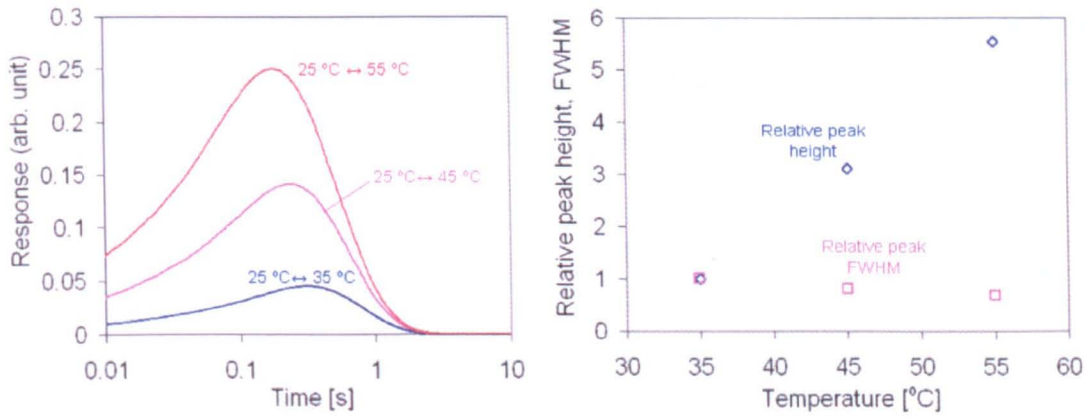

Figure 6.3. (a) Simulated temperature dependence of the response of the new processing technique. (b) Simulated relative peak height and FWHM of the response.

6.3 Experiments and signal processing

In this section, the improved processing technique proposed in the previous section is applied to either experimental data described in chapter 5 or new data, and discussed in terms of (a) temperature dependence, (b) vapour type and concentration dependence, (c) thickness dependence, (d) mixture effect, and (e) number of averaging. The results of the data analysis are given below.

(a) Temperature dependence

First of all, the results for methanol vapours with various temperature modulation amplitudes (25 °C↔55 °C, 35 °C↔55 °C, 45 °C↔55 °C) taken in chapter 5 were processed. The sensor used is PVP11 and the frequency of the square wave is 50 mHz.

Figure 6.4 (a) shows the processed data. The curves shown are generated by averaging 6 transients. The curves and their temperature dependence are similar to the simulation results (figure 6.3 (a)). In fact, the measured temperature dependence of the relative height and FWHM of the peaks are very close to those of simulations as shown in figure 6.4 (b) (Note: The simulation uses the experimental values of methanol to describe the temperature dependence, and thus can be compared with the experiments), indicating that the theory is valid.

The shapes of the curves are different from the simulations at the left hand side tail region. This is because the sampling period of each curve is 10 ms and thus those left hand side tail regions were not measured accurately.

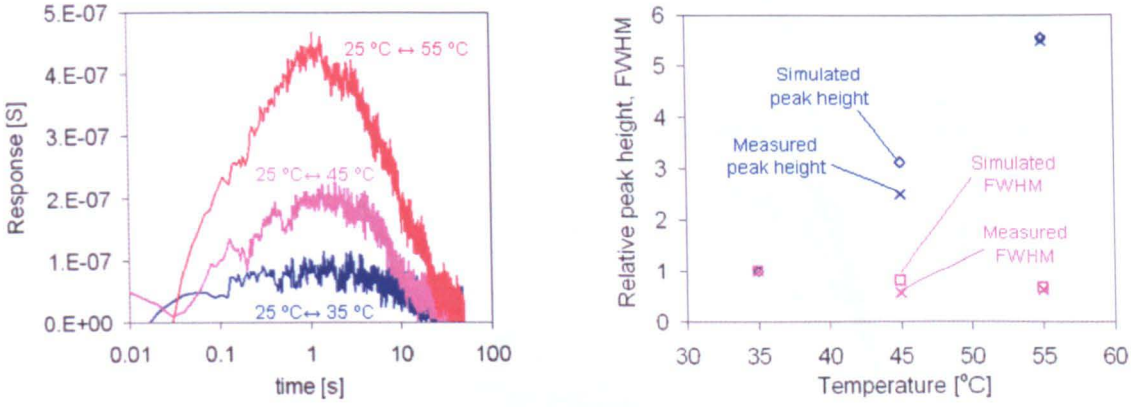

(a) (b)

Figure 6.4. (a) Characteristic behaviour in methanol for different temperature modulation amplitudes. (b) Measured relative peak height and FWHM of the response in methanol vapour with different temperature modulation amplitudes as compared with simulations.

(b) Vapour type and concentration dependence

Temperature modulation (between 25 °C and 55 °C) experiments of the device PVP11 were performed in the presence of single vapours (water, methanol and ethanol) and the results processed using the new technique. The frequency of the square wave is 50 mHz for water and methanol and 1.67 mHz for ethanol.

The results are shown in figure 6.5. The curves for water and methanol vapour are averages of 30 transients and that for ethanol vapour are an average of 3 transients. As predicted, each vapour is separated out clearly using the difference of their peaks in time (water: 50 ms, methanol: 1 s, ethanol 30 s). This is a reasonable result indicating that the species with higher molecular mass has the higher diffusion coefficients (molecular mass of water, methanol and ethanol are 18, 32 and 46, respectively [6.1]). The height of the peaks, shown in figure 6.5, increases when the vapour concentration increases - as the theory predicts. Figure 6.6 plots response vs concentrations of all the vapours (water, methanol and ethanol) in figure 6.5, and shows that the responses are linearly proportional to the concentrations, again as the theory predicts.

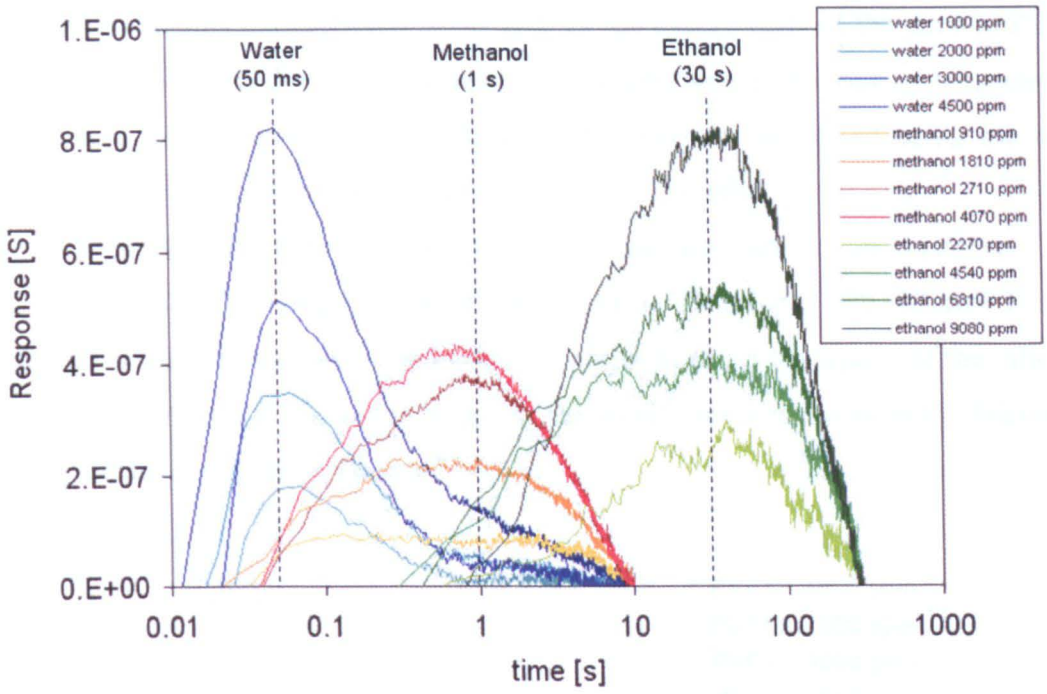

Figure 6.5. Responses in water, methanol and ethanol vapours of various concentrations.

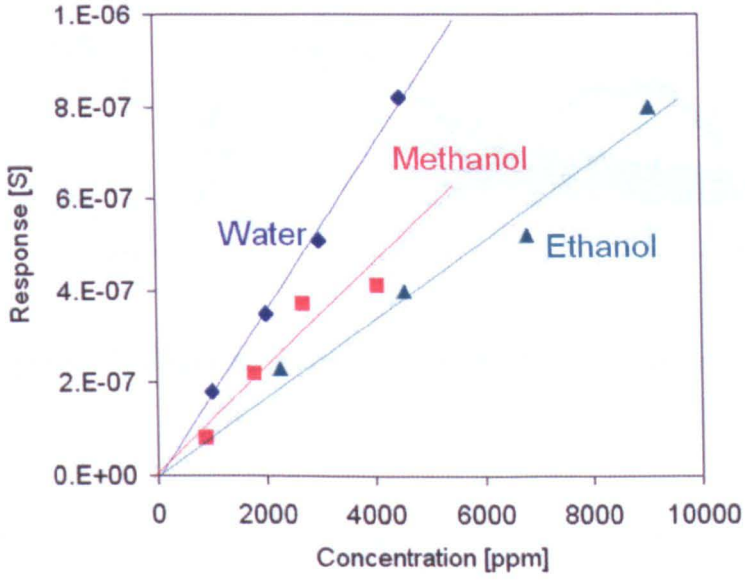

Figure 6.6. Concentration dependence of responses in water, methanol and ethanol vapours.

(c) Thickness dependence

Temperature modulation (between 25 °C and 35 °C) experiments of the devices PVP8 (thickness: *ca* 6 μm) and PVP11 (thickness: *ca* 0.8 μm) were performed in the presence of various concentrations of water vapour and the results processed using the new technique. The frequency of the square wave used was 10 mHz.

Figure 6.7 shows the results. The curves are averages of 30 transients. The thicker film has a 60 times greater peak time (3 s) than the thinner film (50 ms). This is a reasonable value as the peak time should be proportional to the square of the ratio of thickness (*i.e.* $(6/0.8)^2 = 56$) and considering the significant uncertainty in the thickness measurements (described in chapter 5).

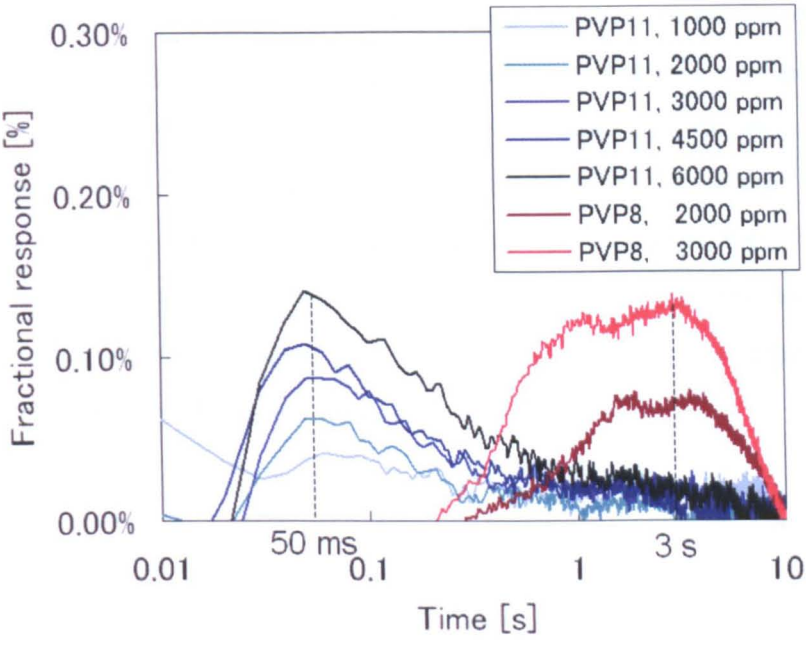

Figure 6.7. Thickness dependence of the fractional response.

(c) Mixture effect

Temperature modulation (between 25 °C and 55 °C) experiments of mixtures (water and methanol) were performed and the results were processed using this new technique. The device used was PVP11 and the frequency of the square wave was 50 mHz.

The results are shown in figures 6.8, 6.9 and 6.10. Each curve is the average of 30 transients. Results correspond to water and methanol concentrations of (1000 ppm, 910 ppm), (1000 ppm, 1810 ppm), (1000 ppm, 2710 ppm), (2000 ppm, 910 ppm), (2000 ppm, 1810 ppm), (2000 ppm, 2710 ppm), (3000 ppm, 910 ppm), (3000 ppm,

1810 ppm) and (3000 ppm, 2710 ppm), respectively. These figures show both the resultant curves of mixtures but also single vapour curves of water and methanol with the corresponding concentrations. The single vapour results were superimposed to predict the curve for the mixtures and plotted as "prediction". It was found that the resultant curves of mixtures are similar to the predicted curves, though there is a tendency that the predicted curves are higher than the experimental ones. The precise cause of this tendency is not known and may be error in experiments. Further tests are needed to confirm the reproducibility.

Quantification of each vapour (water and methanol) was also carried out using the results shown in figures 6.8, 6.9 and 6.10. The concentration of a species in a mixture is calculated by simply subtracting the value of the peak at the time of the species by the sum of the values of the other species at the same point. For example, the concentration of the water in a mixture is calculated by subtracting a value of mixture by that of methanol at 50 ms as shown in figure 6.11. Figure 6.12 (a) shows the results of quantification of water in mixtures with ethanol and figure 6.12 (b) vice versa. It was shown that for both water and methanol can be quantified. However, there is some error especially in methanol vapour quantification: higher water vapour concentration causes the decrease in the detected methanol response. This could be error in experiments, but a more likely possibility is discussed in the next section.

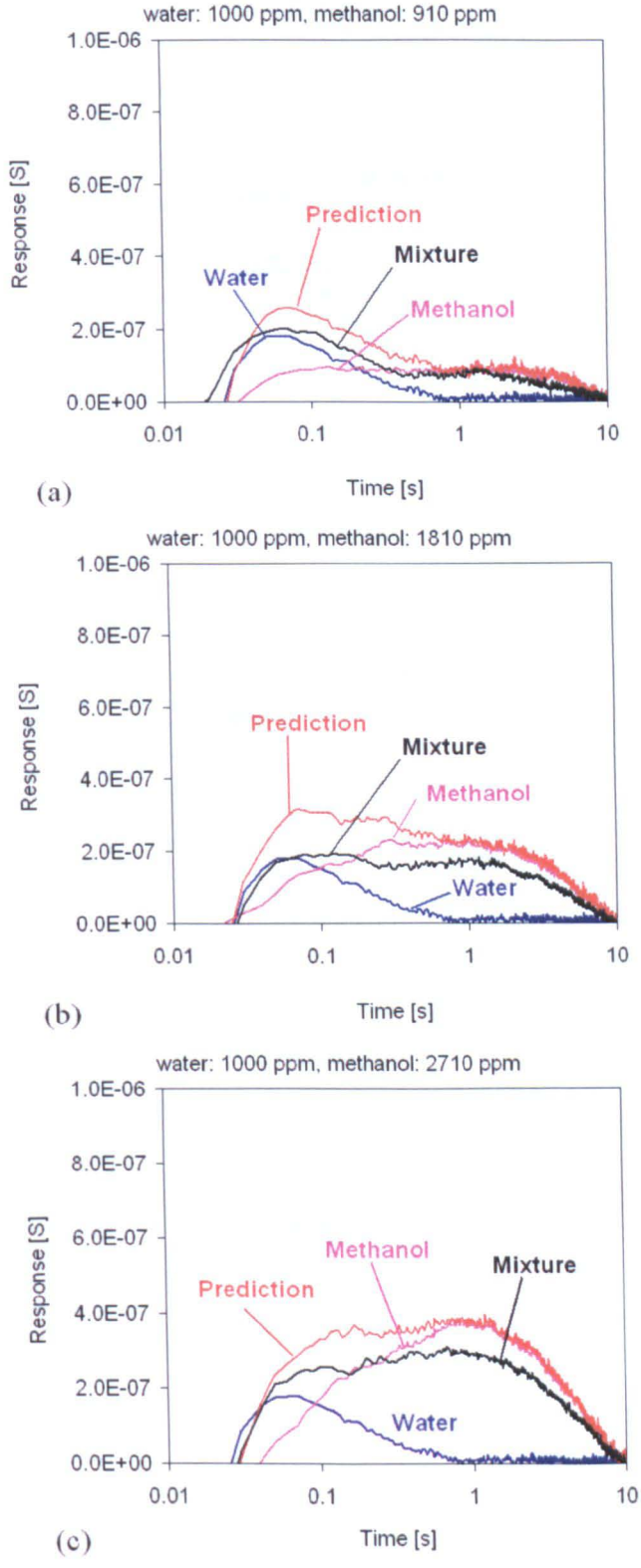

Figure 6.8. Results for mixtures of water concentration of 1000 ppm and methanol concentration of (a) 910 ppm, (b) 1810 ppm, (c) 2710 ppm.

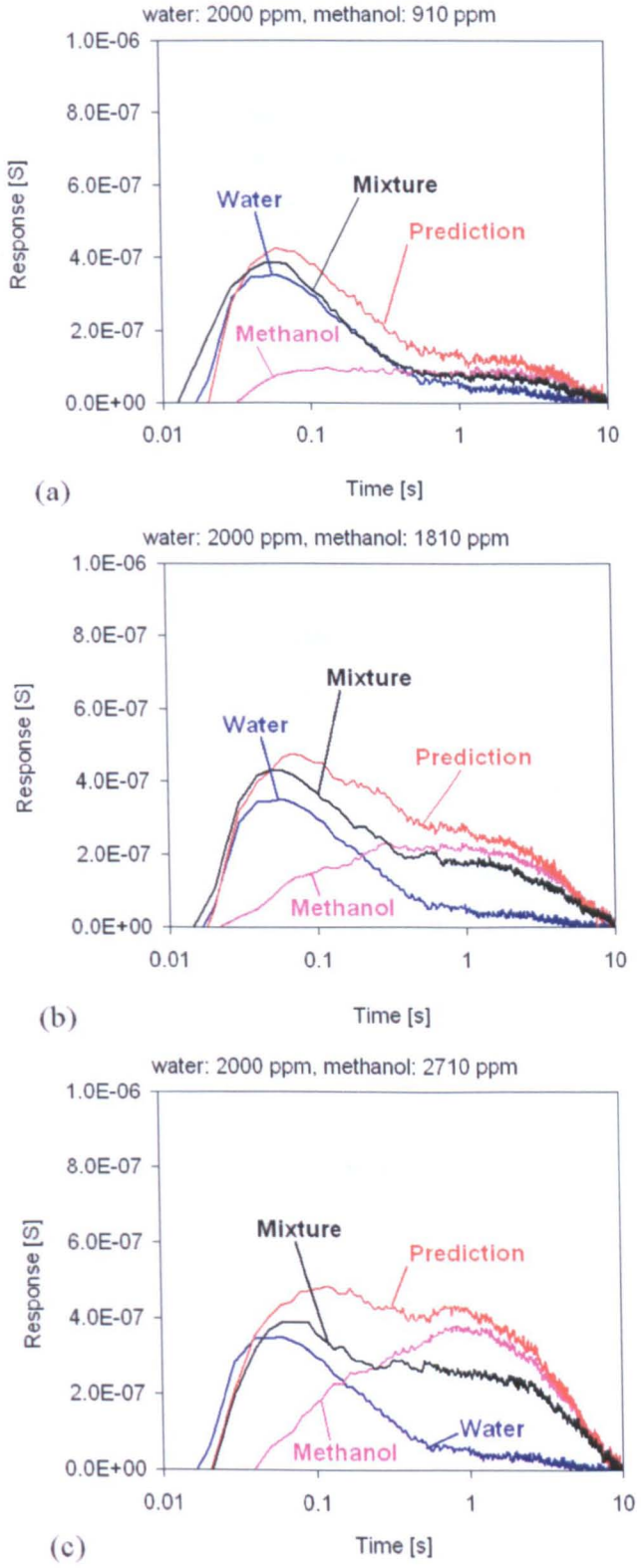

Figure 6.9. Results for mixtures of water concentration of 2000 ppm and methanol concentration of (a) 910 ppm, (b) 1810 ppm, (c) 2710 ppm.

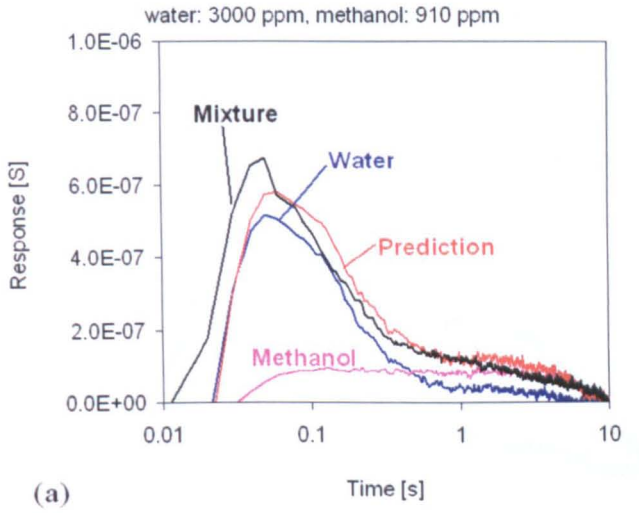

(a)

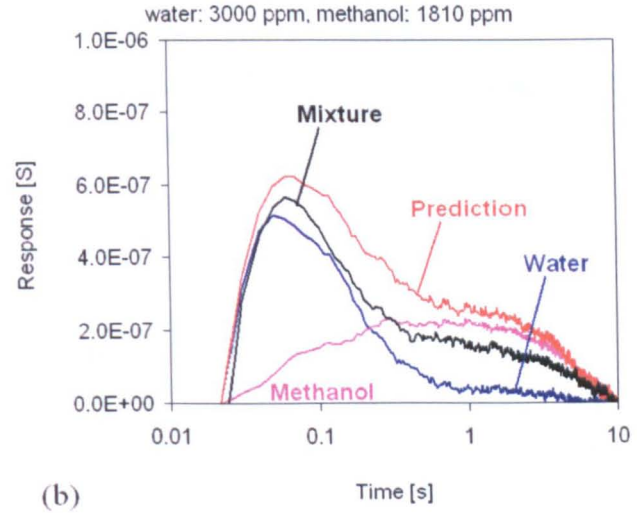

(b)

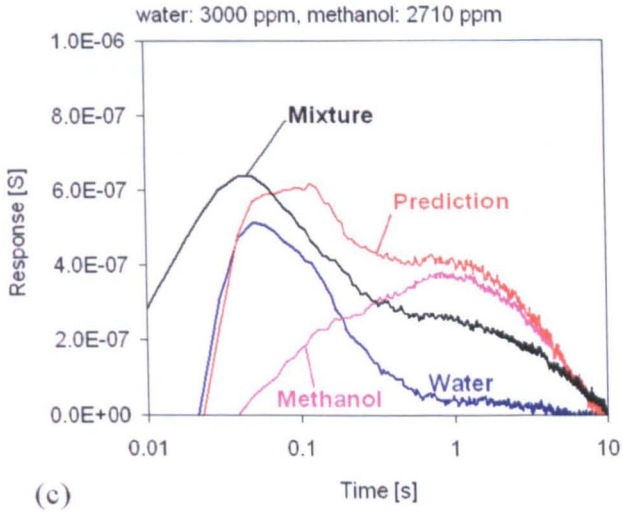

(c)

Figure 6.10. Results for mixtures of water concentration of 3000 ppm and methanol concentration of (a) 910 ppm, (b) 1810 ppm, (c) 2710 ppm.

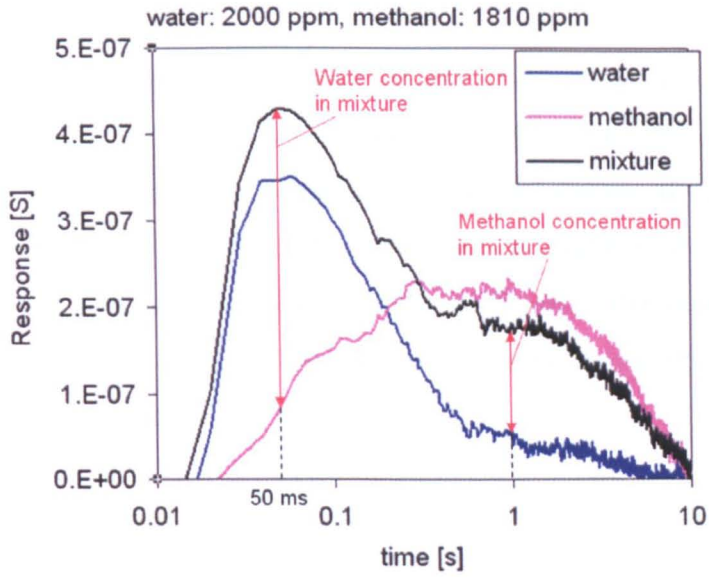

Figure 6.11. Calculation of the concentration of each vapour in a mixture.

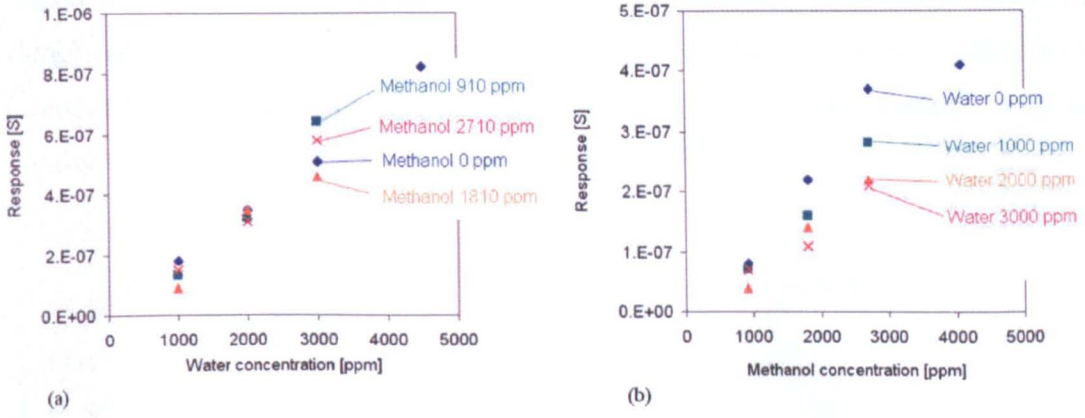

Figure 6.12. (a) Results for water vapour sensing in different concentration of methanol vapour. (b) Results for methanol vapour sensing in different concentration of water vapour.

(d) Number of averaging

To discuss the lower detection limit of the sensor, the number of averaging needed to reduce the noise level to less than 5 % was investigated. The temperature modulation (between 25 °C and 55 °C) results of the device PVP11 in the presence of 3000 ppm of water were used for this purpose. Figures 6.13 (a) and (b) show the response of (a) after

averaging 30 raw data (thus the same curve as the one in figure 6.5), and (b) the 30 raw data.

The standard deviation (or the mean squared error) of the curves in figure 6.13 (b) at 50 ms (peak time for water) is calculated to be 5.3×10^{-8} [S] or 10.4 % of the peak height. The noise is known to be proportional to the inverse of the square root of the number of samples averaged [6.2]. Therefore, the number of averaged curves needed to reduce the error to be less than 5 % for 3000 ppm water vapour is calculated to be $(10.4\ \% / 5\ \%)^2 = 4.3$. Since the concentration is linearly proportional to the signal, the following equation is found:

$$n_{5\%} = \frac{3.9 \times 10^7}{c_{water}^2} \tag{6.8}$$

where $n_{5\%}$ is the number of curves needed to reduce the measurement error to 5 % and C_{water} is the water concentration. Equation (6.8) is plotted in figure 6.14. It is needed to average more than 1000 curves to detect 100 ppm. It is believed that the number could be reduced significantly by, for example, integrating the detection circuitry with the micro-hotplate and amplifying the signal on chip.

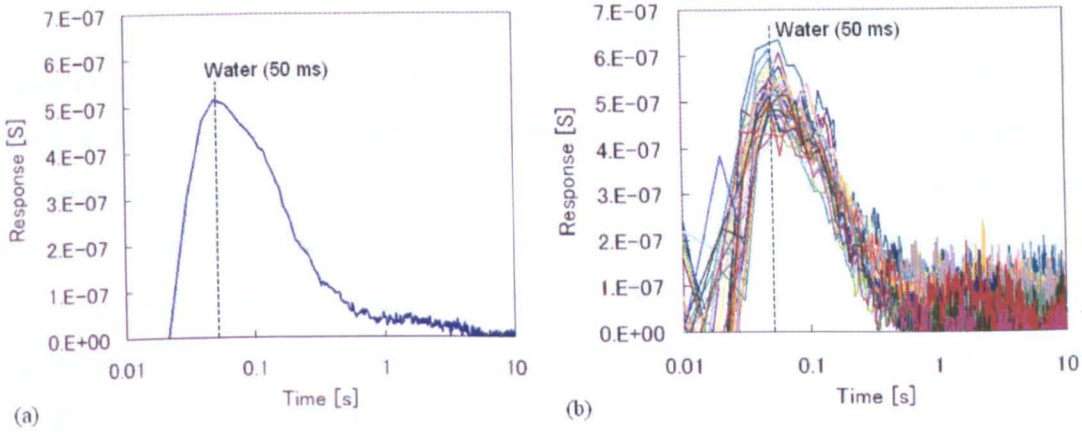

Figure 6.13. Response to 3000 ppm water (a) after averaging 30 raw data and (b) 30 raw data.

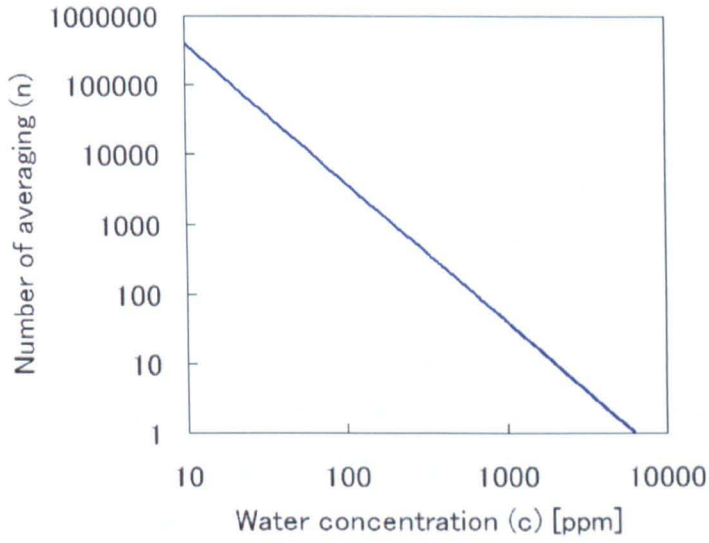

Figure 6.14. Number of averaging needed to reduce the noise level to less than 5 %.

6.4 Discussions

The technique proposed in this chapter has been expressed mathematically and predicts that the response is (a) linearly proportional to the vapour concentration, and (b) superposition of responses for each vapour in a mixture is possible. These characteristics make vapour/gas detection in a mixture relatively straightforward. The advantage of (b) superposition is particularly attractive. Suppose a vapour/gas sensor is sensitive to 5 different vapours/gases. Unless superposition is possible, it is needed to pre-calibrate the sensor response to all the possible combination of concentrations. For example, assuming that 5 different concentrations are needed for one vapour/gas, $5^5 = 3125$ pre-measurements (covering all the possible combinations) have to be carried out. However, if superposition is possible, only $5 \times 5 = 25$ pre-measurements (for single vapour/gases) are sufficient, as the response to mixtures can easily be predicted by superposition. Since none of the temperature modulation techniques for metal oxide sensors published previously allow superposition [6.3-6.5], it is believed that the proposed technique is, as long as it works according to the theory, superior. In addition, it has to be noted that this technique does not rely on any chemical reactions but relies only on physical mechanisms of diffusion and swelling, and thus may offer better reliability.

The linearity of the proposed technique was experimentally shown (figure 6.6) at the concentration range used. These results also agree with Lewis's work, which claims the linearity of the steady state response of this type of sensors (e.g. [6.6]).

However, the superposition was not clearly shown to be possible. Although this may be due to the error in experiments, the following discussion is given assuming that the results shown in figure 6.12 indicate that a linear superposition is problematic. One possible explanation of this is that the second solvent (e.g. methanol) is enhancing the diffusion of the first solvent (e.g. water) as published in [6.7]. It is believed that there is a way to obviate this issue. This is because the vapour molecules should not affect each other as long as their concentrations are dilute. There are ways to reduce the concentrations in the polymers at the expense of sensitivity:

1. Increasing the temperature (e.g. From 25 °C↔55 °C to 35 °C↔65 °C)
2. Using less sensitive polymers (PVP was chosen as it has the highest concentration to methanol in [6.8]. By choosing e.g. poly(styrene), the sensitivity decreases by the factor of 0.05, thus will be more probable to be additive)

However many practical applications involve the detection of lower concentrations of the vapours than tested here and so that would mean the system would be naturally more linear.

The additive behaviour of steady state response of carbon black/poly(ethylene-co-vinyl acetate) to benzene and heptane at low concentration ($0.005 < P/P_0 < 0.015$, where P_0 is the vapour pressure of the analyte) supports this idea [6.6].

It should be stated that the response time is relatively slow. For example, the peak for ethanol is at 30 sec and it was necessary to wait until 300 sec to form the peak. However, the response time of this sensor is strongly dependent on the thickness of the film (*i.e.* proportional to the square of the thickness) because the phenomenon is governed by the diffusion effect. Therefore, response time (*i.e.* time needed to form the peak) can be decreased to say 3 seconds by using a film with 10 % thickness.

6.5 Conclusions

In this chapter, a novel signal processing technique for a carbon black/polymer composite sensor is proposed, modelled, and applied to the experimental data presented in chapter 5. The technique is very simple, namely summing the off and on transient conductances and subtracting the steady-state value from the curve. It was theoretically predicted that the peak time is specific to the type of vapour and that the height of the peak of the resultant curve is linearly proportional to the vapour concentration. Therefore vapours can be both identified and concentration predicted. It was also predicted that the resultant curve for a mixture was a superposition of its constituents. Since the resultant curve of this improved technique has peaks unlike the previous one and does not rely on zero-gas baseline values, this technique should have more widespread application and at lower cost.

The experimental results taken in chapter 6 were processed using the new technique with the following observations:

1. The larger temperature modulation amplitude makes the peak height larger and FWHM narrower for methanol vapour. Therefore higher temperature modulation amplitude is more desirable.
2. Water, methanol and ethanol vapours have their specific peak time *i.e.* 50 ms, 1 s and 30 s, respectively, for the 0.8 μm thick PVP film, and thus can be separated out easily.
3. The response is linearly proportional to the vapour concentration for water, methanol and ethanol in the concentration range tested (water: 1000-4500 ppm, methanol: 910-4070 ppm, ethanol: 2270-9080 ppm).
4. The thicker film has greater peak time (proportional to the square of the thickness) for water.

Therefore, it has been concluded that this technique can identify and quantify single vapours easily. This means this technique is superior to other temperature modulation techniques reported elsewhere for metal oxide based sensors.

The technique was also applied to mixtures of water and methanol with various concentrations. The results appear to be additive, but more experimental work is needed to verify this statement.

References

[6.1] D.R. Lide, "Handbook of Chemistry & Physics 87th Edition 2006-2007", CRC, 2006.

[6.2] J.R. Taylor, "An introduction to error analysis : the study of uncertainties in physical measurements", Sausalito : University Science Books, 1997.

[6.3] A. Heilig, N. Bârsan, U. Weimar, M. Schweizer-Berberich, J.W. Gardner and W. Göpel, "Gas identification by modulating temperatures of SnO_2-based thick film sensors", Sensors and Actuators B 43, 1997, pp. 45-51.

[6.4] E. Llobet, R. Ionescu, S. Al-Khalifa, J. Brezmes, X. Vilanova, X. Correig, N. Bârsan and J.W. Gardner, "Multicomponent gas mixture analysis using a single tin oxide sensor and dynamic pattern recognition", IEEE Sensors Journal, Vol.1, No. 3, 2001, pp. 207-212.

[6.5] E. Llobet, J. Brezmes, R. Ionescu, X. Vilanova, S. Al-Khalifa, J.W. Gardner, N. Bârsan, X. Correig, "Wavelet transform and fuzzy ARTMAP-based pattern recognition for fast gas identification using a micro-hotplate gas sensor", Sensors and Actuators B 83, 2002, pp. 238-244.

[6.6] E.J. Severin, B.J. Doleman and N.S. Lewis, "An investigation of the concentration dependence and response to analyte mixtures of carbon black/insulating organic polymer composite vapour detectors", Analytical Chemistry, 72, 2000, pp. 658-668.

[6.7] J.S. Vrentas, J.L. Duda and H.-C. Ling, "Enhancement of impurity removal from polymer films", Journal of Applied Polymer Science, 30, 1985, pp. 4499-4516.

[6.8] M.C. Lonergan, E.J. Severin, B.J. Doleman, S.A. Beaber, R.H. Grubbs, and N.S. Lewis, "Array-based vapor sensing using chemically sensitive, carbon black-polymer resistors", Chemistry of Materials, 8, 1996, pp. 2298-2312.

CHAPTER 7

Conclusions and further work

7.1 Overview

The aim of this project was "to develop a novel gas sensor with low cost, low power consumption, high reliability, which can detect multiple gases with excellent selectivity" for indoor gas monitoring. To achieve this aim, the project has been split into two parts: the development of a novel ultra-low power CMOS compatible micro-hotplate, and the development of a novel temperature modulated carbon black/polymer composite sensor capable of detecting several different vapours.

For the most part, the aim has been achieved. An SOI-CMOS compatible micro-hotplate with single crystal silicon resistive heater was proposed, designed, fabricated, and its ultra low power consumption and excellent stability demonstrated. Then a novel temperature modulation technique was applied to a chemoresistor formed by depositing carbon black/polymer composite film onto the fabricated micro-hotplate. Identification and quantification of water, methanol and ethanol vapours were successfully demonstrated using the single low power, low cost micro-chemoresistor.

7.2 Conclusions

7.2.1 Conclusions for micro-hotplate development

In the first part of the thesis (chapters 2 and 3), a novel design of micro-hotplate was proposed, designed, fabricated and characterised. The proposed design was aimed

towards low cost, low power consumption and better reliability than previously reported ones.

The resistive heater material and the type of the starting wafer were strategically chosen to be "single crystal silicon" and "SOI". The choice was made aiming at creating devices with low-cost and improved reliability.

First of all, single crystal silicon was chosen as a resistive heater material because it is a CMOS (or SOI-CMOS) compatible material and does not have highly reactive grain boundaries. The CMOS compatibility makes integration with associated circuitry possible. This apparently leads to lower cost in volume production because there is no need to build a production line (or even a factory) specific for the micro-hotplates. The integration leads to smaller size or even enhances the performance of the sensor; for example it is very probable that the signal to noise ratio could be increased by amplifying the signal on chip. From these points of view, the material is much superior to the traditional heater material, platinum, which is not CMOS compatible. Single crystal silicon should be superior to another traditional heater material, polysilicon. This is because the material does not have any grain boundaries or dangling bonds, which was the cause of the resistance drift of polysilicon (More specifically, the gradual breaking of weak Si-H bond at high temperature is the cause of the resistance increase [7.1]).

There have been several studies on micro-hotplates with highly boron doped single crystal silicon resistive heaters (*e.g.* [7.2]). However, the heaters were not passivated due to their fabrication process using ordinary silicon wafer and its wet etching using KOH or TMAH, and thus can easily be damaged during operation. Therefore, it has been decided to use an SOI wafer (thus SOI-CMOS process) rather than ordinary silicon wafer (CMOS process) to ensure the reliability of the devices.

The micro-hotplates were then strategically designed to minimise the power consumption in the following three steps. First of all, it was decided to use a metal as a resistive track material to supply electric current, rather than make both heater and track using single crystal silicon. Tungsten and aluminium, both of which are CMOS compatible, are used as the metal material (Aluminium is generally preferred to tungsten as long as the operation temperature is close to room temperature. This is because the resistivity of aluminium is much lower than that of tungsten, which makes it possible to reduce the power consumption further and enhance the performance of

circuitry. In addition, aluminium process is generally cheaper than tungsten one. However, aluminium is known to suffer from electro-migration problem especially at high temperatures. Therefore, tungsten is preferred for high temperature applications such as metal oxide chemoresistors). Since metals have much smaller resistances than semiconductors, this will lead to narrower tracks with lower thermal conductance. Secondly, the size of the heater was designed to be much smaller than that of the previously reported ones. By doing this, the convective heat loss, which was traditionally the largest heat dissipation mechanism, was greatly reduced. Thirdly, the membrane to heater ratio was designed to be much larger than the previously reported ones (membrane to heater ratio: 12.5) in order to reduce the conduction heat loss through the membrane. Those designing work was carried out confirming the performance by 2D FEM simulations using COMSOL software.

After those micro-hotplates were designed, the fabrication process was carried out at thee commercial foundries in Europe; XFAB in Germany for SOI-CMOS process, Silex Microsystems in Sweden for DRIE and Pac Tech in Germany for electroless Au/Ni plating.

The proposed fabrication process for the micro-hotplates is not only SOI-CMOS compatible, but makes the best use of it. First of all, the shape of the single crystal silicon resistive heater was defined by the trench etching process, which is used to isolate between MOSFETs. Secondly, the resistive heaters were doped simultaneously with the source and drain of MOSFETs. Therefore, no additional fabrication steps to a commercial SOI-CMOS process were needed to fabricate the novel micro-hotplate structure.

The fabricated devices were found to have both ultra low power consumption and low operating voltages. The values are 9.4 mW, 3.35 V for calorimeter (SRL287e) and 11.6 mW, 3.71 V for chemoresistor (SRL289g), both to operate at 500 °C. The power consumption values are, to the best of my knowledge, the smallest ever reported. It should be worth pointing out that the 2D FEM simulation, much simpler and less time consuming method, has shown good agreement with the experiments.

The long term stability tests of the micro-hotplates were carried out at 350 °C and 500 °C for 500 hours. The reliability of $p+$ resistive heater was much better than that of polysilicon, which was believed to be due to the fact that single crystal silicon

has no grain boundaries. The drift of the $p+$ resistive heater was less than 1 % after 500 hour operation at 500 °C, indicating its excellent reliability.

7.2.2 Conclusions for temperature modulation technique for carbon black/polymer composites

The aim of the second part of the project (chapters 4-6) was to develop a novel temperature modulation technique, which can both identify and quantify the vapours/gases by using a single sensor. Carbon black/polymer composite was chosen as the sensing material. The reason of the choice is that the response of the material is known to be linear to the concentration of vapours/gases and the superposition of the responses from different vapours/gases is possible [7.3]. In addition the material shows good sensitivity at low temperatures (*e.g.* close to room temperature) [7.3], which will lead to much lower power consumption compared with, for example, tin dioxide.

The proposed technique comprises of three steps. First of all, a square wave voltage (and thus temperature) is applied to the micro-hotplate both in dry air and vapour ambient. The sudden change in temperature in the presence of vapour, causes the vapour molecules diffuse out of or into the polymer (depending on the direction of the temperature change). This is because the partition coefficient is dependent on the operating temperature (*i.e.* the logarithm of the partition coefficient is inversely proportional to the temperature) [7.4]. Apparently, this vapour diffusion phenomenon alters the conductance (or resistance) of carbon black/polymer composite film (diffusion effect) on top of the conductance change inherent to the film (temperature effect).

Secondly, the fraction of the transient conductance is calculated by using the signals with and without vapours. This is to negate the temperature effect and to focus on the conductance change from the diffusion effect. The shapes of the resultant curve should depend on the vapour type *i.e.* vapour molecules with higher diffusion coefficient should have lower time constants. The amplitude of it should be proportional to the vapour concentration.

Thirdly, the identification and quantification are performed. For a single vapour simply the shape of the curve can be used for identification. For example, the response time $t_{50\%}$ can be used. After the vapour type is identified, the vapour concentration is calculated from the amplitude of the transient curve. For a mixture, the resultant curve

is the linear combination of the curve for single vapours. Therefore, the resultant curve is first separated into the curves for all the single vapours by a curve fitting based on *e.g.* least squares. Then, each vapour is quantified using the amplitude of each separated curve.

The proposed technique was demonstrated successfully. Carbon black/polyvinylpyrrolidone composite was deposited onto micro-hotpates. The devices were tested to three vapours individually at various concentrations (water: 1000 – 6000 ppm, methanol: 1360-5430 ppm and ethanol: 2270-9080 ppm). By using $t_{50\%}$ as a transient feature, those single vapours were identified and quantified successfully.

However, two issues of the proposed technique were discovered. First, the proposed technique, though should work theoretically, are not very suitable to detect the components from a mixture. This is because the transient curve for single vapour is always monotonously increasing (or decreasing). Secondly, the technique uses a signal with dry air. If the sensor resistance does not drift at all, it is not an issue; zero gas signal, which was measured in the factory and stored in a memory, can be used. However, if the resistance drift is not negligible, the zero gas value has to be measured on a regular basis. This means a bottle of dry air has to be included in the gas sensor unit, which will make the cost higher and the size of the unit much larger.

In chapter 6, however, an improved technique to obviate the above two issues was proposed. The technique consists of the following three steps. First of all, a square wave voltage (and thus temperature) is applied to the micro-hotplate in gas/vapour ambient, and the transient sensor signal is collected (Note: The signal in dry air is not collected). Secondly, the signal of both the off and on transients are added up. Unlike the one in the original technique, the resultant curve has a peak. This is because the off and on transients are monotonously decreasing and increasing respectively with different time constants (the off transient is slower than on transient). Thirdly, the steady state value is subtracted from the curve, negating the drift of the baseline. The theory has been examined rigorously and the following was proved:

1. The time of the peak is specific to a vapour *i.e.* a vapour with larger diffusion coefficient has a shorter time of the peak.
2. The amplitude of the peak is proportional to the vapour concentration.

The improved theory utilizes a curve with a peak rather than a monotonous one and thus should be much easier to apply for a mixture than the original technique. It should also be noted that the theory does not depend on the zero gas value; the baseline and its drift is negated when the steady state value is subtracted.

The improved technique was applied first to single vapours of water, methanol and ethanol with various concentrations (water: 1000-4500 ppm, methanol: 910-4070 ppm and ethanol: 2270-9080 ppm). It has been shown that the resultant curves for water, methanol and ethanol have their specific peak times *i.e.* 50 ms, 1 s and 30 s, independent of concentrations, and the height of the peaks are proportional to the concentrations, both as predicted by the theory. It has also been shown that the peak time is dependent on the thickness of the film (the peak time is proportional to the square of the thickness). This means that the response time can easily be controlled to fit for target vapours. It should be reasonable to assume that the possible minimum thickness is 80 nm, considering that the diameter of the carbon black nanoshperes is typically 50 – 80 nm (Note: Strictly speaking, it is needed to carry out some experiments to find the minimum thickness where the proposed theory can be applied). For example, the minimum peak time of ethanol vapour is estimated to be 0.3 s, which is believed to be short enough for almost any application.

The technique was also applied to a mixture of water and methanol vapour, with promising results. The concentration of water and methanol were quantified even in the presence of one another assuming the superposition. However, further experiments are needed to investigate this in more detail. This is because a presence of a vapour could effect the diffusion of the other in the polymer.

It is believed that this technique is superior to previous ones proposed for metal oxide gas sensors. To the best of our knowledge, no technique which can both identify and quantify various gases with using only a single chemoresistor has ever been published. Furthermore, the proposed technique is attractive as the signal is linearly proportional to the concentration, and the superposition of each vapour in a mixture is possible (though the more experiments are needed to confirm the possibility of the superposition). The labour of the pre-calibration of the sensor will be reduced extremely by assuming the possibility of superposition; pre-calibration of a mixture is not needed but signals from a mixture (whatever the combination is) can be predicted from the pre-calibrated values for single vapours. It should also be noted that this technique requires

only 1.2 mW (to modulate the temperature between 25 °C and 55 °C), whereas metal oxide based sensors require typically 100 mW even with micro-hotplates due to their high operating temperatures (*e.g.* 350 °C).

7.3 Further work

7.3.1 Further work for micro-hotplate development

Although the main aim of the thesis has been achieved, it should be possible to reduce the power consumption and resistance drift of the micro-hotplates even further. Here an improved design from these points of view is proposed.

As mentioned in chapter 2, the main heat dissipation mechanism of the developed micro-hotplate is the one through the membrane (heat conduction). The conduction power loss is inversely proportional to the logarithm of the membrane to heater ratio as shown in chapter 3. Assuming that the thicknesses and thermal conductivities of the films in the membrane are fixed, there are only two ways to reduce the power consumption; (1) increasing the size of the membrane and (2) decreasing the size of the heater (Note: It is possible to decrease the power consumption by decreasing the thicknesses or thermal conductivities of the films used in the membrane. However, it would not reduce the power consumption significantly). Since increasing the size of the membrane will cause some other problems (enlarge the size of the chip, thus increase the cost, and reduce the mechanical stability), the only way is to decrease the size of the heater.

Then it may be possible to improve the reliability by modifying the dopant concentration. Assuming that the mechanism proposed in chapter 3 is correct (*i.e.* multiplication of dislocations caused by plastic deformation), it should be possible to decrease the resistance drift further by decreasing the dopant concentration (Note: Precise cause of the resistance drift of single crystal silicon is not known and further experiments are needed especially to explain the observations 1 and 2 in chapter 3. Thorough analysis of the resistive heaters by analytical instruments (*e.g.* TEM) before and after reliability tests should be carried out). This is because it is known that the dislocation velocity is slower at lower concentration even in *p*-type single crystal silicon [7.5]. Therefore it is proposed to use *p* region rather than *p*+ region as a heater material.

Considering the above discussion, the structure shown in figures 7.1 and 7.2 is proposed. The structure has a ring heater made of *p* region of SOI-CMOS, and the

metal tracks are employed again to minimise the heat loss (as discussed in chapter 2). There are $p+$ region between the tracks and the p region to ensure an ohmic contact. Unlike the designs discussed in chapters 2 and 3, the electric current of this new design flows radially as show in in figure 7.2 (b). This design was introduced because the resistivity of p region is much smaller than that of $p+$ region (less than 1/100) and it was needed to reduce the resistance of the heater. The size of the heater should be minimised to decrease the power loss as long as the design rule of the foundry is satisfied. However, it is difficult to predict whether this small size does not cause any reliability problem or not prior to fabrication. In addition, deposition and patterning of sensing materials onto the small heated area will be challenging. Therefore, this structure is needed to be fabricated and tested.

The author hopes this new design will enhance the commercialisation of micro-hotplate based gas sensors.

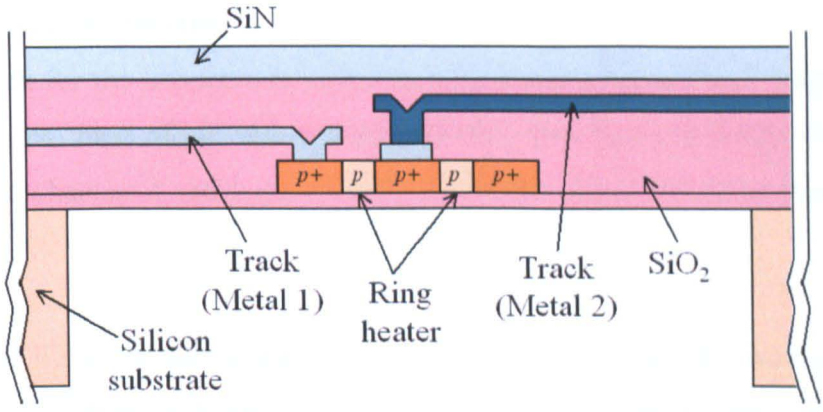

Figure 7.1. Cross section of new SOI-CMOS micro-hotplate design.

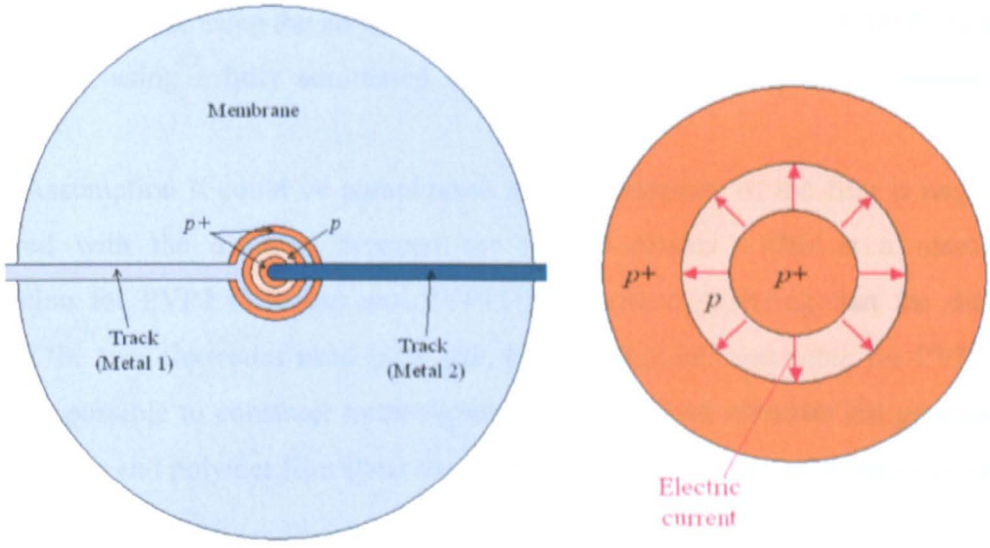

Figure 7.2. (a) Top view of the new SOI-CMOS micro-hotplate design and (b) magnified view of the ring heater (metal tracks not shown).

7.3.2 Further work for temperature modulation technique for carbon black/polymer composites

Further work for the temperature modulation technique and the total sensor system is now discussed. First of all, the assumptions that were made to construct the models described in chapters 4 and 6 are critically reviewed. All of the assumptions are listed as follows:

Assumption I. The surface and bottom of the polymer film are flat and parallel to each other, and the carbon black nanospheres are uniformly distributed within the film.

Assumption II. The electric field between two electrodes is uniform and parallel to the surface (or the bottom) of the membrane.

Assumption III. The diffusion of the vapour molecules in the polymer follows Fick's law of linear diffusion.

Assumption IV. The change in local conductivity is linearly proportional to the local vapour concentration in the polymer, and the proportional constant is independent of the temperature.

Assumption I may not be reasonable for the films used in this project (PVP2, PVP8 and PVP11); the surfaces of the films were not flat or even uniform as is apparent from the photographs shown in figure 5.2. This is probably due to the crude and manual

deposition technique using the air-brush. It is believed that the quality of the film can be improved by using a fully automated nanolitre non-contact dispensing system (e.g. [7.6]).

Assumption II could be paraphrased as "the thickness of the film is negligible compared with the distance between the two electrodes". This is a reasonable assumption for PVP2 (1.9 μm) and PVP11 (0.8 μm), considering that the distance between the two electrodes used is 20 μm, but may not be reasonable for PVP8 (6.0 μm). It is possible to construct more rigorous model, which consider the geometry of the electrodes and polymer film (thus the electric field is not homogeneous or isotropic) as shown in [7.7].

Assumption III can be split into three sub-assumptions. First, it was assumed that there is no chemical reaction between the vapour molecules and polymer. In other words, the interaction between the vapour molecule and polymer is physisorption (thus the adsorption process is reversible). This sub-assumption was shown to be correct by observing that the conductance change is always reversible (For example, see figure 6.13.). Secondly, it was assumed that the diffusion coefficient is independent of the concentration of vapour molecules in the polymer. This assumption was correct for water, methanol and ethanol within the concentration range tested in the project (This is because the shapes of the curves were independent of the concentration of the vapour *e.g.* in figure 5.6.). However, there must be upper limit of the linear concentration range, and it is needed to find it before the technique is commercialised. Thirdly it was assumed that the diffusion coefficient is not affected by the presence of any other vapours. The results in chapter 6 do not confirm this assumption completely, though it seems to be correct for water and methanol of the concentration range tested in this project. Reproducibility should be confirmed by further tests.

Assumption IV is split into two parts. The first part *i.e.* the linear relationship between the local conductivity of polymer and the local vapour concentration was shown to be correct, by the linearity between the response and concentration shown in chapters 5 and 6. The second part *i.e.* the temperature independence of the proportional constant N has been implicitly assumed in this project as in [7.7]. However, it might be temperature dependent and the model could be improved by considering this. The steady state response at temperature T is described as follows (see for example equation (4.9 a)):

$$\frac{\Delta G(T)}{G_{dry}(T)} = N(T)c_{vapour}K(T) \tag{7.1}$$

where $\Delta G(T)$ is the conductance change, $G_{dry}(T)$ the steady state conductance without vapour, $N(T)$ the proportional constant, c_{vapour} the concentration of the vapour and $K(T)$ the partition coefficient. Therefore the temperature dependence of the proportional constant $N(T)$ can be found by measuring temperature dependences of both the steady state response and partition coefficient.

Apart from the work suggested above, it should be pointed out that the types of vapours tested in the project was limited to water, methanol and ethanol (vapours with polar molecules) and only one polymer material (polyvinylpyrrolidone with 20 wt % carbon black) is used. Therefore more vapours and polymers should be tested. It should be emphasized that one of the main aims of testing different polymer materials is to find a material with both high sensitivity and wide concentration range with linearity (and capability of superposition), although it seems to be a trade off problem intuitively. It is believed that the proposed technique could lead to the commercialisation of a new generation of ultra low power and low cost vapour sensors for indoor gas monitors.

References

[7.1] M. Rydberg and U. Smith, "Long-term stability and electrical properties of compensation doped poly-Si IC-resistors", IEEE Transactions on Electrical Devices, Vol. 47, No.2, 2000.

[7.2] Z. Tang, S.K.H. Fung, D.T.W. Wong, P.C.H. Chan, J.K.O. Sin and P.W. Cheung, "An integrated gas sensor based on tin oxide thin-film and improved micro-hotplate", Sensors and Actuators B 46, 1998, pp.174-179.

[7.3] E.J. Severin, B.J. Doleman and N.S. Lewis, "An investigation of the concentration dependence and response to analyte mixtures of carbon black/insulating organic polymer composite vapour detectors", Analytical Chemistry, 72, 2000, pp. 658-668.

[7.4] Y.S. Kim and Y.S. Yang, "Additional thermodynamic feature extraction from chemoresistive carbon black-polymer composite sensors by temperature modulation", Sensors and Actuators B, 121, 2007, pp. 507-514.

[7.5] J. R. Patel, L. R. Testardi, and P. E. Freeland, "Electronic effects on dislocation velocities in heavily doped silicon", Physical Review B, Vol.13, No. 8, 1976, pp. 3548-3557.

[7.6] BioDot, Inc, http://www.biodot.com/, accessed 26th October 2007.

[7.7] J.W. Yates, M.J. Chappell, J.W. Gardner, "A novel phenomena based dynamic model of carbon black/composite vapour sensors", Proceedings of the Royal Society A, 463, 2007, pp. 551 – 568.

Appendix A

Vapour testing system

Figure A.1 illustrates an overview of the vapour testing system. The system is divided into the following three independent systems:

1. A flow injection analysis (FIA) test station and its control system (figure A.2).
2. A temperature modulation system.
3. A data acquisition system.

The aim of the FIA test station is to expose the sensors to single or mixed vapours with controlled concentrations at controlled temperatures. The sensor was bonded onto a ceramic package and mounted in a stainless steel chamber which sits in a Dri-block^{TM} heater (model DB-2D, Techne Inc., US, accuracy: ± 0.1 °C). The temperature of the sensor was set to be 25 °C (The temperature of the Dri-block^{TM} heater was set to be 27 °C and the room temperature was controlled by air conditioner to be 22 °C (± 2 °C), and the temperature of the device was measured by reading the heater resistance as detailed in chapter 3).

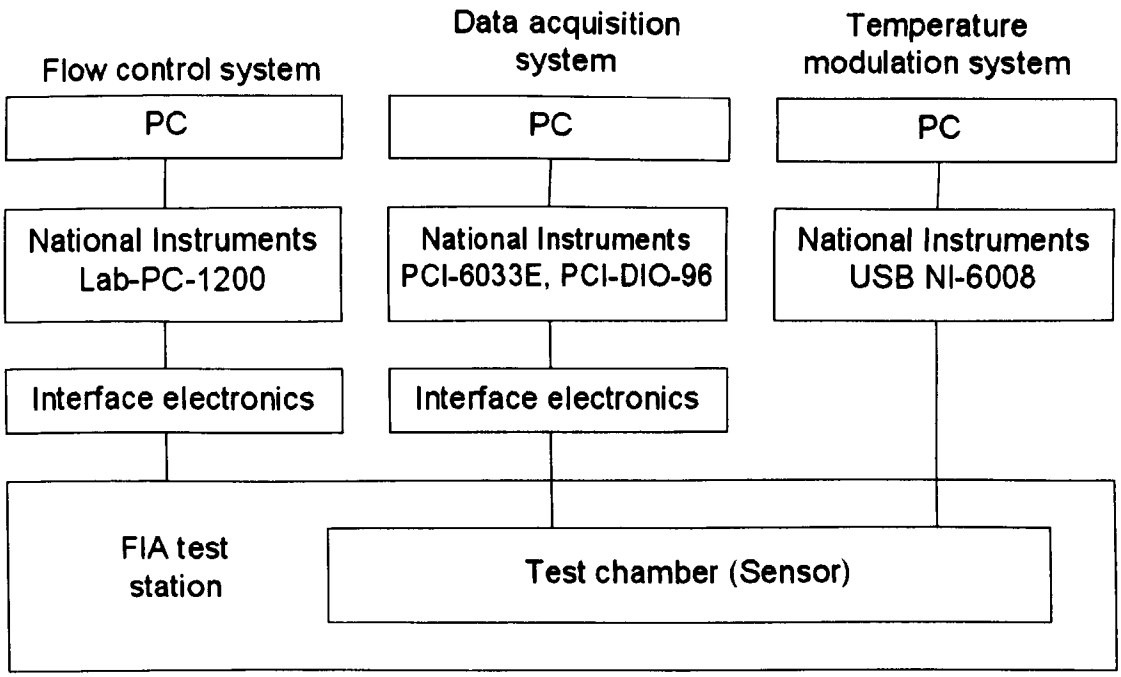

Figure A.1. Overview of the vapour testing system.

The carrier gas used in all the tests is air from a compressed air cylinder (BOC, UK). The air is desiccated by a silica gel desiccator near the entrance of the FIA test station, as the proposed technique requires measurements in dry air. Water, methanol and ethanol vapours are generated by bubblers [A.1]. The flow rate through the test chamber is always kept at 300 sccm, and the ratio of flow rate of each mass flow controller was modified to control the vapour concentrations. The temperature of the water bubbler is not fully controlled (though the air conditioner was always set to be 22 °C), and thus a humidity sensor is employed to control the water concentration inside the test chamber. The temperatures of the methanol and ethanol bubblers are controlled to be - 15 °C and + 5 °C, respectively, by a refrigeration bath (Life Sciences, Neslab RTE-300). The concentration of the output flow of the bubblers is calculated by dividing the partial pressure of the vapour by the atmospheric pressure (760 torr), and the partial pressure of the vapour is given by the Antoine vapour equation [A.2]:

$$\log P_v = A - \frac{B}{C+T} \tag{A.1}$$

where P_v is the partial pressure of the vapour (in torr), T is the temperature (in Kelvin), and A, B, and C are constants specific for materials. The constants A, B and C for

methanol and ethanol are listed in table A.1. All the mass flow controllers and the valves are controlled by the PC via a National Instruments Lab-PC-1200 card. Prior to any experiments carried out in this project, it was confirmed that the leak of the each vapour was less than 5 %. Therefore, the accuracy of the concentration values used in this thesis has the uncertainty of only 5 %. The system is described in more detail in [A.3].

Table A.1. Constants for Antoine vapour equation.

	Methanol	Ethanol
A	7.8975	8.32109
B	1474.08	1718.10
C	229.13	237.52

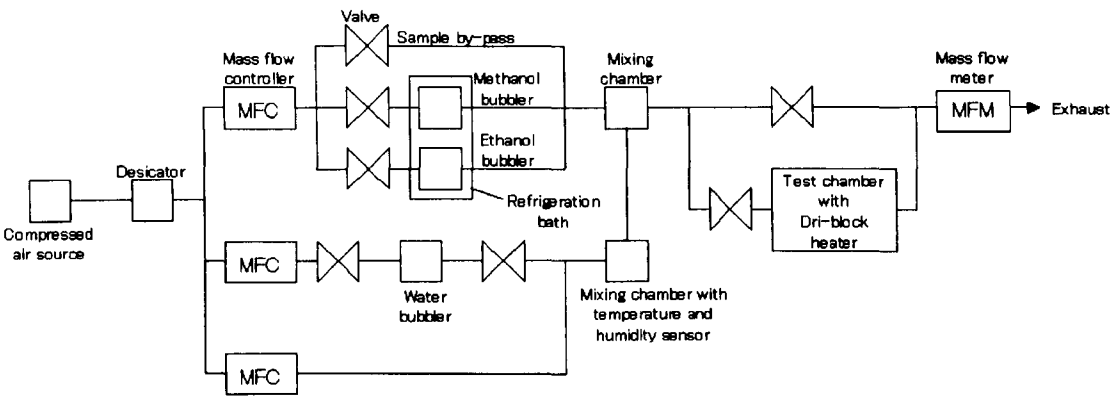

Figure A.2. Flow injection analysis (FIA) test station.

For this project a temperature modulation system was built. The system is capable of applying a multi-level square wave voltage (maximum 5 V) with the pre-set period to the sensor periodically, through the National Instruments USB NI-6008. The voltages and periods are fully controlled by the PC. The temperatures used in the experiments in this thesis were 25 °C, 35 °C, 45 °C and 55 °C, which require operating voltages (and powers) of 0 V (0 mW), 0.78 V (0.8 mW), 1.10 V (1.6 mW) and 1.35 V (2.4 mW), respectively. The accuracy of the analogue output voltage of NI-6008 was ± 0.01 V, which corresponds to the accuracy of the temperature modulation amplitude of ± 0.3 °C.

The data acquisition system was again developed elsewhere [A.4]. The system is capable of applying a constant current (10 μA for all the experiments in this thesis) to the sensing material, and record the voltage to the PC every 10 ms.

References

[A.1] T.C. Pearce, S.S. Schiffman, H.T. Nagle and J.W. Gardner, "Handbook of Machine Olfaction", Wiley-VCH, Dordrecht, 2003.

[A.2] N.A. Lange and J.A. Dearn, "Lange's Handbook of Chemistry", McGraw Hill, London, 1985.

[A.3] J.A. Covington, "CMOS and SOI CMOS FET-based Gas Sensors", Ph.D. Thesis, University of Warwick, Coventry, 2001.

[A.4] J.A. Covington and I. Griffith, "MTX-STH-1 User Manual Version 1.0", University of Warwick, Coventry, 2004.